Advanced Control Laws for Exoplanet Imaging Adaptative Optics

Nelly Natalia Cerpa Urra

▶ **To cite this version:**

Nelly Natalia Cerpa Urra. Advanced Control Laws for Exoplanet Imaging Adaptative Optics. Optics [physics.optics]. Université Paris-Saclay, 2022. English. NNT : 2022UPAST143 . tel-04102520

HAL Id: tel-04102520
https://pastel.hal.science/tel-04102520v1

Submitted on 8 Feb 2024

HAL is a multi-disciplinary open access archive for the deposit and dissemination of scientific research documents, whether they are published or not. The documents may come from teaching and research institutions in France or abroad, or from public or private research centers.

L'archive ouverte pluridisciplinaire **HAL**, est destinée au dépôt et à la diffusion de documents scientifiques de niveau recherche, publiés ou non, émanant des établissements d'enseignement et de recherche français ou étrangers, des laboratoires publics ou privés.

université PARIS-SACLAY

Advanced Control Laws for Exoplanet Imaging with Adaptive Optics

Lois de commande avancées pour l'imagerie d'exo-planètes par optique adaptative

Thèse de doctorat de l'université Paris-Saclay

École doctorale n° 575, Electrical, Optical, Bio: Physics and Engineering (EOBE)
Spécialité de doctorat : Physique
Graduate School : Sciences de l'ingénierie et des systèmes Référent : Institut d'Optique

Thèse préparée dans la (ou les) unité(s) de recherche **Université Paris-Saclay, Institut d'Optique Graduate School, CNRS, Laboratoire Charles Fabry, 91127, Palaiseau, France.**, sous la direction de **Caroline KULCSÁR**, Professeure des Universités, IOGS, LCF, France, le co-encadrement **Markus KASPER**, Docteur, chercheur à l'ESO, Garching, Allemagne, et de l'invitation de **Henri-François RAYNAUD**, Maître de Conférences, IOGS, LCF, France

Thèse soutenue à Paris-Saclay, le 15 novembre 2022, par

Nelly Natalia CERPA-URRA

Composition du Jury

Membres du jury avec voix délibérative

Philippe BEN ABDALLAH Directeur de Recherche au LCF, France	Président
Maud LANGLOIS Directrice de Recherche au CRAL, France	Rapportrice
Rodolphe CONAN Docteur, Giant Magellan Organisation, États-Unis	Rapporteur
Christophe LOVIS Docteur, professeur associé à l'université de Genève	Examinateur

THESE DE DOCTORAT

NNT : 2020UPAST143

université PARIS-SACLAY

ÉCOLE DOCTORALE
Physique et ingénierie : Electrons, Photons, Sciences du vivant (EOBE)

Titre: Lois de commande avancées pour l'imagerie d'exo-planètes par optique adaptative
Mots clés: Optique adaptative extrême (XAO), Systèmes en cascade à deux étages, Commande modale, Modes de Karhunen-Loève, Commande LQG, Imagerie haut-contraste.

Résumé: L'imagerie des exoplanètes est un défi à la fois technologique et scientifique. L'instrumentation des télescopes au sol doit produire des images à haut contraste au voisinage d'étoiles brillantes, tandis que des techniques d'observation appropriées doivent être mises en œuvre pour pouvoir détecter les compagnons stellaires. Cet objectif scientifique exigeant est rendu possible grâce aux systèmes d'optique adaptative (OA) extrême (XAO), qui sont capables de corriger en temps réel la déformation des images due à la turbulence. Des instruments équipés de XAO sont opérationnels sur des télescopes de classe 8 m, par exemple SPHERE au Very Large Telescope ou GPI à l'Observatoire Gemini Sud. Cependant, l'imagerie de compagnons très proches de leur étoile hôte et/ou d'extrêmement faible intensité nécessite d'améliorer un terme majeur du budget d'erreur en XAO : l'erreur temporelle due à la présence de retards inhérents à tout système d'OA. En effet, les systèmes opérationnels actuels n'atteignent pas le contraste nécessaire pour obtenir l'image directe d'une petite exoplanète (comme Proxima b), et par ailleurs ils ne peuvent pas être facilement modifiés pour atteindre la sensibilité requise. Dans ce manuscrit, nous considérons un système d'OA en cascade à deux étages (CAO), obtenu en ajoutant en série à un système XAO existant (le 1er étage) un autre système d'OA plus rapide et plus sensible (le 2e étage). Ce 2e étage est équipé d'un analyseur de front d'onde de type pyramide (PWFS) qui permet une meilleure sensibilité qu'un analyseur Shack-Hartmann (SHWFS). Nous proposons deux structures différentes de CAO et considérons l'utilisation d'une commande prédictive pour le 2e étage : un régulateur linéaire quadratique gaussien (LQG). Le manuscrit présente le contexte de nos travaux en termes d'instruments XAO existants, en se concentrant sur les améliorations qui peuvent être apportées pour l'imagerie à haut contraste, ainsi que sur les éléments clé d'un système CAO pour un télescope de classe 8 m. Un premier système CAO est proposé, composé d'un 1er étage à résolution spatiale élevée mais lent (fréquence d'échantillonnage de l'ordre de 1 kHz) corrigeant la phase turbulente entrante. La phase résiduelle qui en résulte est envoyée à un 2e étage à basse résolution spatiale mais rapide (fréquence d'échantillonnage de 4 kHz), équipé d'un PWFS. Des correcteurs à action intégrale sont utilisés pour les deux étages. Les simulations numériques démontrent que cette architecture CAO standard améliore globalement la performance, avec un meilleur contraste à faible séparation angulaire. Nous étudions également la durée de vie des tavelures et leur contribution au bruit lors de longues poses. Ce système CAO est ensuite amélioré par l'ajout d'un schéma de compensation pour traiter les composantes haute fréquence et non stationnaires dues au sur-échantillonnage effectué par le 2e étage. Nous expliquons comment cette astuce permet d'améliorer les performances grâce au fait que le 2e étage se comporte alors comme un étage rapide autonome avec une meilleure sensibilité, tout en bénéficiant de la résolution spatiale plus fine du 1er étage. Nous effectuons également des simulations numériques et une évaluation des performances de ce nouveau système en remplaçant l'intégrateur du 2e étage par un régulateur LQG. L'évaluation des performances en termes de contraste montre une amélioration significative pour cette nouvelle structure CAO par rapport à un système XAO à un seul étage ou par rapport à la structure CAO initiale. L'utilisation du régulateur LQG améliore encore le contraste en particulier à faible séparation angulaire. Une telle performance mettrait par exemple à portée de main la détection de l'oxygène dans l'atmosphère de Proxima b (s'il était présent en quantité de façon similaire à la Terre).

Title: Advanced Control Laws for Exoplanet Imaging with Adaptive Optics
Keywords: Extreme Adaptive Optics (XAO), Two-stage cascade systems, Modal control, Karhunen-Loève modes, LQG control, High-contrast imaging.

Abstract: Exoplanet imaging is both a technological and scientific challenge. Ground-based telescopes instrumentation must produce high contrast images in the vicinity of bright stars, while proper observation techniques must be implemented to be able to detect stellar companions. This demanding science goal is made possible thanks to extreme adaptive optics (XAO) systems that are able to correct in real time for image deformation due to turbulence. Instruments equipped with XAO are in regular operation on 8 m-class telescopes, e.g., SPHERE at the Very Large Telescope or GPI at the Gemini South Observatory. However, imaging companions that are very close to their host stars and/or that are extremely faint needs to improve a major term of the XAO error budget, which is the temporal error due to the presence of delays inherent to any AO system. Indeed, current operational systems do not achieve the required contrast to obtain a small exoplanet's (like Proxima b) direct image, and neither can be easily modified to achieve the required sensitivity. In this manuscript we consider a two-stage Cascade AO system (CAO), which consists in putting in series to an existing XAO system (the so-called first stage) another but faster AO and more sensitive system, namely a second stage. This second stage is equipped with a Pyramid Wavefront Sensor (PWFS) that allows better sensitivity than a Shack-Hartmann Wavefront Sensor (SHWFS). We propose two different CAO structures and consider the use of a predictive controller for the second stage, a Linear Quadratic Gaussian (LQG) regulator. The manuscript presents the context of our research in terms of existing XAO instruments focusing on the improvements that can be made for high contrast imaging, together with key elements to study a CAO system for an 8-m class telescope. A first CAO system is proposed, composed of a slow (that is, in the order of a 1 kHz sampling frequency) high-order first-stage that corrects for the incoming turbulent phase. The resulting residual phase is sent to a fast (4 kHz sampling frequency) low-order second stage equipped with a PWFS. Integral action controllers are used for both stages. Numerical simulations demonstrate that this standard CAO architecture can benefit overall performance, with better contrast at small angular separation. We also study the lifetime of atmospheric residual speckles and their noise contribution in long exposures. This CAO system is then improved by adding a compensation scheme to deal with the high-frequency and non-stationary components due to the over-sampling done by the second stage. We present how this trick can improve the overall performance by making the second stage behave like a stand-alone fast stage with better sensitivity, while taking advantage of the finer spatial resolution of the first stage. We also perform numerical simulations and performance evaluation for this new scheme by replacing the second stage integrator by an LQG regulator. Our contrast performance assessment shows a significant improvement of the proposed CAO structure over a single stage XAO system or over the initial CAO structure. Using the LQG regulator improves contrast further in particular at low angular separation. Such a performance would for example bring the detection of oxygen in the atmosphere of Proxima b (if it were present in an Earth-like abundance) within reach.

Maison du doctorat de Université Paris-Saclay
2e étage, aile ouest, École normale supérieure Paris-Saclay
4 avenue des Sciencs
91190 Gif-sur-Yvette, France

A mis padres.

Acknowledgements

After almost five years of starting my journey as a Ph.D. student, now it is almost ending, and I would like to complete it by thanking everyone I have met during all these years. First, I would like to start with my supervisors. Caroline, Markus, and Henri-François, I'm incredibly thankful for the encouragement and support you have given me all these years. Thank you for your vote of confidence in me to start this marathon. I immensely appreciate how you always helped me even in the most challenging times of this Ph.D. Thank you, Markus, for introducing me to the world of Astronomy and Exoplanetary science. I learned to so much from the technology and science behind astronomy, and I couldn't have asked for a better person to teach me all about it. Thank you, Caroline and Henry-Francois, for opening my curiosity and to dive into the world of automatic control. Thank you for pushing me to ask questions and for the productive visits to Palaiseau. I would also like to thank all the Ph.D. students and researchers I met at the Charles Fabry Laboratoire. Thank you for the many walks and conversations we had at lunchtime! Thank you, Leonard, for introducing me to OOMAO and always being available for my questions regarding SHWFS and coding. Of course, I also want to thank the people at ESO. I'm incredibly thankful for the fantastic ESO Adaptive Optics group. I need to thank all for your kindness and support. I will never forget our meetings and coffee breaks. I'm immensely thankful for always being available for my questions and for receiving me with great disposition since the first day I arrived at Garching. Thanks, Pierre-Yves, for meeting with me that first time at the ESO in Santiago. Your attentiveness made me want to be part of this organization and start this journey. Thank you, Miska, for introducing me to AO simulations and always sharing a piece of advice. Thanks, Stefan, for teaching me the lab work (and for the many ThorLabs candy boxes!). Thanks, Jérôme, for all the talks and advice. Thank you, Christophe, Pierre, Sylvain, and Elise, for always being available to share your knowledge with me.

I absolutely have to thank my office mates!. Prashant! My first office mate! You arrive to fill the emptiness of office E.3.54/3. Thank you for all the advice, the laughs, and the good times. I hope we can meet again soon! Of course, the pizza master Taïssir!, office E.3.54/3, was not the same as the first time you left,

and we were so happy when you came back! Thank you for the fantastic pizza and for always being supportive not only for me but for Pablo too. I only hope we can keep the friendship for years to come, and we are waiting for your visit to Chile to try the pizza oven! I also have to thank Kelly (I still find confetti between my notebook pages from my birthday decoration!) and Byron for making the office such a special place!

I also need to thank all the other Ph.D. students at ESO and honorary members of the "Garching Group". Thank you, Tereza, for the fantastic friendship! I never met someone so intelligent and unique as you. Thank you for always being there, and I'm sure Gastón couldn't ask for a better ski instructor! Thanks, Carlo, for the conversations and all the lunches we had together! You made us fall in love with Trento, and only time will tell if Pablo's plan to retire there comes to life! Thank Alex, Misa, Sarah, Eleonora, Silvia, Kateryna, Serban, Calum, Benoit, Stephen, and Jens. I never had so much fun with our outings to the lake, the volleyball matches, and the exquisite Italian cuisine we had! My heart is filled with love from all the fantastic people we met during these years, and you are all more than welcome to visit us in Chile! (we will be waiting!).

Of course I want to thank my parents. Gracias por su apoyo incondicional. Gracias Mamá por ser mi ejemplo a seguir como mujer, madre y trabajadora. Gracias por siempre entregarlo todo por tu familia. Gracias Papá por inculcarme el no temerle al conocimiento, y por siempre tener unas palabras de aliento para los momentos difíciles. No tengo más que agradecerles por el infinito apoyo que nos dieron como familia. También le agradezco a Miguel y Soledad, por toda la ayuda que nos dieron para partir esta aventura, y gracias por siempre estar presentes cada vez que los necesitabamos.

Finally, I have to thank my family. Thank you, Pablo. Because you gave me the courage to start this journey, this achievement belongs to you as much as to me. Without your support and encouragement, I would have never been able to reach the finish line. Thank you for always being by my side and caring for Gastón and me. Thank you for your infinite effort to make our life the best possible. I'm absolutely sure I wouldn't have all these amazing friends if it weren't for your social skills! It definitely made our German stay hard to forget. Thank you, Gastón, for coming to brighten our days and filling our heart with kindness and unconditional love.

It is difficult not to forget anyone, but I just want to thank anyone who gave me a bit of advice, a word of wisdom, a piece of knowledge, or even a good moment during all these years.

Contents

List of Figures

Chapter 1

Introduction

Atmospheric turbulence is one of the main factors for degradation of spatial resolution of images obtained using ground-based astronomical telescopes. Air masses through the atmosphere are not homogeneous, and there is a mixture of various layers at different temperatures moving at different velocities and directions. These temperature variations produce density and therefore refractive index fluctuations along the propagation path of the light.

When entering the atmosphere, the light wavefronts from far away sources are flat, but will then be deformed by propagating through different regions of air with different refractive index. These distortions will blur the images and reduce peak intensity of point sources.

As a response, Adaptive Optics (AO) was born as a way of compensating the phase deformations produced by this atmospheric turbulence. AO was first proposed by Babcock, 1953 as a way to improve astronomical images using an active optical element (like a Deformable Mirror (DM)) that instantaneously corrects for the wavefront phase distortions. These distortions are measured by a Wavefront Sensor (WFS) from which the signal is derived to drive the correcting element. Even though this was a promising concept, the required technology was not available at the time.

From the late 1950's up until the beginning of the 1980s, there where numerous progress in AO and image processing, in particular by the military to provide sharper images for surveillance (Fontanella, 1985; Gaffard and Boyer, 1987; Hardy, Lefebvre, and Koliopoulos, 1977; Pearson, Freeman, and Reynolds, 1979) and the first AO system was developed for defense applications. But it was not up until the mid 1980's that several programs to take AO to the astronomy field were born, and by the end of the 1980's the first astronomical AO system (COME-ON) was built (Rigaut et al., 1991; Rousset et al., 1990).

As a joint effort, the European Southern Observatory (ESO) and the US National Optical Astronomy Observatories (NOAO) decided to develop a program

of AO for infrared astronomy. COME-ON was installed at the Observatoire de Haute-Provence in France in 1989, and in 1992 an upgraded version (COME-ON-PLUS) was set on the ESO 3.6m telescope at La Silla (Chile). Since then, a growing number of telescopes started implementing AO systems with different configurations, WFSs and DMs.

This new generation of AO systems was of great benefits for the development of astronomy in many scientific areas. The images obtained with unprecedented high spatial resolution present an important value for the astronomical science, and now after decades of development, AO is used in astronomy on a regular basis. AO systems can nowadays be tailored to improve the on-axis image quality for exoplanetary imaging, or to improve an extended field of view for extragalactic astronomy using Multi-Conjugate AO.

In less than 10 years from now, the next generation of large scale telescopes like the Extremly Large Telescope (ELT) (ESO, 2022), will be operational. This new telescope, with a diameter of 39m, and equipped with instruments using AO, will enable scientists to image Earth-like planets around the nearest stars. Now that the limits of AO are being pushed further and further, the direct imaging of small exoplanets come within reach but the development of the required AO instrumentation still presents significant challenges. The contrast requirements for the exoplanet science case are far from being easy to achieve. The AO complexity strongly scales with the size of the telescope aperture and the necessity for higher contrasts calls for a superb correction of the incident wavefront distortion by an Extreme Adaptive Optics (XAO) system and a subsequent coronagraph to further suppress diffracted stellar light.

1.1 The Exoplanet Science Case

Since the first detection of an exoplanet around a main sequence star more than 25 years ago (Mayor and Queloz, 1995), the hunt for exoplanets has been more than prolific. Exoplanetary science is one of the most rapidly developing fields in astrophysics. Its goal is not only to be able to identify new extrasolar systems, but also to detect, characterise and understand the compositions of exoplanets and their atmospheres. Planets are characterised by their low mass and small size compared to their host stars. They only reflect the light emitted by those, making exoplanets very difficult to observe by direct imaging. More than 3.000 exoplanets have so far been detected (http://exoplanets.org/), using mostly two indirect detection techniques:

- Radial Velocity (RV): Being a very productive method so far for exoplanet detection, RV is based on the Doppler shift effect produced by the gravitational pull of an unseen exoplanet on its host star (see Figure 1.1). Both orbit

around the center of mass of the star-planet system. When the star moves away from the observer, the light moves to longer wavelengths and is redshifted, while when it returns, it shift towards shorter ones and is blueshifted. These measurements are done using high resolution (R $\sim$ 100.000) spectrographs like the High Accuracy Radial velocity Planet Searcher (HARPS) mounted on ESOs La Silla 3.6-m telescope. Even though RV is the most prolific method for exoplanet detection, it does not provide information about some important planet parameters like radius, and mass estimates can be uncertain because the inclination of the system is usually not known.

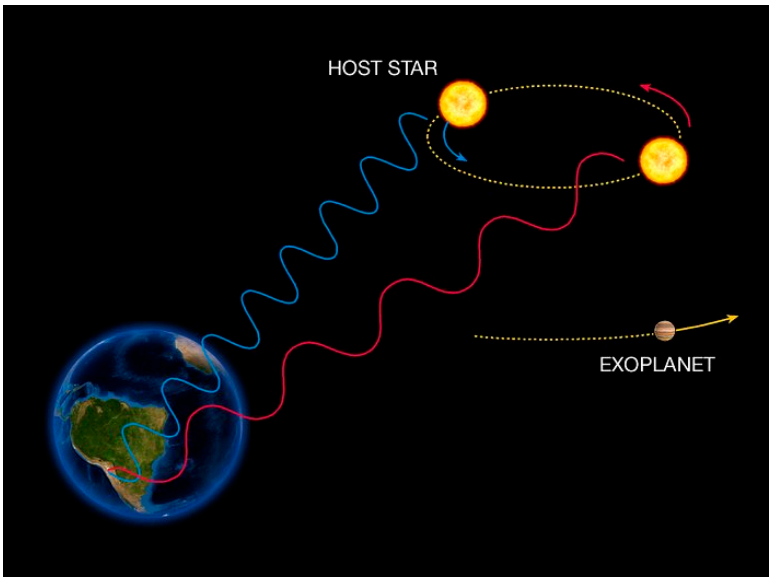

Figure 1.1: The radial velocity method to detect exoplanet is based on the detection of variations in the velocity of the central star. (From ESO)

- Transit: Used also as a follow up for RV detections, transits occur when a planet passes in front of its host star, producing a brightness variation during its transit (see Figure 1.2). This method provides us estimates about planet parameters like radius, and density (together with a mass estimate from RV- without sin i uncertainty [1] because transiting orbits are edge-on) and because of its technical simplicity, numerous transit surveys are active (Charbonneau et al., 2007).

[1] sin i uncertainty: The observer only sees the RV component along the line of sight. When the planet orbit is not edge-on and is seen at an inclination i smaller than 90 degrees, the measured RV is a factor sin i smaller than the true RV, and the derived planet mass is smaller than the real one by the same factor.

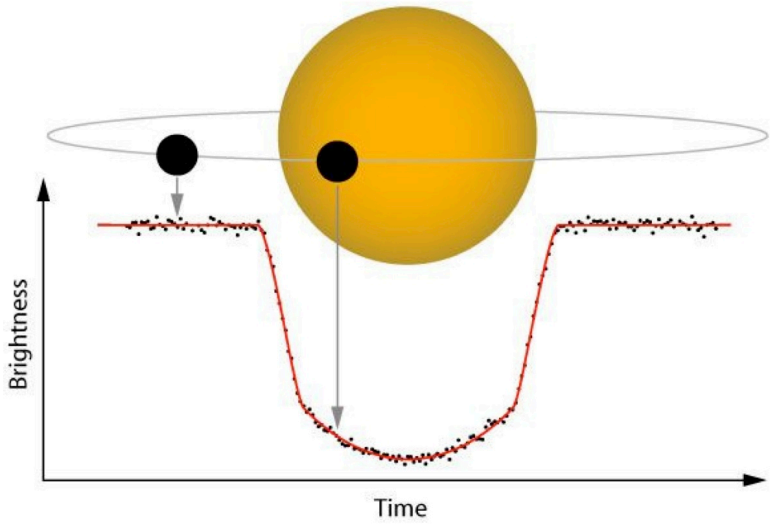

Figure 1.2: Transit method technique that uses a brightness variation of a star for exoplanet detection (From ESO)

Using RV, transits, and other methods, scientists have developed a basic statistical understanding of the inner regions of planetary systems. But because the RV and transit methods are most suitable to find large planets on short orbits (less than a few years and < 5 Astronomical Units (AU)), the statistical results are biased to this kind of objects.

Therefore, the angular separations of exoplanets detected by the RV or transit methods to their host stars are usually very small, and these methods detect no light from the exoplanets themselves. Hence even the most fundamental physical parameters of these planets (luminosity and temperature) are not measured, and the information is limited to mass and orbit (RV, with sin i uncertainty), size and orbit (transit, edge-on orbit) and density (combining RV and transit results where possible). Therefore, only direct imaging and -to a lesser extent- transit spectroscopy (Spake et al., 2018) providing spectral data from the visible to the near-infrared and polarimetric information will allow us to characterize the planets and their atmospheres, see, e.g., (Kasper, Cerpa Urra, et al., 2021) and references therein.

As we mentioned before, the intensity contrast between the stellar light reflected off a planet surface, and the star itself is less than one part in a million at a few ten mas of angular separation and gets even smaller for larger distances. The restrictions are even more significant for Earth-like planets, and such high-contrast observations are not yet possible with the current telescopes and instrumentation. Even the recently launched James Webb Space Telescope (JWST) does not reach

the required imaging contrasts for this science case. It, however, adds thermal IR direct imaging observations mostly to known young Exoplanets (Carter et al., 2022), and performs transit spectroscopy characterization of nearby planets on close-in orbits. However, planet evolutionary models predict that giant planets glow in the near-infrared when they are young and still warm, making them more easily detectable and with less contrast restrictions (Baraffe et al., 2003; Burrows et al., 1997; Marley et al., 2007).

The contrast of temperate Earth-like planets to their host stars increases in the thermal IR by a factor of 100-1000 wrt to the one obtainable in the reflected light. Still the required 10^{-7} contrast and the significantly increased sky background are such that only the habitable zones of αCen A and B can be searched for Earth-like planets with current ground-based telescopes. Such an attempt was made with the New Earths in the Alpha Cen Region (NEAR) instrument at the Very Large Telescope (VLT) (Kasper, Arsenault, et al., 2017) and provided the detection of a weak feature which could be the signature of a Neptune or larger size planet in the habitable zone of αCen A (Wagner et al., 2021).

On the other hand, theoretical models of planet formation predict that the peak of formation of giant planets is found close to the snow line[2] at several AU depending on the star's luminosity, thanks to the availability of a larger amount of condensate in the protoplanetary disk. In outer regions, the longer timescales involved should make planet formation a less efficient process. In addition, migration mechanisms and long-term orbit instabilities will alter the original orbital distribution.

The young stars closest to the Sun are members of young moving groups such as β Pictoris at typically a few tens of parsec distance. Unfortunately, for current 8-m class telescopes, the ice-line cannot be spatially resolved easily.

Other models considering migration in protoplanetary disks (Goldreich and Tremaine, 1980) could explain the existence of hot Jupiters (Mayor and Queloz, 1995) but do not provide us with a population of giant planets already observable by direct imaging. Such models (Alibert et al., 2013; Boss, 1997) produce only a small population of planets at large separation (see Fig. 1.3) beyond 10 AU accessible by direct imaging with current 8-m class telescopes.

Determination of the frequency of giant planets in wide orbits (5-10 AU) would allow testing fundamental aspects of the planet formation models. In agreement with these models, direct imaging surveys have found only a small amount of giant planets at large separations. Earth-like planets around M-stars are exciting targets for High-contrast Imaging (HCI) with the ELT. In the near-IR and visible bands,

[2]From Wikipedia: [...] The snow line [...] is the particular distance in the solar nebula from the central protostar where it is cold enough for volatile compounds such as water, ammonia, methane, carbon dioxide, and carbon monoxide to condense into solid ice grains.

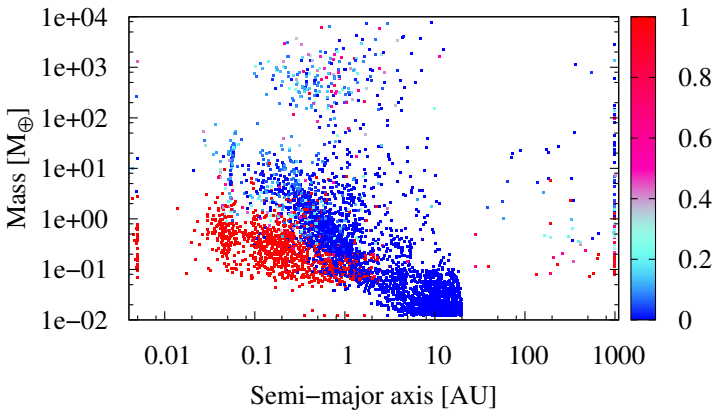

Figure 1.3: From: Alibert et al., 2013, Mass versus semi-mayor axis for a theoretical model of planetary system formation.

the reflected light component from inner planets is brighter than thermal emission, especially for rocky planets lacking strong internal heat. Reflected light imaging with XAO systems promises to be able to characterize potentially habitable rocky planets orbiting nearby stars. The most accessible targets are nearby M-type stars for which the planet-to-star contrast would be between 10^{-7} and 10^{-8} (Guyon, 2018). The most promising target, Proxima Cen b, is a potentially habitable planet orbiting the nearest star (Anglada-Escudé et al., 2016), expected to be at $\approx 10^{-7}$ contrast in reflected light at a 38-mas separation.

Finally, even though the primary motivation for XAO is to observe exoplanets and circumstellar discs, there is a wide range of astronomical challenges that can be addressed using XAO as we can see on Fig. 1.4.

Other uses for XAO and HCI are the characterisation of diffuse material (dust, gas) around stars, extragalactic astronomy, and even visible-light imaging.

1.1.1 Contrast requirements for exoplanetary science

To obtain direct images and characterize Earth-like planets, the combination of telescope and instrument must provide extremely high contrast and good sensitivity. The contrast requirements for imaging planets in reflected light are e.g. 10^{-7} at 0.01 arcseconds for an Earth-size planet in the habitable zone around nearby M-stars, and 10^{-9} at 0.1 arcseconds to observe similar objects around earlier type of stars at larger distances from us (see Figure 1.5).

As we can see on Figure 1.5, if we can achieve these levels of contrast, then we could obtain direct images of potentially habitable planets around M-stars that

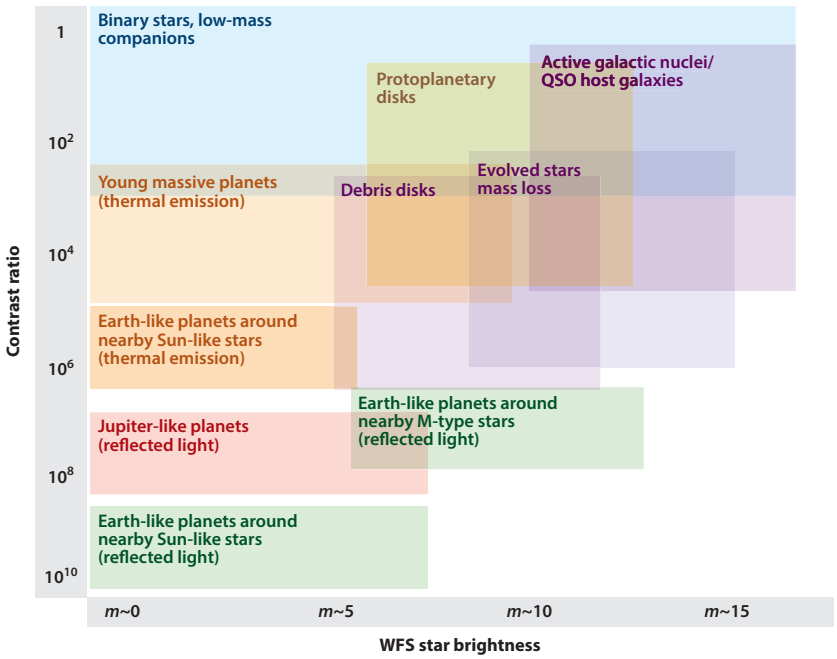

Figure 1.4: A selection of XAO science cases as a function of guide star brightness (horizontal axis, brightness decreases from left to right) and contrast ratio (vertical axis) (Guyon, 2018)

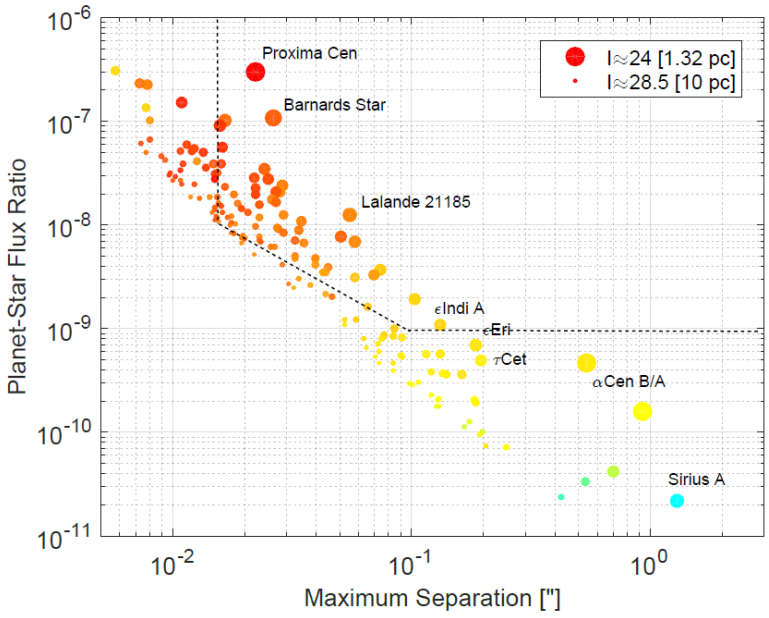

Figure 1.5: Contrast versus angular separation for different planetary systems. The symbol size indicates the planet apparent brightness, and the colour indicates the spectral type (red are M-stars and yellow are solar-type stars). The dotted line indicates the approximate contrast boundaries of the Planetary Camera and Spectrograph for the ELT (From Kasper, Cerpa Urra, et al., 2021)

have been already detected using RV or Transit methods. M-stars are particularly interesting because around 80% of all stars belong to this group and many of them are nearby. Temperate small planets were already found around Proxima Cen (1.4 pc; Anglada-Escudé et al., 2016), Barnard's star (1.8 pc; Ribas et al., 2018), Lalande 21185 (2.5 pc; Díaz et al., 2019), and Teegarden's star (3.8 pc; Zechmeister et al., 2019). It is therefore of utmost scientific importance to understand if such planets might provide habitable conditions or even show atmospheric fingerprints of biological activity.

The most prominent of these biosignatures is molecular oxygen (O_2), which was originally identified as a promising pathway to find extraterrestrial life in exoplanet atmospheres by Lovelock, 1965. It is currently the most easily detectable signal of life in Earth's atmosphere (20% by volume), created as a product of photosynthesis. Most prominent for optical to Near-InfraRed (NIR) observations is the O_2 A-band at around 765 nm, which consists of a forest of narrow lines. A spectral resolution of several hundred thousand would resolve the unsaturated lines (López-Morales et al., 2019), and still a spectral resolution of around one hundred thousand would be needed to resolve the saturated lines expected to be present in the spectrum of a directly imaged exoearth. In addition, such a High-Dispersion Spectrum (HDS) also presents the opportunity to spectrally isolate the planet signal and differentiate it from residual stellar light, thus improving the achievable contrast and sensitivity. Contrast improvements of at least 1:10,000 have been realized by HDS, which would in principle multiply with the contrast achievable by other methods to suppress stellar light at the position of a planet (Snellen et al., 2015).

1.1.2 High Contrast Imaging and XAO

HCI will enable us to obtain direct images of planets around nearby young low-mass stars. Because of the very small angular separation of the planets from their host stars, the light from the star itself must be suppressed by using a coronagraph if most of the energy is concentrated at the center of the Point Spread Function (PSF), i.e., when the Strehl ratio (SR) is high.

The XAO objective is to increase the Strehl ratio of the corrected PSF to well above 70% (a more detailed description of performance criterion is given later in Chapter 2.), and to suppress the halo of the scattered light around the host star at the same time, thus minimising the photon noise. For this, the XAO DM provides a larger number of actuators than usually deployed by regular multi-purpose astronomical AO systems. Also, the angular size of the PSF region over which the DM has an impact (control radius) is proportional to the ratio between the wavelength and the actuator spacing projected onto the telescope aperture.

Each component of an XAO system is pushed to its limits, and an important amount of research and development (R&D) is done to be able to minimize as much

as possible the residual variance of the wavefront. The residual XAO errors produce rapidly changing patterns of diffraction-limited speckles. Over long exposures, these speckles are averaged out, and they can be removed with post-processing. But if we assume that the speckle noise reduces with $1/\sqrt{t_{dc}}$, where t_{dc} is the speckle decorrelation time, then a residual speckle halo with typical intensity contrast of about 10^{-5} would require 10^6 independent realizations to reach a level of 10^{-8} in the absence of other instantaneous speckle correction techniques. Depending on the speckle lifetime, accumulating that many realizations of the speckle pattern can be a very long process.

The speckle lifetime is proportional to the ratio between telescope diameter (D) and the wind-speed (v), more specifically $0.6D/v$ (Macintosh, Poyneer, et al., 2005). In the case of the VLT, with winds of 10 m/s, the atmospheric residual speckle lifetime is therefore of the order of half a second, and in the ELT case, speckles are expected to decorrelate on timescales of up to several seconds. Such lifetimes would lead to unfeasible long exposure time requirements (more than 100 hours for the 10^6 independent realizations motivated above) to be able to reach very high contrast images. These considerations underline the high interest in reducing the lifetime of residual atmospheric speckles, and even if the frozen flow assumption may be pessimistic in this context, there is a necessity of pushing XAO performance to its limits.

A second source of errors are the long-lived quasi-static speckles. These are produced by instrument aberrations, which are left uncorrected by the AO system (Marois et al., 2003) and are one of the dominating factors affecting contrast especially at low angular separations (Guyon, 2005). These residual aberrations can occur in the instrument's science camera optical path (which is not seen by the AO WFS), or in the optical path to the AO WFS (which is not seen by the science camera). Therefore they are called Non-common Path Aberrations (NCPA). During an observation tracking a target in the sky, NCPA change only slowly on timescales on which the instrument orientation and the gravity vector changes.

Even using XAO, the instruments available today at 8-meter class telescope achieve contrast levels of 10^{-6} at best, and are restricted to observe relatively bright stars with magnitudes up to around 9 on the I-band. The SPHERE instrument (**S**pectro-**P**olarimetric **H**igh-contrast **E**xoplanet **Re**search) (Beuzit et al., 2019a) is a highly specialised exoplanet imager and spectrograph. Located at the ESO VLT (Very Large Telescope), SPHERE controls a 41x41 actuators DM and is divided in four systems: the Common Path and Infrastructure containig the SAXO XAO system (Fusco, Sauvage, et al., 2014) and the three science channels, a differential imaging camera IRDIS (**I**nfra**R**ed **D**ual **I**mager and **S**pectrograph) (Dohlen et al., 2008), an Integral Field Spectrograph (IFS) (Claudi et al., 2008), and a visible

imaging polarimeter ZIMPOL (**Z**urich **Im**aging **Pol**arimeter) (Thalmann et al., 2008). The detection limit for the SPHERE instrument is around 10^{-6} at 0.5 arcsec (i.e, 15 magnitudes between the star and the planet). On-sky performance is available at (Sauvage et al., 2016) and a confirmation of the performance levels reached during the first two and a half years can be found in (Milli, Mouillet, et al., 2017). ESO's 39-m Extremely Large Telescope with first light planed for 2027 aims to obtain the first images of an Earth-like planet. However the performance of the XAO system has to still be perfected and enhanced in order to fully take advantage of the bigger mirrors and finally reach the goal of a direct image of an Earth-like exoplanet.

1.2 Aim of this work

As we mentioned before, for optical and near-IR HCI, the AO-corrected residual halo stellar flux is the main source of measurement noise (Otten et al., 2021). In order to obtain great contrast sensitivity for exoplanet imaging at small angular separations, it is therefore crucial to minimize this residual halo which is typically dominated by the AO temporal delay at small angular separations (Guyon, 2005).

A straightforward approach to reduce the temporal delay would be to run the AO system faster at the expense of increased detector read-noise. Ultra-fast AO systems for high-contrast imaging are under development at several observatories, using either a single-stage (Chilcote et al., 2020), a woofer-tweeter (Bond et al., 2020; Males and Guyon, 2018) or a Cascade Adaptive Optics (CAO) system with two stages (Boccaletti et al., 2020; Chazelas et al., 2020; Lozi et al., 2018).

The 2^{nd} AO stage has its own deformable mirror (DM), wavefront sensor (WFS) and RTC behind the 1^{st} stage AO system. This 2^{nd} stage only sees the residuals of the wavefront pre-flattened by the 1^{st} stage and can therefore employ a DM with small actuator stroke. As the scientific interest is mostly at very small angular separations, the AO correction radius (Perrin et al., 2003) can be small, and the number of actuators of the 2^{nd} stage's DM can be relatively low, leading to a compact design and moderate computational demands. These properties and the possibility to develop and test the 2^{nd} stage stand-alone and retrofit it to an already existing 1^{st} stage make this approach very attractive for upgrades of existing AO systems such as VLT-SPHERE (Beuzit et al., 2019b) or VLT-AOF (Madec et al., 2018).

Another approach to reduce temporal error is the use of predictive controllers, generally based on evolution models of the disturbance, instead of the standard integral action controller (the so-called integrator). The goal is to predict the disturbance at short time scales (in the order of the sampling time) to compensate for the unavoidable delays present in the AO system.

Along this line, a natural way is to design a Linear Quadratic Gaussian (LQG) controller (see, e.g., (Anderson and Moore, 1990)). The models of the whole system including disturbance have to be linear and expressed in state space form Gaussian noises, in order to derive a Kalman filter that provides optimal prediction. LQG controllers optimize a criterion which is a quadratic function of the state and control and were proposed for ground-based adaptive optics for the first time by (Paschall, Von Bokern, and Welsh, 1991; Paschall and Anderson, 1993), showing the great potential of this approach. In these seminal works, the solution was not optimal with respect to the variance of the residual phase. An optimal formulation where the quadratic criterion indeed corresponds to the variance of the residual phase has been proposed later in (Kulcsár, Raynaud, Petit, and Conan, 2012; Kulcsár, Raynaud, Petit, Conan, and Viaris de Lesegno, 2006; Le Roux et al., 2004), with a demonstration that the optimal LQG control design can be done equivalently in discrete time.

LQG control has been studied for various AO systems and with various control configurations, from single conjugate AO (SCAO) in a modal basis with independent disturbance models leading to scalar controllers in parallel (Looze et al., 1999), to the fully multivariable case and to wide-field AO, see, e.g., (Correia, Jackson, et al., 2015; Hinnen, Verhaegen, and Doelman, 2007; Le Roux et al., 2004; Petit, Conan, Kulcsár, and Raynaud, 2009; Petit, Conan, Kulcsár, Raynaud, and Fusco, 2008; Piatrou and Roggemann, 2007b; Sivo, Kulcsár, Conan, Raynaud, É., et al., 2011). A formulation using Fourier domain disturbance modeling has been also proposed with Fourier domain (Poyneer and Véran, 2010) or time domain (Massioni et al., 2011) efficient implementations.

Thanks to several on-sky demonstrations, it has been shown that an LQG controller with a disturbance model identified from telemetry data could largely outperform the standard integrator. This was shown from cases where only a few low order modes were controlled with LQG, higher orders being controlled with the integrator (Doelman, Fraanje, and Breeje, 2011; Tesch et al., 2015) to cases where the AO system is fully controlled with an LQG regulator (Sinquin et al., 2020; Sivo, Kulcsár, Conan, Raynaud, Gendron, et al., 2014).

These results and demonstrations lead to the use of LQG on operational exoplanet detection instruments, such as SPHERE, with a two-mode tip-tilt LQG controller (Petit, Sauvage, et al., 2014), and GPI with a three-mode LQG control (Poyneer, Palmer, et al., 2016), the higher modes being controlled by an integrator in both cases. The idea of controlling some low-order modes only using a predictive controller has been retained for example for the multiconjugate system NFIRAOS at TMT (Correia, Véran, et al., 2011) or for the SCAO mode of the MICADO ELT instrument (Zidi et al., 2022a).

In this manuscript, we will study a two-stage cascade AO system with the

assumption that only the second stage can be freely customized. A full LQG controller will thus be designed using a minimum variance criterion and in discrete-time, with a disturbance model identified from the second stage telemetry data. The identification method is similar to the one used for the low orders in (Sinquin et al., 2020) or (Haffert, Males, Close, et al., 2021) and allows therefore for regular updates in case of varying turbulence conditions.

From this point of view, the recent works on model-based controllers with reinforcement learning from (Nousiainen, Rajani, Kasper, Helin, et al., 2022; Nousiainen, Rajani, Kasper, and Helin, 2021; Pou et al., 2022) are very promising but will not be explored here.

First, on Chapter 2 we do a whole overview of AO, we introduce the each components of an AO loop. We pay particular attention on the controller side of an AO system and the XAO case. We also present the context of our research in terms of existing XAO instruments focusing on the improvements that can be done for HCI.

On Chapter 3, we present the key elements to study a CAO system for an 8-m class telescope. The 1st stage is assumed to feature a Shack-Hartmann Wavefront Sensor (SHWFS) and a DM controlling about 800 modes and running at 1 kHz frame rate while the faster 4 kHz 2nd stage features a Pyramid WFS (Ragazzoni and Farinato, 1999) and controls about 200 modes. We also analyze ways to optimize the system and study the lifetime of atmospheric residual speckles and their noise contribution in long exposures.

In Chapter 4, we improve the CAO system by adding a compensation scheme that we define as "disentanglement CAO". The idea behind the compensation scheme is to act like a woofer-tweeter configuration to deal with the high-frequency oscillations produced by the over-sampling in the 1st stage. We present how this trick can improve the overall performance by making the 2nd stage behave like a stand-alone stage. In this chapter, we offer numerical simulations and performance evaluation for this new scheme using not only a simple integrator but also using an Linear Quadratic Gaussian (LQG) regulator on the 2nd stage.

Finally in Chapter 5, we present some conclusions and perspectives regarding our simulations with the CAO system and its control strategy. We discuss how these could be implemented in future instruments and how these studies can be further developed.

Chapter 2

Adaptive Optics Overview

2.1 Wavefront distortion and the AO concept

Generally in AO we represent the light wave by a complex number Φ, made of both an amplitude A and a phase ϕ:

$$\Phi = A \exp(-i\phi) \tag{2.1}$$

The amplitude and the phase are real numbers representing the fluctuation of the electric field. A surface with a spatially constant value of ϕ is called a flat *wavefront*, representing e.g. the light emitted by a distant star before entering Earth's turbulent atmosphere. Inside the atmosphere, the light speed is not constant, and it will vary as the inverse of the refractive index. Then, the flat-wavefront will no longer be flat, producing shifts in the phase. This wavefront phase fluctuation is related to the wavefront surface deformation by:

$$\phi = k \int n(z) dz \tag{2.2}$$

where $n(z)$ is the refractive index over the beam trajectory parametrized by z, and k is the wavenumber $k = 2\pi/\lambda$. Then, the main idea of AO is to compensate for these phase distortions with hopefully the opposite phase.

A basic AO system comprises three main components: a wavefront sensor, a wavefront corrector, and a controller (See Fig. 2.1). Light from a distant source will pass through the turbulent atmosphere and gets the wavefront distorted. When it reaches the telescope, the distorted wavefront will pass through a wavefront corrector (in most cases a deformable mirror), with the ability to compensate for the distortions. Then a beam splitter sends parts of the light to the wavefront sensors to measure the residual wavefront distortions. Finally, the controller will use the wavefront sensor measurements to update the control signals sent to the

wavefront corrector. A central property of the AO system is the frequency at which this closed-loop process is executed. This working frequency should be fast enough to compensate for the atmospheric disturbance changes. As the characteristic time of the atmospheric disturbance is generally considered to be 1 ms, framerates of about 1 kHz are typical for current XAO systems. For standard AO, framerates are generally in the range of 150 Hz to 1 kHz.

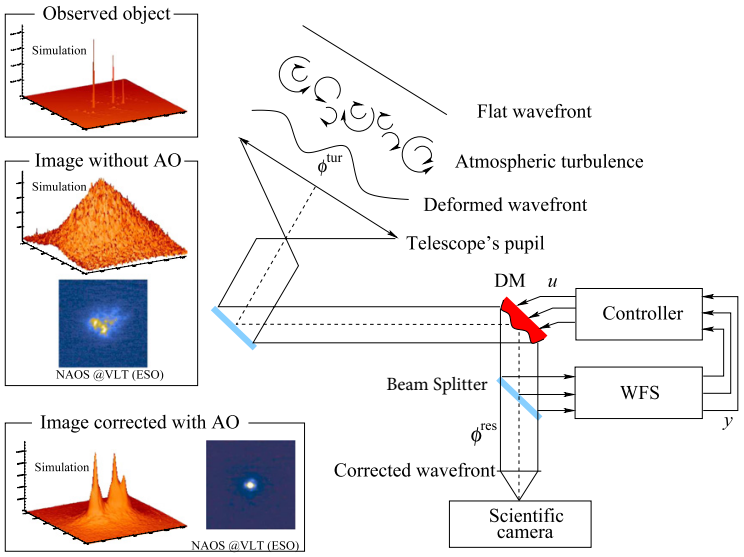

Figure 2.1: Standard AO setup: the wavefront deformation induced by atmospheric turbulence is compensated by a deformable mirror using closed-loop measurements. (From Kulcsár, Raynaud, Petit, and Conan, 2012)

In the following sections, we will describe all the components of a classical AO loop (See Fig. 2.2). First, we will introduce in Section 2.2 how atmospheric turbulence is characterized and describe in Section 2.3 how a turbulent phase can be represented using modal basis. In section 2.4 we present the principle of image formation and how performance can be evaluated. Then, we will focus in Section 2.5 on the two wavefront sensors (WFS) commonly used for astronomical AO: the Shack-Hartmann Wavefront Sensor (SHWFS) and the Pyramid Wavefront sensor (PWFS). Next, we will introduce in Section 2.6 the technology of deformable mirrors (DM). In Section 2.7 we present the basics of AO control with the integrator, and the basics of LQG control are presented in Section 2.8. Finally, we will introduce in Section 2.9 the eXtreme Adaptive Optics (XAO) concept and its fundamentals.

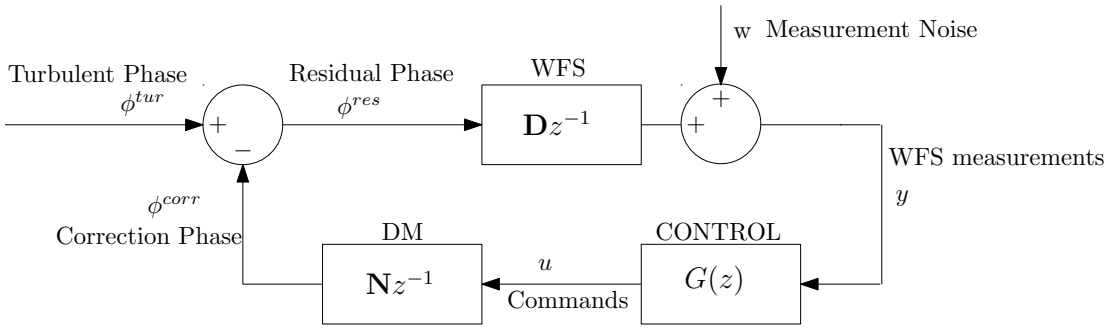

Figure 2.2: Block diagram of standard AO Loop, the matrices **D** and **N** represent the linear operations associated with the WFS and DM respectively. The operator $G(z)$ represents the controller transfer function, and z is the z-transform variable.

2.2 Atmospheric Turbulence

A proper understanding of how the atmosphere behaves and affects the phase is needed to compensate correctly for the wavefront aberrations. The aberrations produced by the atmospheric turbulence can be modelled as an stochastic process characterized by statistical parameters. The spatial statistical parameters define the so-called seeing conditions. This section will summarize our knowledge of the air refractive index spatial fluctuations and their translation into a phase deformation. More detailed information can be found in Roddier, 1999.

Fluctuations of air temperature produce density fluctuations which changes of the air refractive index over the beam trajectory $n(z)$ that distorts the wavefront and impacts the quality of the observations. Andrei Nikolayevich Kolmogorov considers the atmospheric turbulence an isotropic and spatially invariant process, and even though these are only approximations of the true phenomena, he proposed a stochastic model of the spatial evolution in his works from 1941 (Kolmogorov, 1941a; Kolmogorov, 1941b; Kolmogorov, 1941c),. Later, Theodor Von Kármán reformulated Kolmogorov's approximation in 1948 (von Kármán, 1948) by taking into account an inner and outer scale on which the energy is dissipated allowing to have a turbulent spectrum that does not diverge at zero frequency.

We are not interested in the absolute wavefront phase, but in the difference between the phase $\phi(\vec{x})$ at a point $\vec{x}$ in the telescope aperture, and the phase $\phi(\vec{x}+\vec{\xi})$ at the nearby point at a distance $\vec{\xi}$. Then, variance of the difference is the structure-function of the phase (Roddier, 1981):

$$D_\phi(\vec{\xi}) = \langle \mid \phi(\vec{x}) - \phi(\vec{x}+\vec{\xi}) \mid^2 \rangle = 6.88(\xi/r_0)^{5/3}, \tag{2.3}$$

where $\langle\rangle$ denotes the ensemble average (mathematical expectation) over $\vec{x}$ and r_0 is the Fried parameter given by the expression:

$$r_0(\lambda) = \left[0.423\left(\frac{2\pi}{\lambda}\right)^2 \int_0^\infty C_n^2(h)dh\right]^{-3/5}, \tag{2.4}$$

where $C_n^2(h)$ is the atmospheric turbulent strength and depends on the altitude h. The Fried parameter describes the effects of seeing at a particular wavelength. It corresponds to the aperture size over which the standard deviation of atmospheric turbulence wavefront error is ≈ 1 rad. A telescope without AO, with a diameter less than r_0, will be diffraction-limited when observing through the turbulence. In comparison, a telescope of diameter larger than r_0 will be seeing-limited and limited to a λ/r_0 angular resolution. Equation (2.4) reveals that r_0 is proportional to the $6/5$ power of the wavelength and decreases as the $-3/5$ power of the air mass.

We can also describe the atmosphere fluctuations using the spatial power spectrum under Kolmogorov statistics:

$$\Phi_n(\vec{k}) = 0.033(2\pi)^{-2/3}C_n^2(z)|\vec{k}|^{-11/3} \tag{2.5}$$

where $\vec{k}$ is a two dimensional spatial frequency vector. The Kolmogorov Power Spectral Density (PSD) diverges at when $k \to 0$ and does not account in particular for the effects of the outer scale. In practice one often uses the Von Kármán spectrum that includes the attenuation effect of the outer scale L_0 on low spatial frequencies:

$$\Phi_n(\vec{k}) = 0.033(2\pi)^{-2/3}C_n^2(z)\left[|\vec{k}|^2 + \left(\frac{1}{L_0}\right)^2\right]^{-11/6} e^{-(|\vec{k}|l_o)^2} \tag{2.6}$$

where l_o is the inner scale at which the turbulent energy is dissipated.

2.3 Modal representation of the phase

It is often convenient to expand the turbulent phase on a modal basis. The perturbed wavefront over a pupil can then be considered a superposition of several spatial modes of globally increasing spatial frequency.

Let us suppose a modal basis function $Z_k(\vec{r})$ defined on the whole aperture to decompose a given phase $\phi(x, y)$ on a set of modes given by:

$$\phi(\vec{r}) = \sum_{k=1}^{\infty} a_k Z_k(\vec{r}) \tag{2.7}$$

where a_k is the modal coefficient of the phase ϕ for mode k and for the basis function Z_k. The modal basis can always be made orthonormal over the pupil P:

$$\int_P Z_i(\vec{r}) Z_j(\vec{r}) d\vec{r} = \delta_{ij} \tag{2.8}$$

where the a_k coefficients are given by:

$$a_k = \int_P \phi(\vec{r}) Z_k(\vec{r}) d\vec{r}. \tag{2.9}$$

The most common modal basis to describe the phase is the Zernike basis. A detailed description of the Zernike basis applied to the atmospheric description can be found in Noll, 1976. Using polar coordinates $\vec{\rho} = (\rho, \theta)$, the Zernike modes are defined by:

$$\begin{aligned} Z_i(\rho,\theta) &= \sqrt{n+1} R_n^m(\rho)\sqrt{2} cos(m\theta) \quad \text{for } m \neq 0 \text{ and } i \text{ even} \\ Z_i(\rho,\theta) &= \sqrt{n+1} R_n^m(\rho)\sqrt{2} sin(m\theta) \quad \text{for } m \neq 0 \text{ and } i \text{ odd} \\ Z_i(\rho,\theta) &= \sqrt{n+1} R_n^0(\rho)\sqrt{2} \quad \text{for } m = 0 \end{aligned} \tag{2.10}$$

where

$$R_n^m(\rho) = \sum_{s=0}^{n-m+2} \frac{(-1)^s (n-s)!}{s![(n+m)/2-s]![(n+m)/2+s]!} \rho^{n-2s} \tag{2.11}$$

The Zernike modes are orthonormal over a circle of unit radius. They are ordered according to their radial order n and azimuthal order m, and the highest spatial frequency of a radial order n increases with n. The first few modes correspond to familiar optical aberrations, such as tip, tilt, defocus, astigmatism and coma (see Fig. 2.3). The mode $(0, 0)$ corresponds to piston and is not used.

Lets us suppose that the phase is represented by a final number of modes n_{modes}:

$$\phi(\vec{r}) = \sum_{k=1}^{n_{modes}} a_k Z_k(\vec{r}). \tag{2.12}$$

The spatial covariance matrix is then $\boldsymbol{A} = E(\boldsymbol{a}\boldsymbol{a}^t)$ where $\boldsymbol{a}$ is the vector containing the a_i coefficients and $E()$ denotes the mathematical expectation. The diagonal elements are the Zernike modes variance given by the approximate expression:

$$\langle a_i^2 \rangle = 0.294 i^{-1.9} \left(\frac{D}{r_0}\right)^{5/3}. \tag{2.13}$$

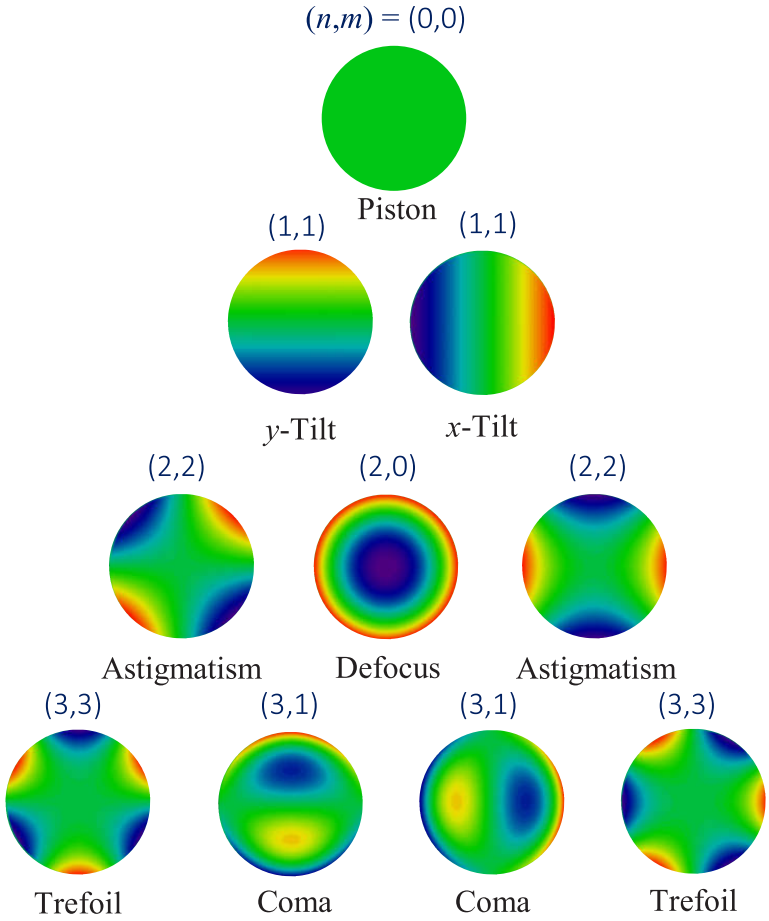

Figure 2.3: Illustration of the first ten Zernike polynomials

The covariance matrix $\boldsymbol{A}$ is not diagonal, the Zernike coefficients are thus not spatially statistically independent. A way of obtaining a diagonal covariance matrix is to use the so-called Karhunen-Loève basis, obtained through the diagonalization of $\boldsymbol{A}$.

Since the covariance is an Hermitian matrix, then there is always a matrix $\boldsymbol{U}$ such that $\boldsymbol{U}\boldsymbol{A}\boldsymbol{U}^\intercal$ is diagonal. The coefficients b_j of the K-L expansion are the components of the vector $\boldsymbol{b}$ given by:

$$\boldsymbol{b} = \boldsymbol{U}\boldsymbol{a}, \tag{2.14}$$

and then indeed the K-L covariance matrix is diagonal, so that the K-L modes are spatially statistically independent. Using equations. (2.14) and (2.12) and for a finite number of modes n_{modes}, then the phase can then be represented on the K-L basis by:

$$\phi(\vec{r}) = \sum_{k=1}^{n_{modes}} u_{k,j} b_j Z_k(\vec{r}) \tag{2.15}$$

where $u_{k,j}$ is the element (k, j) of matrix $\mathbf{U}$.

The K-L mode number k can be therefore defined as:

$$K_k(\vec{r}) = \sum_{j=1}^{n_{modes}} u_{k,j} Z_j(\vec{r}). \tag{2.16}$$

An illustration of a few K-L modes is given on Fig 2.4.

2.4 Image formation and performance criteria

When designing an AO system, it is essential to understand the relationship between the wavefront phase and the telescope aperture plane. When a wavefront represented by the equation (2.1) reaches the telescopes and passes through the aperture D, the light is diffracted. The complex amplitude A is then given by the Huygens' principle, which states that each point in the aperture can be considered as the center of an emerging spherical wave. In the far-field (i.e., in the case of Fraunhofer diffraction), the spherical waves are equivalent to plane waves, and we can write down the expression for the intensity in the focal plane as a function of the angular position α, known as the Airy disk:

$$Airy(\alpha) = \frac{\pi D^2}{4\lambda^2} \left| \frac{2J_1(\pi D\alpha/\lambda)}{\pi D\alpha/\lambda} \right|^2 \tag{2.17}$$

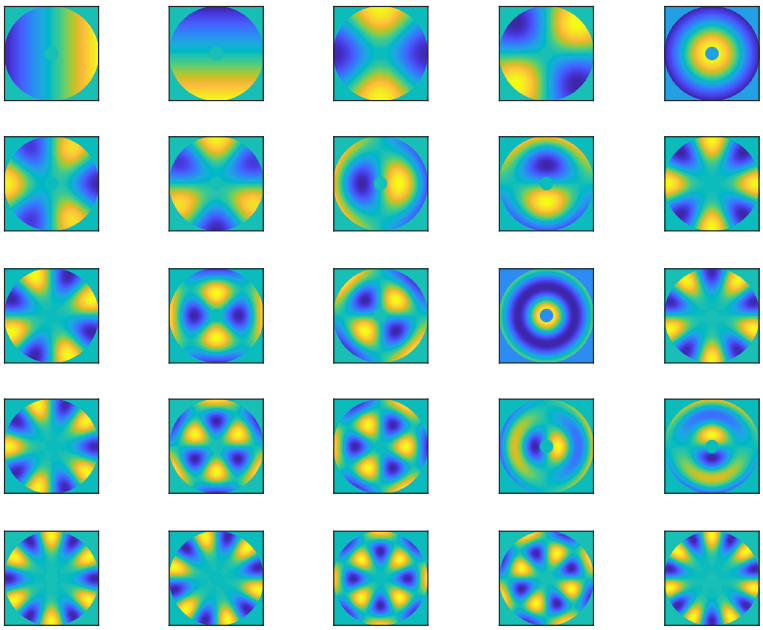

Figure 2.4: Illustration of the first 25 K-L modes for an atmosphere of $r_0 = 0.157$.

where its angular width is about λ/D. The intensity distribution of the response of a point source image is called the point spread function (PSF), and the Airy disk ends up describing the image of a point source produced by a perfect diffraction-limited telescope.

In the presence of atmospheric turbulence, the Optical Transfer Function $OTF(\boldsymbol{f})$, defined as the Fourier transform of the PSF, can be written as the product of two terms, the telescope transfer function $T(\boldsymbol{f})$ and the turbulence transfer function $A(\boldsymbol{f})$ (Roddier, 1981):

$$OTF(\boldsymbol{f}) = T(\boldsymbol{f})A(\boldsymbol{f}) \tag{2.18}$$

where $\boldsymbol{f} = \xi/\lambda$ is the spatial frequency in $[radians^{-1}]$.

If the telescope is diffraction limited, its transfer function will be given by the autocorrelation of the pupil transmission function. The atmospheric transfer function is given by:

$$A(\boldsymbol{f}) = \exp(-\frac{1}{2}D_\phi(\lambda\boldsymbol{f})) \tag{2.19}$$

where D_ϕ is the phase structure function of the atmospheric turbulence (See Eq. (2.3)). As a consequence, Roddier's expression shows that the PSF (which is the Fourier transform of Eq. (2.18)) is composed of two components: the influence of

the atmospheric turbulence and the influence of the static aberrations or diffraction effects.

The performance criteria used in this thesis to evaluate XAO performance are the Strehl ratio or wavefront error rms, raw PSF contrast and speckle lifetime, as detailed below.

2.4.1 Strehl ratio and wavefront error

A traditional criterion for image quality, not only in AO, is the Strehl ratio (SR). The SR is defined as the ratio between the peak image intensity of the PSF after correction I, to the peak intensity of a diffraction-limited PSF I_{dif}:

$$SR = \frac{I(0,0)}{I_{dif}(0,0)}. \tag{2.20}$$

In this case, the peak intensity of the PSF is located at the position $(0,0)$ which is the center of the PSF.

The SR ranges between 0 and 1 (or 0% and 100%), and can be approximated by a function of the variance of the residual wavefront $\sigma^2_{\phi^{res}}$ using the Mahajan approximation (Mahajan, 1982, 1983):

$$SR = \exp[-\sigma^2_{\phi^{res}}]. \tag{2.21}$$

This approximation can be used with negligible error for SR $\gtrapprox 0.8$.

The standard deviation σ_{res} of the residual phase, also referred to as root-mean-square error (RMS) or wavefront error (WFE), is also a way of evaluating the performance of the corrections in simulations and will also be used for evaluation in this thesis. A detail of the error terms that primarily determine this global error for the case of XAO can be found in section 2.9.1 dedicated to XAO error budget.

2.4.2 Contrast

Indeed, for planet finder instruments and in the XAO case, the residual halo of the PSF limits the detection of the planet, even for high SR (Guyon, 2018). Because of this, contrast levels between the core of the PSF and the halo gives a better estimation of the XAO performance. Indeed, for HCI with XAO, the photon noise of the central PSF intensity residuals at the location of the planet at its angular separation ultimately limits the detection sensitivity (Guyon, 2018). Hence, the intensity of the residual PSF as a function of angular separation and normalized to the central intensity is commonly called the **raw PSF contrast** and used as an HCI performance metric.

2.4.3 Speckle Lifetime

Another important parameter for HCI is the lifetime of speckles in the AO residual PSF. If we assume that the speckle noise would reduce with $1/\sqrt{t_{dc}}$, where t_{dc} is the speckle decorrelation time, a residual speckle halo with typical intensity contrast of about 10^{-5} would require 10^6 independent realizations to reach a level of 10^{-8} in the absence of other speckle correction techniques such as angular, spectral or polarimetric differential imaging. Depending on the speckle lifetime, accumulating that many realizations of the speckle pattern can be a very long process.

Long-lived quasi-static speckles are produced by instrument aberrations, which are left uncorrected by the AO system (Marois et al., 2003) and are one of the dominating factors affecting contrast, especially at low angular separations (Guyon, 2005). These residual aberrations can occur in the instrument's science camera optical path, which is not seen by the AO WFS, or in the optical path to the AO WFS, which is not seen by the science camera. Therefore they are called Non-common Path Aberrations (NCPA). NCPA change only slowly on timescales on which the instrument orientation and the gravity vector changes during an observation tracking a target in the sky. Also, temperature variations that produce thermal expansions in the instrument may introduce NCPA. Residuals from the atmospheric turbulence can induce a fast partial decorrelation of the PSF over a few seconds before transiting to a linear decorrelation regime at small angular separations (Milli, Mawet, et al., 2016b). A refined analysis further revealed another speckle decorrelation time scale of less than 2 ms, which can be attributed to the AO correction (Goebel et al., 2018).

Depending on the behavior of the CAO system, then we should see an effect on the speckle lifetime in the image plane. Therefore, we can apply an analysis (e.g. (Milli, Banas, et al., 2016)) on our simulated coronagraphic images and compare speckle lifetimes for single and double stage AO correction.

The analysis published by Milli, Banas, et al. (2016) analysed annular regions at different angular separations from the PSF center. For each region, we arranged the data in a matrix containing the evolution over time for each pixel. We can then subtract the mean intensity of each pixel and calculate the temporal autocorrelation functions. Finally, the autocorrelation functions can be averaged over all the pixels to derive the typical temporal correlation of the residual speckles in each region giving us an idea on how fast the speckles are decorrelating.

2.5 Wavefront sensors

In AO systems, the purpose of the wavefront sensors (WFS) is to measure the wavefront shape with the required spatial and temporal sampling (Campbell and

Greenaway, 2006). Because the wavefront phase does not interact with matter in any measurable way, WFSs typically use indirect methods to deduce phase information from intensity measurements at one or more planes.

Depending on where the detector is located on the optical path, wavefront sensors can be divided into pupil plane and image plane sensors. The most common WFSs used in AO are pupil plane WFSs; this includes the Shack-Hartmann wavefront sensor (SHWFS) and the pyramid wavefront sensor (PWFS). In this thesis, we will only consider pupil plane WFSs for the purpose of AO control.

The SHWFS and the PWFS behave quite differently in terms of linearity and sensitivity. By linearity of a WFS, we refer to the range for which the sensor response (relationship between the phase and the measurement) is linear. On the other hand, the sensitivity of a WFS refers to the slope of the sensor's response in linear range. In general, the SHWFS has a larger linear range and lower sensitivity, while the PWFS shows the opposite behavior. The PWFS is therefore a sensor of choice for AO correction with high performance requirements and is thus preferred for HCI cases.

2.5.1 The Shack-Hartmann WFS

The SHWFS has been the most used WFS for the development of AO. It uses the Hartmann method (1900), which was developed to test lenses and mirrors using an opaque mask with holes in it. Because the light passing through the optical object converges, these holes act as an aperture producing an array of dots. Then, the position of each spot is an indicator of the local wavefronts tilt at each hole. Shack (1971) improved the concept by replacing the holes with lenslets to focus the spot and optimize the light.

The SHWFS measures the local mean slopes of the wavefront of an incident light beam by imaging the light source through an array of lenslets, dividing the wavefront on the pupil plane into smaller subapertures. Each subaperture will image the source, creating a spot on the detector. If the wavefront is plane, then the lenslet will focus the spot on the optical axis of the corresponding lenslet. On the other hand, if the wavefront is disturbed, each lenslet will receive a locally tilted wavefront, producing an angular displacement α of the spot as it can be seen on Fig. 2.5.

The most straightforward technique to measure the positions of the SH images formed by the lenslet array is by using a four-quadrant detector for each subaperture. Another method widely implemented is the used of a Charge Coupled Device (CCD) camera to record better samples images of each spot.

Different methods (centroiding algorithms) to estimate the spot positions have been studied. A simple estimation is the center of gravity position (c_x, c_y):

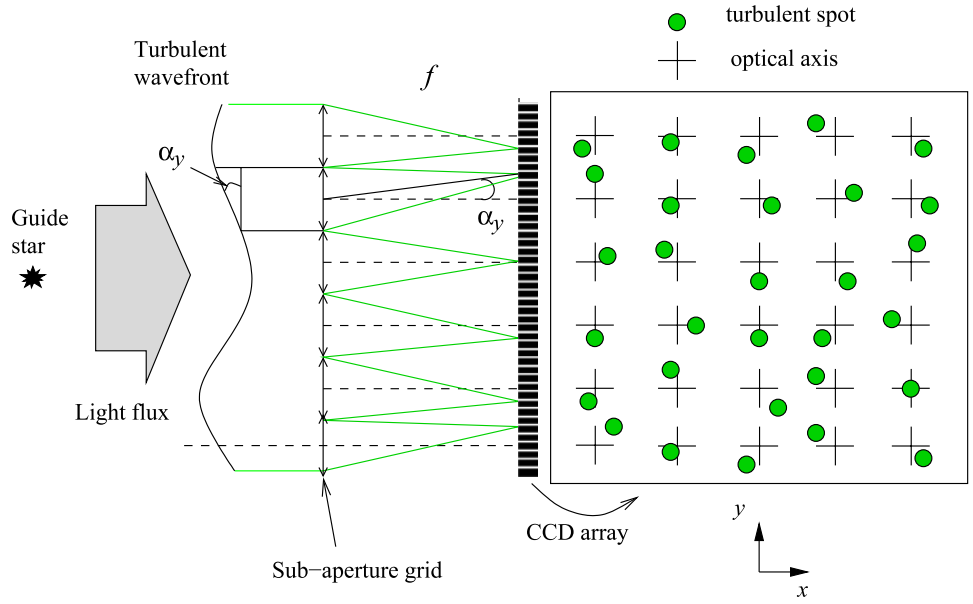

Figure 2.5: Principle of the Shack-Hartman WFS (from: Kulcsár, Raynaud, Petit, Conan, and Viaris de Lesegno, 2006)

$$c_x = \frac{\sum_{i,j} x_{i,j} I_{i,j}}{\sum_{i,j} I_{i,j}} \quad c_y = \frac{\sum_{i,j} y_{i,j} I_{i,j}}{\sum_{i,j} I_{i,j}} \tag{2.22}$$

where $I_{i,j}$ and $(x_{i,j}, y_{i,j})$ are respectively the intensity and the positions coordinates of the pixel (i, j).

The angular displacement gives a slope estimation over the subaperture of area A_{sa}:

$$S_x = \frac{c_x}{fM} \simeq \frac{\lambda}{2\pi A_{sa}} \int \frac{\partial \phi}{\partial x} dxdy \tag{2.23}$$

where f is the lenslet focal length and M the magnification between the lenslet plane and the telescope entrance plane. The same equation can be written for the y-axis.

The linearity of the SHWFS will depend on several parameters, including the type of centroiding algorithm used, spot dimension, pixel size, the level of noise, and the pixel scale that defines the portion of sky seen by each pixel on the detector (Thomas, Fusco, et al., 2006).

Using a correct combination of design parameters, the SHWFS allows maximizing the dynamical range and the turbulence strength that the sensor can linearly sense. Furthermore, the linear behavior of the SHWFS makes it particularly suited

for AO systems operating with Laser Guide Stars (LGS) (Thomas, Adkins, et al., 2008).

2.5.2 The Pyramid WFS

The current developments for future AO systems of the VLTs and ELTs, and the need for diffraction-limited WFS for XAO revealed the limitations of the SHWFS to reach the ultimate necessary performance (Guyon, 2018), but the AO community has been actively investigating new types of WFS capable of operating on a diffraction-limited image.

The most promising is the Pyramid Wave-front Sensor (PWFS) introduced by Ragazzoni (1996). The PWFS is a Fourier Filtering type of WFS (Fraanje et al., 2010), and it is based on the same principle as the Foucault knife-edge test used for optical lens testing. The principle of operation is shown in Fig. 2.6.

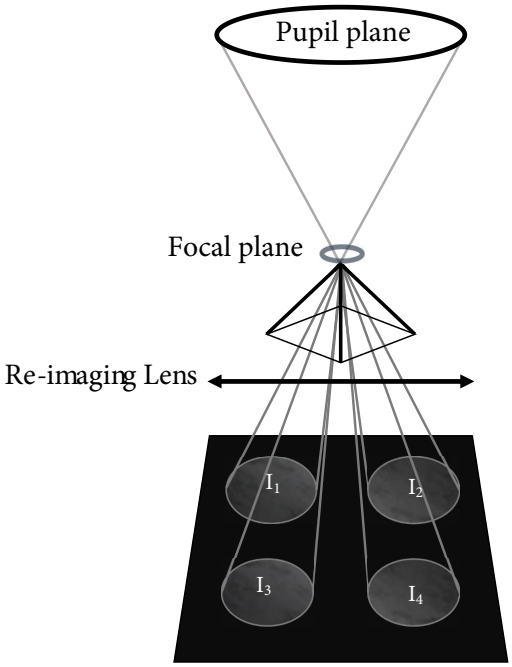

Figure 2.6: Schematic diagram of the PWFS concept. The reference source is imaged on the pyramid vertex, then light is deflected in four directions and re-imaged in four pupils over a detector.

A general formalism for Fourier based wavefront sensing applied to the PWFS can be found in Fauvarque et al. (2017), were the PWFS is treated as if a Fourier

mask m (see Figure 2.7) were located in a focal plane and we can filter the light from one pupil plane in to another. These masks are able to transform incoming phase fluctuations into intensity variations on a detector.

The lightbeam coming from the telescope is focused on the focal plane, where a four-face pyramidal prism is placed with its vertex at the focal point. The four faces of the pyramid deflect the light in different directions according to the wavefront slopes. A lens relay set after the pyramid is used to produce four images of the exit pupil on a CCD detector allowing for adjustments of the pixels across the pupils.

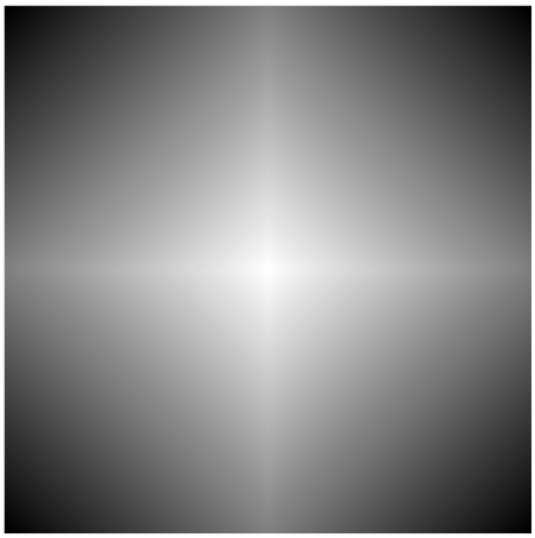

Figure 2.7: Mask m of a 4-sided PWFS with a phase angle of $\pi/2$.

Ragazzoni (1996) proposes to calculate the slopes using a quad-cell approach and with normalization of the signals by the total intensity in the selected PWFS pupils. Then in Vérinaud (2004) a global normalization using the spatially averaged intensity has been introduced and widely adopted by the community. The local slope S_x along the x-axis and the local slope S_y along the y-axis of an incoming wavefront are calculated using four equivalent sections in positions (x, y) in each of the four pupils with the expressions:

$$S_x(x,y) = \frac{I_1(x,y) - I_2(x,y) + I_4(x,y) - I_3(x,y)}{I_{glob}} \tag{2.24}$$

$$S_y(x,y) = \frac{I_1(x,y) - I_4(x,y) + I_2(x,y) - I_3(x,y)}{I_{glob}} \tag{2.25}$$

where I_{glob} is defined as:

$$I_{glob} = \frac{1}{N_s} \sum_{x,y} I_1(x,y) + I_2(x,y) + I_3(x,y) + I_4(x,y) \tag{2.26}$$

where N_s is the total number of valid sub-apertures. In the case of the PWFS, the number of sections in which each quadrant is divided is called "sub-apertures". Each sub-aperture will have a specific amount of pixels on the detector. The intensities in (2.26) will then correspond generally to the average intensities in each section. In the rest of the document, we will refer to the generic term "subaperture" for the PWFS sections or the SHWFS subapertures equivalently.

The Pyramid WFS Linearity

One particularity of the PWFS is that the signal response is only linear for small wavefront aberrations, roughly < 1 rad of amplitude. This can become problematic, especially in the presence of large residual phases. To overcome this difficulty, a solution proposed in Ragazzoni, 1996 consists in artificially increasing the size of the PSF imaged on the top of the pyramid using spatial oscillations in the focal plane. Such spatial modulation is usually achieved using a circular tip-tilt modulation as introduced in Esposito and Riccardi, 2001 which allows us to trade sensitivity and linear range through the modulation amplitude, a tuning parameter that the SHWFS concept does not provide (See Fig. 2.8).

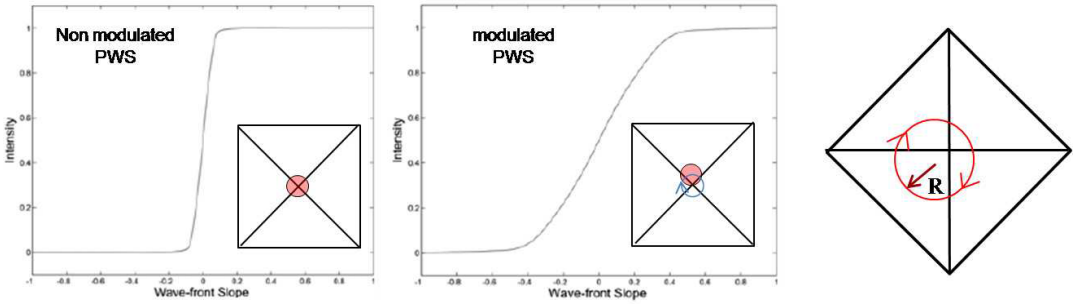

Figure 2.8: From left to right: Response of a non-modulated PWFS, of a modulated PWFS, and path of a tilted single ray due to tip-tilt modulation. On the x-axis we have the wavefront slope measurement and in y-axis the intensity.

Unfortunately a significant loss of sensitivity is associated with this linear range increase. Simulations done by Fauvarque et al., 2017 show that the sensitivity was linked to the time spent on the edges whereas the linearity range was correlated to the time spent on faces. They noted that the modulation inevitably makes the WFS PWFS chromatic, i.e., sensitive to the wavelength. Without modulation all

the sensors of the Pyramid class are rigorously achromatic. In this work, because the PWFS will be working in the 2nd stage AO loop, that is with hopefully small incoming wavefronts, we will not use any modulation in order to favor sensitivity.

Optical Gains

Another feature of the PWFS is that the residual wavefront errors have an impact on the sensor signal response function. This response function modification is mainly expressed through a spatial-frequency-dependent sensitivity reduction, a phenomenon named Optical Gain (OG) (Deo, Gendron, Rousset, Vidal, and Buey, 2018; Korkiakoski, Vérinaud, and Louarn, 2008).

This loss of sensitivity on sky is induced by the limited dynamic range of the PWFS, and the magnitudes of the OG will depend on the wavefront spatial frequency and the residual wavefront conditions. We can then write $\boldsymbol{G}(\phi^{res})$ as the optical gains of the PWFS for a given ϕ^{res}. This matrix is often assumed to be diagonal, and its coefficients are also called modal gains of the PWFS (Deo, Gendron, Rousset, Vidal, and Buey, 2018; Korkiakoski, Vérinaud, and Le Louarn, 2008). In Figure 2.9 we can see an estimation of the diagonal of $\boldsymbol{G}(\phi^{res})$ for different r_0 from (Heritier, 2019).

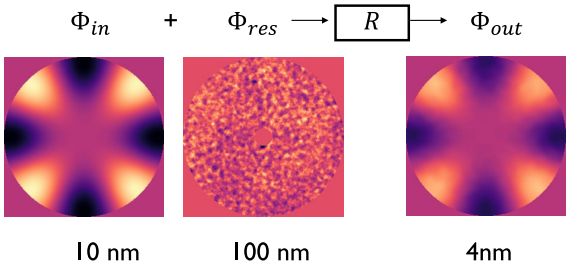

(a)

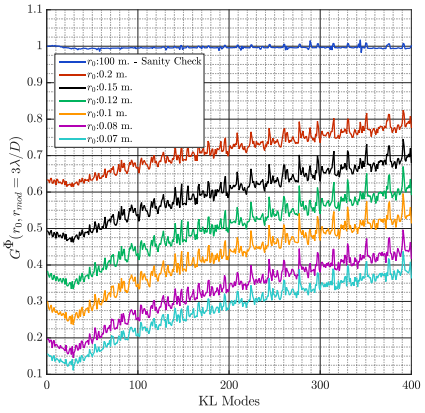

(b)

Figure 2.9: (a) Illustration of the impact of residual phase on the push pull measurement of the KL mode 20 using a PWFS. (b) Illustration of the Optical Gains of a PWFS modulated by $3\lambda/D$ as a function of the Fried Parameter r_0. From: Heritier, 2019

Errors induced by the OG can become predominant specially in bad seeing

conditions, so to take into account OG by estimation can be crucial in cases where the non-linear behavior is predominant. Also, OG are particularly critical for the handling of the aberrations located between the WFS and the science camera, which are not seen by the AO system. These are the so-called Non-Common Path Aberrations (NCPA), which are a highly investigated topic in the AO community (Esposito, Puglisi, et al., 2020; Esposito, Pinna, et al., 2015). The usual way to correct for NCPA's is to introduce a static offset in the WFS signal, but this methods assumes a linear behavior of the WFS which is not the case of the PWFS and the reference slopes are affected by the OG as an unforeseen difference of the acquired set point for the subtraction.

Some of the approaches to handle the OG during operations include adjusting the closed-loop gains to compensate for the sensitivity or even differentiate on selected spatial frequencies and determine the reduction of sensitivity (Esposito, Pinna, et al., 2015). Also, to apply a convolution model of the PWFS for the OG estimation was proposed by (Chambouleyron et al., 2020).

Other approaches suggest considering linearization of the PWFS signals around the AO residuals to identify the modal gains that depend on the observing conditions and provide a significant improvement of the AO performance by compensating for the OG (Deo, Gendron, Rousset, Vidal, and Buey, 2018; Deo, Gendron, Rousset, Vidal, Sevin, et al., 2019; Korkiakoski, Vérinaud, and Louarn, 2008). In the case of this thesis, we identify the optical gains using the method described in (Deo, Gendron, Rousset, Vidal, and Buey, 2018) using the attenuation in the reconstruction of each K-L mode produced by the OG, and depending on the controller, we include the optical gain values in the control calculations.

2.6 Deformable Mirrors

In order to compensate for the aberrations of the wavefront, we need a phase correction component, namely a DM. Some AO systems even use several DMs to achieve better results. A detailed review of the different technologies of DMs is available in the literature (Madec, 2012).

For XAO, the DM is usually located in the pupil plane of the AO system and consists in most cases of a main reflective surface under which are located actuators. These actuators represent the degrees of freedom of the DM, and they are controlled to produce a deformation of the DM's surface. The number of actuators will be associated with the system's level of performance, and for larger telescopes, a higher number of actuators is required. On the other hand, the actuators pitch (i.e. the distance between two neighbouring actuators) and the diameter of the pupil can constrain the DM selection.

For our modeling, we are considering the so-called Fried geometry (Fried, 1977)

for which the DM actuators are placed on the corners of each subaperture of the SHWFS or PWFS as illustrated in Figure 2.10.

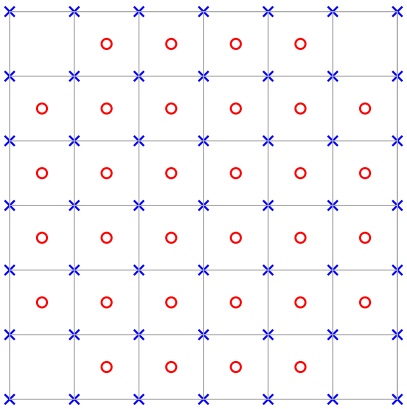

Figure 2.10: Illustration of an AO system with Fried geometry. Each actuator (blue crosses) falls over the corner of a subaperture of the SHWFS or PWFS, while the red circles represent the center of each subaperture. Because of this, in most cases if the number of subapertures in the diameter of the DM is N_{wfs}, then the number of actuators in the diameter will be $N_{act} = N_{wfs} + 1$.

The performance of the DM is not only determined by the number of actuators, but also from other characteristics that can determine or constrain the DM's ability for wavefront correction. The mechanical stroke defines the maximum range over which an actuator can move. The amount of stroke required depends on the standard deviation of the wavefront aberration. In the ideal case, we would like the DM to compensate for large tip-tilt aberrations, but this requires a high mechanical stroke, and a single DM is usually not enough to provide good correction for these aberrations and high order ones at the same time. Moreover, because of the highly unpredictable nature of the turbulence, the DM stroke specifications need margin to avoid saturation in case of high turbulence.

The shape of the DM surface under the effect of a single actuator is defined as its **influence function**. The shape of the influence function is commonly characterized by a Gaussian function, with the coupling efficiency providing the relative normalized height of the influence function at the position of a neighboring actuator.

Finally, the **temporal response** of the DM, or how fast the DM can converge to a requested shape, is driven by the AO loop frequency requirements. In terms of control of the DM, we assume throughout the document that the response of the DM is linear and that its time response is negligible with respect to the loop sampling period, so that it can be considered as instantaneous.

We can describe the correction phase ϕ^{corr} produced by the DM when a command u is sent as:

$$\phi^{corr} = \mathbf{N}u \tag{2.27}$$

where $\mathbf{N}$ is the influence matrix of the DM, and each column represents the influence functions of a single actuator in the chosen turbulent phase representation.

2.7 AO Control basics

In this section we will describe and explain the basics of a typical AO controller. We will consider for the sake of simplicity, a 2-frame delay system as illustrated in Figure 2.11. We will study the chronogram of an AO loop, and we will describe the most common controllers namely an integral action controller (or integrator) and a Linear Quadratic Gaussian (LQG) controller

2.7.1 Chronogram and models

In the chronogram presented in Figure 2.11, the different steps are described to illustrate the sequence of operations and to explain the 2-frames delay system. The frame (or sampling period) is denoted by T. Variables at time index k, $\forall k \in \mathbb{N}$, correspond to discrete times kT. In the closed-loop configuration (see Figure 2.2), the DM compensates for the wavefront errors of the incoming beam before it is measured by the WFS. The WFS therefore only measures the residual phase ϕ^{res}, that is, the difference between the current incoming wavefront and the correction ϕ^{corr} generated by the DM, expressed at time k, $\forall k \in \mathbb{N}$, by:

$$\phi_k^{res} = \phi_k^{tur} - \phi_k^{corr}. \tag{2.28}$$

In a 2-frame delay AO loop, and as the control is applied using a zero-order-hold, the correction phase writes:

$$\phi_k^{corr} = \mathbf{N}u_{k-1}. \tag{2.29}$$

The one frame delay in Eq. (2.29) accounts for the read-out of the WFS camera and the slopes and commands calculations (see Figure 2.11).

The residual phase thus writes:

$$\phi_k^{res} = \phi_k^{tur} - \mathbf{N}u_{k-1}. \tag{2.30}$$

The WFS integrates the optical flow over one frame T, introducing a delay of one frame. The WFS measurements are then modeled at time k by:

$$y_k = \mathbf{D}\phi^{res}_{k-1} + w_k \tag{2.31}$$

where $\mathbf{D}$ is the matrix representing the linear operation done by the WFS, and the noise w is the measurement noise mainly composed by photon noise and camera noise (Rousset, 1999), and it is assumed to be a white Gaussian noise. Then, the commands u_k applied at a time k are calculated using the measurements y_k.

As the time needed to read out the WFS camera, calculate y_k and u_k, transfer the data is also one frame, then the total loop delay is two frames.

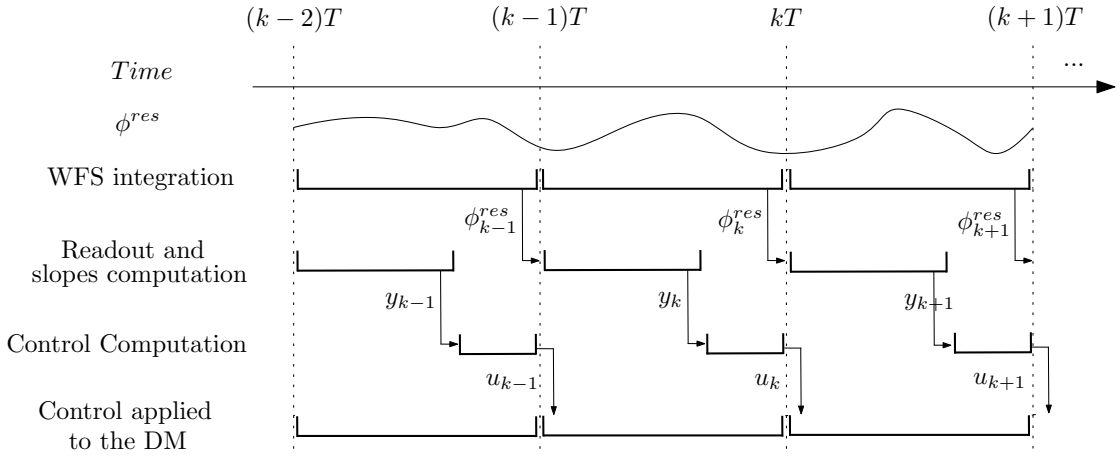

Figure 2.11: Chronogram of a two-frame delay AO loop. T is the duration of one frame and corresponds to the sampling period.

2.7.2 Integrator control

The most common controller used today in AO is the integrator. Its simplicity of implementation and stability tuning have provided benefits in AO since the very beginning of astronomical AO systems (Rousset et al., 1990). The integrator control is parameterized in its simplest configuration by a scalar gain g. The controller commands are updated at each iteration according to:

$$u_k = u_{k-1} + g\mathbf{M}_{comm}y_k, \tag{2.32}$$

where $\mathbf{M}_{comm}$ is the so-called command matrix that relates the WFS measurements to the commands values. The way it is obtained is explained below.

This controller provides a good attenuation of the low temporal frequencies and filters out the static aberrations. The value of g is tuned so that the AO performance is increased, while a value of $g < 1$ ensures the system's stability

for a two-frame loop delay. We describe hereafter how this matrix is obtained, including the case of modal control.

There is a linear relationship between the slopes space (or measurement space) and the actuator's space, and it can be expressed as:

$$y = \mathbf{M}_{int} u \tag{2.33}$$

where y are the WFS slopes measurements and $\mathbf{M}_{int}$ is called the **Interaction Matrix**. It is the mapping matrix between the DM and the WFS space, modeled as:

$$\mathbf{M}_{int} = \mathbf{DN} \tag{2.34}$$

where the matrices $\mathbf{D}$ and $\mathbf{N}$ represent the linear operations associated with the WFS and DM respectively (see Sections 2.7.1 and 2.6). The columns of the matrix $\mathbf{M}_{int}$ contain the measurements of the actuator's influence functions. Then inverting $\mathbf{M}_{int}$ should provide us with the necessary command matrix $\mathbf{M}_{comm}$:

$$u = \mathbf{M}_{comm} y. \tag{2.35}$$

However, the linear system that links actuators to slopes is over-determined (there are more measurements than actuators). Hence, $\mathbf{M}_{int}$ is non-invertible since it is not square. Moreover, $\mathbf{M}_{int}^{\intercal}\mathbf{M}_{int}$ is badly conditioned and its direct inversion is not suitable. There are many approaches to finding $\mathbf{M}_{comm}$ but the most common method is using the pseudo-inverse of the interaction matrix $\mathbf{M}_{int}^{\dagger}$ (Boyer, Michau, and Rousset, 1990):

$$\mathbf{M}_{comm} = \mathbf{M}_{int}^{\dagger} = (\mathbf{M}_{int}^{\intercal}\mathbf{M}_{int})^{-}\mathbf{M}_{int}^{\intercal} \tag{2.36}$$

where $()^{-}$ refers to a filtered inversion as explained below.

Usually, some sort of filtering is achieved by removing the shapes of the DM which are badly seen by the WFS, e.g., by a Truncated Singular Values Decomposition (TSVD) of the matrix $\mathbf{M}_{int}$ before the inversion.

The matrix $\mathbf{M}_{int}^{\intercal}\mathbf{M}_{int}$ is decomposed using SVD as:

$$\mathbf{M}_{int}^{\intercal}\mathbf{M}_{int} = \mathbf{UWV}^{\intercal} \tag{2.37}$$

where $\mathbf{U}$ and $\mathbf{V}$ are orthonormal matrices and $\mathbf{W}$ is the diagonal of the singular values. The filtered inversion is then:

$$(\mathbf{M}_{int}^{\intercal}\mathbf{M}_{int})^{-} = \mathbf{VW}^{-}\mathbf{U}^{\intercal} \tag{2.38}$$

where $\mathbf{W}^{-}$ is the diagonal matrix of the inverse singular values that have been kept, while the rest were set to zero.

We saw in section 2.3 that a modal basis could be used to describe the optical aberrations commonly seen in optics or those induced by atmospheric turbulence.

The choice of the modal basis can be dictated by different needs, and because of the diagonalization of the covariance matrix of the atmospheric turbulence, a K-L basis could be more appropriate in some instances. Moreover, the double orthogonalization to obtain the K-L basis ensures generating an orthonormal basis in the DM space that will contain the maximum of turbulent energy for a given number of modes considered (Gendron, 1995).

If we apply a set of calibration patterns in a zonal basis (a set of modal patterns with given coefficients) to the DM and we record the slopes vector produced on the WFS, then the modal calibration matrix $\mathbf{M}_{int}^{modal}$ is obtained. The modal interaction matrix converts the mode coefficients vector m into a slopes vector y:

$$y = \mathbf{M}_{int}^{modal} m. \tag{2.39}$$

The corresponding command matrix is then obtained directly as the pseudo-inverse of the modal interaction matrix $\mathbf{M}_{int}^{modal}$:

$$\mathbf{M}_{comm}^{modal} = \left(\mathbf{M}_{int}^{modal}\right)^{\dagger}. \tag{2.40}$$

Using this modal command matrix provides some advantages in terms of control as the inversion of the interaction matrix is often more stable when the badly seen modes by the WFS are removed from the modal basis.

2.8 Linear Quadratic Gaussian control

The linear Quadratic Gaussian (LQG) controller, has been implemented in two XAO systems, at the SPHERE (Petit, Sauvage, et al., 2014) on the 8-m VLT telescope, and at the Gemini Planet Imager (GPI) at the 8-m Gemini South telescope (Poyneer, Palmer, et al., 2016).

It is a predictive controller based on a model of the AO system and of the turbulent phase. It is obtained as the regulator that minimizes the residual phase variance for a given turbulent phase model (Kulcsár, Raynaud, Petit, and Conan, 2012; Kulcsár, Raynaud, Petit, Conan, and Viaris de Lesegno, 2006; Le Roux et al., 2004). When the model is expressed under the form of a linear state-space representation with Gaussian noises, then the optimal LQG controller consists in projecting the estimation of the future phase value onto the actuators space; this phase prediction is obtained as the output of a Kalman filter.

The expression of the control criterion and the description of the different steps mentioned above are the purpose of this section.

2.8.1 From continuous to discrete-time control

As explained in section 2.4, an appropriate performance criterion is the variance of the residual phase $\phi^{res} = \phi^{tur} - \phi^{corr}$. For long exposure time, this criterion can be defined in a quadratic form as (Kulcsár, Raynaud, Petit, Conan, and Viaris de Lesegno, 2006):

$$J^{c}(u) \triangleq \lim_{\tau \to +\infty} \frac{1}{\tau} \int_{0}^{\tau} \left\| \phi^{\text{res}}(t) \right\|^{2} dt. \tag{2.41}$$

The derivation of an equivalent discrete-time criterion for control design is detailed in the above mentioned reference. In this section we will summarize the main equations.

Taking $\tau = KT$, then equation (2.41) can be rewritten as:

$$J^{c}(u) = \lim_{K \to +\infty} \sum_{k=0}^{K-1} \frac{1}{KT} \int_{kT}^{(k+1)T} \left\| \phi^{res}(t) \right\|^{2} dt. \tag{2.42}$$

Because $\phi^{corr}(t) = Nu_k$ for $kT \leq t < (k+1)T$ and using equation (2.28), then the continuous-time performance criterion in equation (2.41) can be written as:

$$J^{c}(u) = \lim_{K \to \infty} \frac{1}{K} \sum_{k=0}^{K-1} \frac{1}{T} \int_{kT}^{(k+1)T} \left\| \phi_{k+1}^{tur} - \mathbf{N}u_k + \phi^{tur}(t) - \phi_{k+1}^{tur} \right\|^{2} dt \tag{2.43}$$

where ϕ_{k+1}^{tur} is defined as the average of the turbulent phase over $[kT, (k+1)T)$:

$$\phi_{k+1}^{tur} \triangleq \frac{1}{T} \int_{kT}^{(k+1)T} \phi^{tur}(t) dt. \tag{2.44}$$

.

Because $\phi_{k+1}^{tur} - \phi^{tur}(t)$ is zero mean ovear each sampling interval, then

$$\begin{aligned} J^{c}(u) = & \lim_{K \to \infty} \frac{1}{K} \sum_{k=0}^{K-1} \left\| \phi_{k+1}^{tur} - Nu_k \right\|^{2} dt \\ & + \lim_{K \to \infty} \frac{1}{K} \sum_{k=0}^{K-1} \frac{1}{T} \int_{kT}^{(k+1)T} \left\| \phi^{tur}(t) - \phi_{k+1}^{tur} \right\|^{2} dt. \end{aligned} \tag{2.45}$$

The first term of equation (2.45) depends only on discrete-time variables, and this is our discrete-time quadratic performance criterion named J^{d} (Kulcsár, Raynaud, Petit, Conan, and Viaris de Lesegno, 2006):

$$J^d(u) = \lim_{K\to\infty} \frac{1}{K} \sum_{k=0}^{K-1} \left\| \phi_{k+1}^{tur} - \mathbf{N}u_k \right\|^2 dt. \tag{2.46}$$

The second term in equation (2.45) depends on the continuous time t, but not on the controller commands u, and it is called the **inter-sample variance** (ε^2_{sampl}) (De Souza and Goodwin, 1984; Kulcsár, Raynaud, Petit, and Conan, 2012):

$$\varepsilon^2_{sampl} \triangleq J^c(u) - J^d(u). \tag{2.47}$$

This inter-sample variance is the value of $J^c(u)$ that would be achieved if one could make $J^d(u)$ equal to zero. "Therefore, it should be regarded as an incompressible performance penalty resulting from the use of a discrete-time control with sampling period T" (Kulcsár, Raynaud, Petit, and Conan, 2012).

The design of a full information optimal AO controller can thus be done in discrete-time using the discrete-time criterion $J^d(u)$. This simply leads using equation (2.46) to:

$$u_k^{LQ} = (\mathbf{N}^\intercal \mathbf{N})^{-1} \mathbf{N}^\intercal \phi_{k+1}^{tur}. \tag{2.48}$$

2.8.2 Deriving the LQG regulator

In the real world, the future phase $\phi_{k+1}^{tur}$is unknown and the control u_k is computed using the controls and WFS measurements already available at time $t = kT$. This is the so-called "Incomplete information case". Then the stochastic separation theorem (See e.g., (Anderson and Moore, 1990)) can be applied: assuming that $\{\phi_k^{tur}\}_{k\in\mathbb{Z}}$ is a weakly stationary stochastic process and taking the expectation of the square norm in J_d, the optimal control then becomes:

$$u_k^{opt} \triangleq \arg\min_{u_k} \mathrm{E}\left(\left\| \phi_{k+1}^{tur} - \mathbf{N}u_k \right\|^2 | \mathcal{I}_k \right) \tag{2.49}$$

with $\mathrm{E}\left[\cdot|\mathcal{I}_k\right]$ representing the conditional expectation with respect to past information $\mathcal{I}_k$, and where

$$\mathcal{I}_k = \{y_0, \ldots, y_k, u_0, \ldots, u_{k-1}\} \tag{2.50}$$

is the set of all past measurements and control values available for the control computation u_k. The optimal control in the so-called incomplete information can thus be written as:

$$u_k^{\mathrm{opt}} \triangleq (\mathbf{N}^\intercal \mathbf{N})^{-1} \mathbf{N}^\intercal \hat{\phi}_{k+1|k}^{tur} \tag{2.51}$$

where the unknown value ϕ_{k+1}^{tur} is replaced by its minimum variance estimate $\hat{\phi}_{k+1|k}^{tur}$, i.e. the conditional expectation:

$$\hat{\phi}_{k+1|k}^{tur} \triangleq \mathrm{E}\left(\phi_{k+1}^{tur}|\mathcal{I}_k\right). \tag{2.52}$$

If ϕ^{tur} can be obtained as the output of a linear state model where all noises are Gaussian, then the minimum variance estimate $\hat{\phi}_{k+1|k}^{tur}$ is obtained as the output of the Kalman filter based on this state model, and the optimal control is a Linear Quadratic Gaussian (LQG) control. This LQG control minimizes the variance of the residual phase under the hypothesis that the turbulent phase model is correct.

The problem is to find an adequate linear stochastic model for the time evolution of the turbulence and from that, derive a state-space representation. A state-space representation of the turbulence phase and the AO system can be written in the form (Kulcsár, Raynaud, Petit, and Conan, 2012):

$$\begin{cases} X_{k+1} &= \mathbf{A}X_k + \Gamma v_k \\ \phi_k &= \mathbf{C}_\phi X_k \\ y_k &= \mathbf{C}X_k + w_k - \mathbf{M}_{int}u_{k-2} \end{cases} \tag{2.53}$$

where

- $\mathbf{A}$ is the state matrix of the stochastic disturbance model
- $\mathbf{C}_\phi$ is the matrix that extracts the corresponding turbulent phase from the state vector X_k
- $\mathbf{C}$ is the observation matrix embedding the WFS operations,
- y_k is the measurement vector at time k,
- v_k is a Gaussian state noise, temporally white and zero-mean with known covariance matrix Σ_v,
- w_k is a Gaussian measurement noise, temporally white and zero-mean with known covariance matrix Σ_w

From this state-space model, we can build an asymptotic Kalman filter which enables to recursively calculate the optimal prediction $\hat{\phi}_{k+1|k}^{tur}$. The Kalman filter takes the form:

$$\hat{X}_{k+1|k} = (\mathbf{A} - \mathbf{L}_\infty\mathbf{C})\hat{X}_{k|k-1} + \mathbf{L}_\infty(y_k + \mathbf{M}_{int}u_{k-2}) \tag{2.54}$$

where

$$\hat{y}_{k|k-1} = \mathbf{C}\hat{X}_{k|k} - \mathbf{M}_{int}u_{k-2}. \tag{2.55}$$

The optimal control then is:

$$u_k^{opt} = (\mathbf{N}^\intercal\mathbf{N})^{-1}\mathbf{N}^\intercal\hat{X}_{k+1|k} = \mathbf{P}\hat{X}_{k+1|k} \tag{2.56}$$

where $\mathbf{P}$ extracts the phase prediction from the predicted state $\hat{X}_{k+1|k}$ and projects it to the DM. The Kalman gain $\mathbf{L}_\infty$ is obtain by:

$$\mathbf{L}_\infty = \mathbf{A}\mathbf{\Sigma}_\infty\mathbf{C}^\intercal\left(\mathbf{C}\mathbf{\Sigma}_\infty\mathbf{C}^\intercal + \Sigma_w\right)^{-1} \tag{2.57}$$

which depends on the covariance asymptotic matrix of the estimation error Σ_∞. This matrix is calculated by solving the discrete-time algebraic Riccati equation:

$$\mathbf{\Sigma}_\infty = \mathbf{A}\mathbf{\Sigma}_\infty\mathbf{A}^\intercal + \Gamma\mathbf{\Sigma}_v\Gamma^\intercal - \mathbf{A}\mathbf{\Sigma}_\infty\mathbf{C}^\intercal\left(\mathbf{C}\mathbf{\Sigma}_\infty\mathbf{C}^\intercal + \Sigma_w\right)^{-1}\mathbf{C}\mathbf{\Sigma}_\infty\mathbf{A}^\intercal. \tag{2.58}$$

This equation is solved using the function **idare.m** already implemented in MATLAB that computes a unique solution of a discrete-time Riccati equation.

2.8.3 Controller implementation in state-space form

Even though the LQG represents some advantages in terms of temporal error reduction, the computational requirements may be still restrictive. That is why the most common controller for future AO systems is the integrator possibly combined with an LQG controller for the low-order modes (Petit, Sauvage, et al., 2014; Poyneer, Macintosh, and Véran, 2007; Zidi et al., 2022b)

However, any linear and discrete-time AO controller can be represented in a state-space predictive form as:

$$x_{k+1}^u = \mathbf{A}^u x_k^u + \mathbf{B}^u y_k \tag{2.59}$$

$$u_k = \mathbf{C}^u x_{k+1}^u \tag{2.60}$$

where x_k^u is the state vector of the controller, y_k is the input of the controller (WFS measurements), and u_k is the command sent to the DM. Then, the dimensions of the matrices $\mathbf{A}^u$, $\mathbf{B}^u$ and $\mathbf{C}^u$ will depend on the controller and on the state vector.

For an LQG control, the implementation in state-space form from equations (2.54) and (2.56) is obtain by taking:

$$x_k^u = \begin{pmatrix} \hat{X}_{k|k-1} \\ u_{k-2} \end{pmatrix} \tag{2.61}$$

On the other hand, for the integrator, it is immediately checked that taking:

$$\begin{aligned} x_k^u &= u_{k-1} \\ \mathbf{A}^u &= \mathbf{C}^u = I \\ \mathbf{B}^u &= g\mathbf{M}_{comm} \end{aligned} \tag{2.62}$$

leads to the integrator equation:

$$u_k = u_{k-1} + g\mathbf{M}_{comm}. \tag{2.63}$$

Therefore, in the simulations, only the form given by (2.59) and (2.60) needs to be implemented as it embeds any linear controller.

2.9 Extreme Adaptive Optics

XAO systems are specifically optimized AO systems that deliver a superb wavefront correction on relatively bright natural guide stars. They generally run faster than regular AO systems and have more actuators and sometimes, even more sensors elements. And as a result, they deliver a high Strehl Ratio on bright stars.

This section will introduce XAO, how it was developed, the HCI science case that drives XAO, how HCI is done using XAO, the error terms associated with the contrast, and ongoing or future developments.

2.9.1 The XAO error budget

As mentioned before in this chapter, not only the total variance of the WFE is essential (and it constitutes a good way of evaluating the AO error budget), but also the raw PSF contrast defined by the structure of the WFE. In this section, we present a decomposition of the more dominant terms that contribute to the calculation of the raw contrast. We use the notation adopted in (Guyon, 2005) and based on the review done by Kasper (2021) which provides a thorough description and derivation of the error terms relevant for XAO.

The total raw contrast is obtained by adding each appropriate term. Then the overall contrast in terms of the angular separation θ is:

$$C = CP_{OHN} + CP_{OTEM} + CP_{UAMP} + CP_{ALIA} + CP_{WRON} + CC_{TOT} + CP_{FITT} \tag{2.64}$$

where CP_{OHN} is contributed by the optical pathlength difference (OPD) of the WFS photon noise, CP_{OTEM} by the temporal error, CP_{UAMP} by the uncorrected amplitude aberrations, CP_{ALIA} by the aliasing, CP_{WRON} by the readout noise and CC_{TOT} by the chromaticity.

This is for a system with a single WFS, no scintillation correction, and no additional loop.

Error budget terms derivation

According to Guyon (2005) and Kasper (2021), assuming paraxial approximation and a Fresnel propagation of the wave, the fraction of the atmospheric turbulence which produces phase errors is:

$$X(f,\lambda_i) = \frac{\int C_n^2(z)\cos^2(\pi z f^2 \lambda_i)dz}{\int C_n^2(z)dz}. \tag{2.65}$$

On the other hand, the fraction of the atmospheric phase that produces amplitude errors is:

$$Y(f,\lambda_i) = \frac{\int C_n^2(z)\sin^2(\pi z f^2 \lambda_i)dz}{\int C_n^2(z)dz} = 1 - X(f,\lambda_i), \tag{2.66}$$

where λ_i is the imaging wavelength and f the spatial frequency. Then, according to (Kasper, 2021), the contrast produced by uncorrected phase aberrations is:

$$C_{UPH}(\theta) = \frac{4}{\pi D^2}(\frac{\lambda_{r_0}}{\lambda_i})^2 X(\theta/\lambda_i,\lambda_i)W_\phi(\theta/\lambda_i), \tag{2.67}$$

and the contrast produced by uncorrected amplitude aberrations (i.e., **scintillation**) is:

$$CP_{UAMP}(\theta) = \frac{4}{\pi D^2}(\frac{\lambda_{r_0}}{\lambda_i})^2 Y(\theta/\lambda_i,\lambda_i)W_\phi(\theta/\lambda_i), \tag{2.68}$$

where $W_\phi(\theta/\lambda_i)$ is the phase power spectrum with outer scale L_0.

$$W_\phi(f) = \frac{0.023}{r_0^{5/3}}(f^2 + L_0^2)^{-11/6}. \tag{2.69}$$

Uncorrected scintillation creates speckles at 10^{-5} contrast levels for an 8-m telescopes. Most WFSs can measure this term and if corrected, this component is attenuated to well below 10^{-7} as shown by the terms C_{APHN} and C_{ATEM} in figure 2.12.

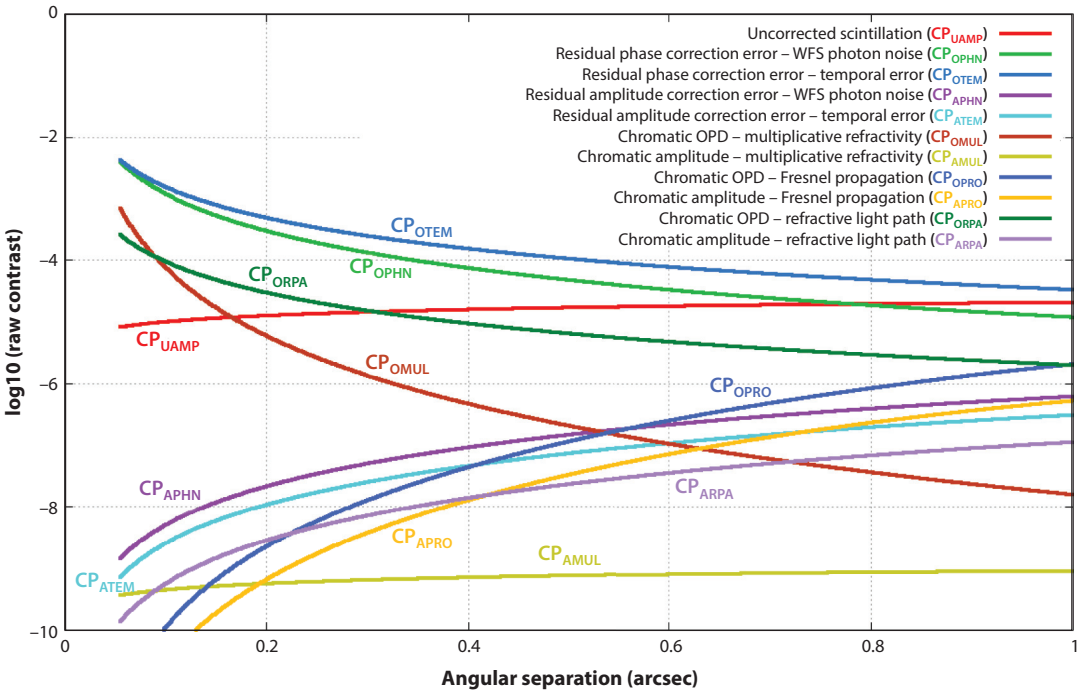

Figure 2.12: Simulated raw contrast contributions of XAO error terms for an 8-m telescope. WFS aliasing and readout noise are not considered. Perfect removal of the coherent long-exposure PSF is assumed to be achieved with the coronagraph (from: Guyon, 2018)

However, from figure 2.12 we can see that the most prominent error source is the **temporal delay error** CP_{OTEM} due to the finite temporal sampling of the wavefront sensor hence the time lag between the application of the DM command and the wavefront as measured by the WFS. Using the Taylor or frozen flow approximation for turbulence moving at speed v_w through a delay Δt, the term can be written as:

$$CP_{OTEM}(\theta) = (2\pi v_w \Delta t f)^2 C_{UPH}(\theta). \tag{2.70}$$

It limits the contrast in the most innermost regions with separations less than 100-mas to about 10^{-4} for 8-m telescopes. Also, as it was mentioned in section 2.7.1, the delay of the AO loop can significantly affect the performance (Guyon, 2018), and for XAO, the system speed must be of at least 1 kHz.

The temporal lag produces a wind-driven halo on the PSF that has been studied In Cantalloube, F. et al., 2020; Milli, Mouillet, et al., 2017 and can be seen in figure 2.13.

Another major contributor at small angular separations is the WFS **photon noise** CP_{OPHN}. It is proportional to the number of photons per sampling time, so it is also related to the system speed:

$$CP_{OPHN}(\theta) = (\frac{\pi}{\lambda_i})^2 (\frac{\lambda}{2\pi})^2 (\frac{\beta_p(\theta/\lambda)}{\sqrt{n_{phot}}})^2 \tag{2.71}$$

where the number of photons n_{phot} depends on the sampling time, the circular telescope aperture, and the source brightness (in $ph.s^{-1}.m$). The sensitivity factor β is relative to an ideal WFS that measures directly the wavefront modes (Guyon, 2018). When expressed in radians, it equals to the inverse square root of the number of photons available for the measurement. For the case of the PWFS (one of the popular choices for XAO system), $\beta = \sqrt{2}$ (Guyon, 2005).

Because the photon noise and the temporal error are related to the flux of photons available for the correction, then the loop speed must be carefully chosen to balance these two terms.

Even though it could be tempting to use faster frame rates as a straightforward approach to reduce temporal bandwidth errors, there is high price to pay. First, it increases **readout noise** error term CP_{WRON} noise error term. The readout noise can limit the reference star magnitude since the readout noise can be important for low magnitude objects. Secondly, it leads to higher demands on RTC computational power. Especially the second point presents important constraints. Then, a trade-off must be made between hardware availability, control algorithms, and degrees of freedom (number of DM actuators and WFS elements). Like we mention in section 1, one possibility is to run a high-order XAO loop at moderate speed

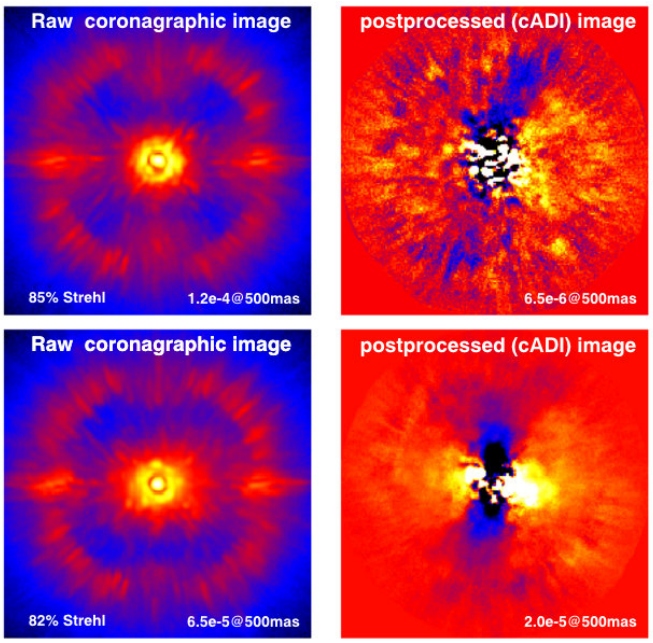

Figure 2.13: Examples of raw coronagraphic images of a few seconds exposures (left) and after applying classical Angular Differential Imaging (ADI) (right) on a 40 min sequence of pupil-stabilised observations. The first raw image illustrates the case of nominal conditions under a good seeing and coherence time, while the second raw image illustrates the case of a low coherence time due to high-altitude wind. Although the PSF elongation due to the wind is not clearly visible in the raw coronagraphic image because it is hidden in the speckle halo, the post-processed image reveals the typical butterfly pattern in the direction of the wind (here East-West, the predominant jet stream direction above Paranal) from: Milli, Mouillet, et al., 2017

and a low-order loop at high speed to efficiently correct low spatial frequencies. This is the approach we study in Chapter 3.

Advanced control schemes such as double integrator and/or predictive controllers can also enhance the overall rejection, in particular, in the low temporal frequency range, i.e., long-lived aberrations (see Section 2.7). On the other hand, the next generation of detectors (e.g., SAPHIRA or CMOS) allows a reduction of the delay by implementing a rolling shutter approach in which the DM update is done at a higher rate than the WFS readout.

If the WFS wavelength is different from the wavelength of the science camera then we have the introduction of **chromatic errors**. For the term associate with chromatic errors CP_{TOT} we will take in to account two main contributors. The chromaticity due to the refractive index CP_{OMUL} and due to a geometrical path through the atmosphere CP_{ORPA}. Then CC_{TOT} is:

$$CP_{TOT}(\theta) = CP_{OMUL}(\theta) + CP_{ORPA}(\theta). \tag{2.72}$$

When we perfectly correct at the WFS wavelength, then the imaging wavelength will show some residuals errors owing to the atmosphere´s refractive index chromaticity. Also, atmospheric dispersion creates a wavefront shear for high-altitude turbulence layers: the telescope beam footprint is laterally shifted with wavelength, creating a chromatic wavefront effect. The shift is on the order of 1 cm for high-altitude layers and zenith angle of 45 deg (Guyon, 2018).

In the end, chromatic errors are highly dependent on the conditions, the observing wavelength, and the zenith angle, and a comprehensive study of these chromatic effects is beyond this thesis's scope. Nevertheless, one can always minimize these chromatic effects by, for example, choosing an observing wavelength as close as possible to the WFS wavelength or using a precompensation mechanism in the case of refractive index chromaticity.

Another major contributor to the error budget when using fast WFS is the **fitting error** CP_{FITT}. The fitting error is due to the finite number of actuators of the DM, and it is directly linked with the actuator pitch $d = D/(N_{act} - 1)$, where N_{act} is the linear number of actuators on the telescope diameter D. On the other hand, the actuator pitch is directly linked with the DM correction radius as $\theta_{DM} = \lambda/(2d)$ which is the largest radial distance at which the DM can correct atmospheric speckles using its maximum spatial frequency. Decreasing d could be beneficial in terms of improving the coronagraphic image, but the larger the number of DM actuators, the larger the number of WFS subapertures and, hence, the smaller number of photons per subaperture and per frame (Fusco, Rousset, et al., 2006).

An expression for this term can be found in (Kasper, 2021) as:

$$CP_{FITT}(\theta) = H(\theta - \theta_{DM})C_{UPH}(\theta), \tag{2.73}$$

with H being the Heaviside step function, being equal to zero at $\theta < \theta_{DM}$ and equal to one otherwise.

Considering the rest of the error sources and the science requirements, a 40×40 actuator DM is a good compromise in terms of corrected area size, and the number of photons per subaperture. This corresponds to the actual design of the SPHERE DM (Fusco, Rousset, et al., 2006; Madec, 2012).

Finally, **aliasing** CP_{ALIA} could also be considered for the contrast calculation. The aliasing error is due to the finite number of wavefront analysis elements. Spatial frequencies higher than the inverse of half the subaperture size are folded by the WFS, so that high order spatial frequencies are misunderstood as low order frequencies. A way of mitigating aliasing is to reduce the subaperture size, to use a properly designed spatial filter (Poyneer and Macintosh, 2004), or applying super-resolution techniques (Oberti et al., 2022).

2.9.2 The wavefront sensor choice for XAO

One of the most fundamental limits in XAO is the guide star brightness. The XAO system must be able to sense and correct many modes, and in company with the turbulence, diameter, and wavelength, there can be limitations on the star magnitude. The selection of the XAO system components must comply with these requirements as they are the main drivers of the system design, and the selection of the WFS for XAO is crucial.

One of the most common WFS in use is the SHWFS. It is a well-proven mature technology that has already been implemented both by the Gemini Planet Imager (GPI) (Macintosh, Graham, et al., 2006), by the Spectro-Polarimetric High-contrast Exoplanet Research (SPHERE) at VLT (Beuzit et al., 2019a) and by Subaru Coronagraphic Extreme Adaptive Optics (SCExAO) at Subaru Telescope (Jovanovic et al., 2015). However, as was mentioned in section 2.5, the PWFS is the sensor of choice for closed-loop correction with small residuals like XAO and HCI. As it was mentioned before, the efficiency with which a WFS converts a fixed wavefront into a photometric signal varies between sensors, and the PWFS sensitivity gain over the SHWFS is significant, allowing fainter targets to be observed (Vérinaud et al., 2005). The PWFS is also less prone to aliasing effects than the SHWFS, although this can be mitigated by the use of an adjustable spatial filter (Milli, Mawet, et al., 2016b).

Even though there can be some linearity concern with the PWFS (see section 2.5), a good way to take advantage of its sensitivity is to use a two-stage scheme (see Chapter 3). That way, the aberrations that need to be corrected by the PWFS

are sufficiently small to stay in the linear regime.

Also, a correct choice of the sensing wavelength can be substantial. Wavefront sensing at a shorter wavelength will produce a stronger signal, and depending on the type star, the WFS should ideally operate in the visible light (Guyon, 2018).

2.9.3 Coronagraphy imaging

The role of a coronagraph is to block the starlight and let as much off-axis signal as possible pass through. A coronagraph typically uses an optical mask in the pupil and focal planes, and in the absence of wavefront errors, it must deliver an image essentially free of residual starlight.

Even though the coronagraph cannot remove speckles due to wavefront errors, it still reduces the photon noise of the diffraction pattern. Moreover, it prevents saturation at the detector by the PSF central core. At the 10^{-5} raw contrast level to be achieved by aggressive XAO systems, coronagraphs can deliver high $\gtrapprox 80\%$ throughput and small $\lessapprox 2\lambda/D$ inner-working angle, making it a perfect tool for exoplanet imaging for improving the raw contrast (Guyon, 2018).

Coronagraphs also address the coherent coupling or speckle pinning between the static and dynamic terms (Aime and Soummer, 2004; Bloemhof et al., 2001; Guyon, 2018; Soummer, Ferrari, et al., 2007). A complete review of state-of-the-art technologies of coronagraphy can be found in (Guyon, Pluzhnik, Kuchner, et al., 2006) and (Mawet et al., 2012).

In VLT/SPHERE, Gemini/GPI, and Subaru/HiCIAO, apodized Lyot coronagraphs are mainly used. They represent an evolution of the Lyot coronagraph to include an apodized entrance pupil to further improve the achievable contrast by removing the diffraction pattern (Milli, Mawet, et al., 2016a; Soummer, Aime, and Falloon, 2003).

Our simulations assume the theoretical concept of the **perfect coronagraph** (Cavarroc et al., 2006) where the coherent part of the wavefront is entirely removed before calculating the PSF. This is a reasonable simplification because several existing concepts come close to the perfect coronagraph at the contrast level of the XAO residuals which are of the order 10^{-5}.

2.9.4 Ongoing and next generation of XAO instruments

The first truly XAO order system was the PALM-3000 for the the 5-m Hale telescope at Palomar Observatory (Dekany et al., 2013). PALM-3000 had first light in June 2011 and was the first high order system deployed on-sky. It includes an IFS for exoplanet detection and characterisation using a 66x66 DM and a SHWFS running at 2 kHz. In late 2019 PALM-3000 underwent an extensive upgrade to its WFS and RTC system (Meeker et al., 2020).

The SPHERE instrument is an exoplanet imager belonging to the second generation instruments of the European VLT (Beuzit et al., 2019a). It started operations on 2014 and has three science channels: a differential imaging camera, a near-IR IFS and a visible light polarimetric imager (ZIMPOL). It's AO system SAXO (Sauvage et al., 2016) posses a 41x41 piezo-electric DM and a SHWFS running at 1.2 kHz. On the control side, it include an Optimized Modal Gain Integrator (OMGI) to control the DM and a LQG controller to manage the tip/tilt mirror. LQG allows optimal estimation and prediction of turbulent angle of arrival but also of possible vibrations (Petit, Sauvage, et al., 2014).

The US competitor of SPHERE is the GPI at the 8.2-m Gemini Telescope (Macintosh, Graham, et al., 2006). With similar capabilities, it also uses a near-IR IFS for exoplanet imaging and spectroscopy. The wavefront correction is done using a 50x50 MEMS DM with a woofer/tweeter architecture. It uses a spatially-filtered SHWFS with 44 subapertures across the pupil and it runs at 1 kHz. It also uses a three-mode LQG control (Poyneer, Palmer, et al., 2016), the higher modes being controlled by an integrator.

The SCExAO at the Subaru 8.3-m telescopes has been serving, both, as a science instrument and a test-bed for HCI technologies for ELTs (Jovanovic et al., 2015). Positioned behind the regular AO188, SCExAO utilizes several coronagraphs, including the Phase Induced Amplitude Apodization (PIAA) (Guyon, Pluzhnik, Galicher, et al., 2005) and a vector vortex. It also has two visible wavelength interferometric imaging modules know as VAMPIRES and FIRST. It is equipped with a 48x48 MEMS DM and uses a PWFS running up to 3.6 kHz.Fir control, it uses an optimal linear approach based on the Empirical Orthogonal Functions (EOF).

The MagAO-X is an XAO system for the Magellan Clay 6.5-m telescope (Males, Close, et al., 2018). First-light observation were conducted in December 2019 and it uses a 2040 actuators MEMS DM controlled at up to 3.63 kHz by a PWFS. It includes a vector Apodizing Phase Plate (vAPP) (Snik et al., 2012) coronagraph for Phase I and later for Phase II they will deploy a Phase Induced Amplitude Apodization Complex Mask Coronagraph (PIAACMC) with a Lyot Low-order WFS (Singh et al., 2017). It has plans to deliver high Strehl ratios ($> 70\%$), high resolution (19 mas) and high contrast ($< 1 \times 10^{-4}$) at 656 [nm]. It has a real time controller implemented based on a data-driven subspace predictive control (DDSPC) that uses directly the closed-loop residual without the need to a model of the turbulence (Haffert, Males, Gorkom, et al., 2022).

The ELT Planetary Camera and Spectrograph (PCS) will be the instrument dedicated to detect and characterize small nearby exoplanets from sub-Neptune to Earth-size in the neighbourhood of the Sun at the ELT (Kasper, Cerpa Urra, et al., 2021). The PCS concept is a derivation of the EPICS phase-A (Kasper,

Beuzit, et al., 2010) with improved strategies mainly on small inner working angles coronagraphy. PCS plans to combine XAO with coronagraph and high-dispersion spectroscopy to not only take direct images of nearby exoplanets, but also to look for biosignatures such as molecular oxygen in the exoplanets atmospheres. It plan to use the ELT's M4 mirror to pre-flatten the wavefront and use a second stage XAO system to further reduce the left-over turbulence. The high contrast raw image will then be fed by an array of single mode fibers to a high-dispersion spectrograph working in the red optical R- and I- band where the oxygen A-band is located. Several activities in R&D are already been conducted by ESO and the community, raging from XAO and predictive control methods to laboratory testing (Kasper, Cerpa Urra, et al., 2021). After conclusion of these activities, PCS could see it first light in the mid to late 2030s.

Chapter 3

The Cascade Adaptive Optics (CAO) system principle

3.1 Introduction

In Chapter 1 we presented the current state of the art in terms of HCI and XAO and how the contrast requirements become more challenging. We also mentioned how different approaches have been studied to minimize the AO-corrected residual halo. Then in Chapter 2 we reviewed the raw contrast error terms, how this can be quantified and how different techniques can reduce these errors. We also explained how temporal delay can dominate the overall wavefront error budget. In this Chapter, we focus on the Cascade Adaptive Optics (CAO) system that promises to be a good approach to reduce temporal delay error, but at the same time, introduce new capabilities to an already existing AO system that do not achieve the contrast requirement for certain XAO science cases.

We show that this system can be a good way to improve contrast performance of current XAO systems. The benefits of such a design is to reduce temporal error by using a small and fast DM in the 2^{nd} stage, minimizing the interventions in the hardware and software of the existing system, while increasing the number of degrees of freedom and speed of the combined system. The 2-stage CAO system is composed of two hierarchical loops. The 1^{st} stage corrects for the incoming turbulent phase, producing a residual phase that enters a faster second stage, resulting in an improved overall performance.

The advantages of this kind of system can be summed up in three main points: first, the second stage can be connected to any other already existing system; this can be especially helpful to reduce downtime of existing instruments and improve implementation time. Second, a CAO system reduces the stroke needed by the second stage DM to correct for low-order aberrations. Finally, the second

stage system can be designed and installed without modifying the first stage RTC, which is beneficial when the budget available for an upgrade is not sufficient for a complete overhaul.

The in-depth analysis of a CAO system corresponds to the article published in JATIS (Cerpa-Urra et al., 2022) and is the object of Section 3.2. We present the study of CAOs temporal and control properties using an integrator control for each stage. We also present the performance simulation results in a particular case of CAO for an 8-m class telescope, where performance is analysed in terms of residual phase RMS, contrast and speckle life-time.

The simulation environment, and in particular the way the CAO has been implemented using the Object Oriented Matlab Adaptive Optics (OOMAO) simulator (Conan and Correia, 2014), are presented in Section 3.3, and a conclusion in Section 3.4 motivates the developments in Chapter 4.4.

3.2 System Modeling and simulation of a CAO system: JATIS article

Cascade adaptive optics: contrast performance analysis of a two-stage controller by numerical simulations

Nelly Cerpa-Urra,[a,b,*] **Markus Kasper**,[a] **Caroline Kulcsár**,[b] **Henri-François Raynaud**,[b] **and Cedric Taïssir Heritier**[a]

[a]European Southern Observatory, Garching bei München, Germany

[b]Université Paris-Saclay, Institut d'Optique Graduate School, CNRS, Laboratoire Charles Fabry, Palaiseau, France

Abstract. The contrast performance of current extreme adaptive optics (XAO) systems can be improved by adding a second AO correction stage featuring its own wavefront sensor (WFS), deformable mirror (DM), and real-time controller. We develop a dynamical model for such a cascade adaptive optics (CAO) system with two stages each controlled by a standard integrator and study its control properties. We study how such a configuration can improve an existing system without modifying the first stage. We analyze the CAO architecture in general and show how part of the disturbance is transferred from low to high temporal frequencies with a nefarious effect of the second stage integrator overshoot and suggest possible ways to mitigate this. We also carry out numerical simulations of the particular case of a first stage AO using a Shack–Hartmann WFS and a second stage AO with a smaller DM running at a higher framerate to reduce temporal error. In this case, we demonstrate that the second stage improves imaging contrast by one order of magnitude and shortens the decorrelation time of atmospheric turbulence speckles by even a greater factor. The results show that CAO presents a promising and relatively simple way to upgrade some existing XAO systems and achieve improved imaging contrasts fostering a large number of science case including the direct imaging of exoplanets. © *2022 Society of Photo-Optical Instrumentation Engineers (SPIE)* [DOI: 10.1117/1.JATIS.8.1.019001]

Keywords: adaptive optics; extreme adaptive optics; cascade adaptive optics; speckle lifetime.

Paper 21066 received Jun. 18, 2021; accepted for publication Jan. 14, 2022; published online Feb. 15, 2022.

1 Introduction

Since the first detection of an exoplanet around a main sequence star more than 20 years ago,[1] the hunt for exoplanets has been more than prolific. Thousands of exoplanets have been detected[2] using mostly radial velocity (RV) and transit techniques and providing valuable information on a number of basic planet parameters, such as orbit, mass, size, and density. High-contrast imaging (HCI) with adaptive optics (AO), however, provides direct images of exoplanets that can be analyzed spectroscopically to characterize their atmospheres. HCI aims at reducing the 99% host star's light flux at the location of the exoplanet, thereby minimizing the photon noise and maximizing the detection sensitivity. It potentially reduces the required observing time to detect a planet from orbital period(s) for the indirect methods to just a few nights or even a few hours (depending on the exoplanet's apparent flux and the measurement noise). Although more than 99% of the planets discovered so far have been found indirectly, HCI led to the discovery of several young giant planets at relatively large orbital separations,[3–9] but extending the search space to lower mass and older exoplanets at smaller orbital separations has proved to be a challenge. In particular, HCI requires bigger telescopes and improved technologies (AO, coronagraphy, instrumentation) to boost contrast sensitivity at very small angular separations.

For optical and near-IR HCI, the AO-corrected residual halo stellar flux is the main source of measurement noise.[10] To obtain great contrast sensitivity for exoplanet imaging at small angular

*Address all correspondence to Nelly Cerpa-Urra, ncerpaur@eso.org

2329-4124/2022/$28.00 © 2022 SPIE

separations, it is therefore crucial to minimize this residual halo, which is typically dominated by the AO temporal delay at small angular separations.[11] A straightforward approach to reduce the temporal delay would be to run the AO system faster at the expense of increased detector read-noise.

Ultrafast AO systems for HCI are under development at several observatories, using either a single-stage,[12] a woofer-tweeter,[13,14] or a cascade adaptive optics (CAO) system with two stages[15–17] approach. In the latter case, a second AO stage with its own deformable mirror (DM), wavefront sensor (WFS), and RTC is added to the instrument behind a first stage AO system. This second stage only sees the residuals of the wavefront preflattened by the first stage and can therefore employ a DM with small actuator stroke. As the scientific interest is mostly at very small angular separations, the AO correction radius[18] can be small, and the number of actuators of the second stage's DM can be relatively low, leading to a compact design and moderate computational demands. These properties, and the possibility to develop and test the second stage standalone and retrofit it to an already existing first stage, make this approach very attractive for upgrades of existing AO systems, such as VLT-SPHERE[19] or VLT-AOF.[20]

Besides running fast, predictive control presents another way to reduce the temporal error. Predictive controllers have been proposed in the literature in many different forms,[21–34] and some on-sky tests have been performed.[35–39] With the greatly increased processing power and bandwidth of modern computers, predictive control has been recently brought back into the focus of AO engineering with integration in operational systems.[13,40–42]

In this work, we rather follow a simple approach and propose a CAO system with two stages, where each stage is controlled by a classical integrator. We introduce the generic CAO in Sec. 2 and study its temporal and control properties. In Sec. 3, we present numerical simulations of a particular CAO case for an 8-m class telescope. The first stage is assumed to feature a Shack–Hartmann WFS and a DM controlling about 800 modes and running at 1-kHz frame rate while the faster 4 kHz second stage features a pyramid WFS[43] and controls about 200 modes. This case roughly represents the considered upgrades of some VLT AO systems mentioned above.

We also analyze ways to optimize the integrator gains for both stages and how to best split the light between them. We demonstrate an improved low frequency rejection by CAO, which also reduces the lifetime of atmospheric residual speckles and their noise contribution in long exposures. A comprehensive discussion of these results is provided in Sec. 3.3.

2 *Two-Stage CAO System: Principle and Control Analysis*

2.1 *Principle and General Hypotheses*

The principle of the two-stage CAO system is shown in Fig. 1: the first stage corrects for the incoming turbulent phase, producing a residual phase that enters a faster second stage. The residual phase at the output of this second stage is sent to the science camera. The wavelengths of the two WFSs may be different and may be also different from that of the science camera. The nature of each WFS and their dimensions will be detailed when addressing performance evaluation in Sec. 3.2.

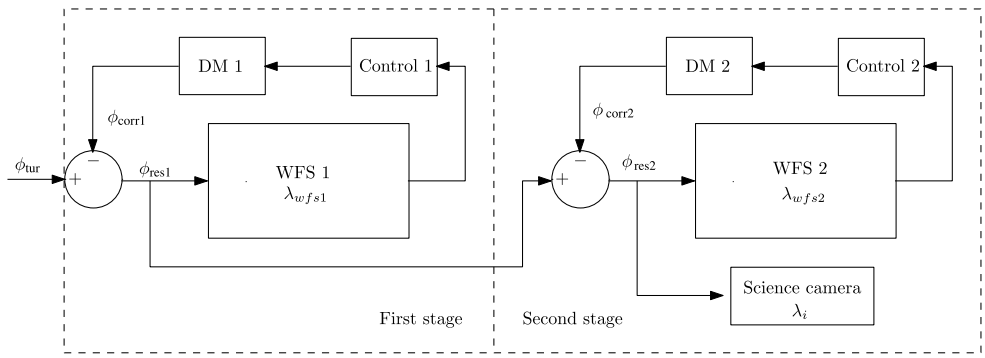

Fig. 1 Two-stage CAO system architecture.

The advantages of this kind of system can be summed up in three main points: first, the second stage can be connected to any other already existing system; this can be especially helpful by reducing downtime of existing instruments and improve implementation time. Second, a CAO system reduces the stroke needed by the second stage DM to correct for low-order aberrations. Finally, the second stage system can be designed and installed without modifying the first stage RTC, which is beneficial when the budget available for an upgrade is not sufficient for a complete overhaul.

Note that contrarily to standard CAO control, the second stage (inner loop) is not seen by the first stage (outer loop), so the stability of the inner and outer loops are sufficient to guarantee the stability of the CAO feedback. Each loop is controlled by an integral action controller (or integrator). Also, we will consider in the following that each WFS integrates the flux over one frame, T_1 for the first stage T_2 for the second stage, and that the two loop frequencies $F_1 = 1/T_1$ and $F_2 = 1/T_2$ are such that the second stage frequency is a multiple of the first stage frequency, that is, $F_2 = nF_1$, $n > 1$, $n \in \mathbb{N}$. Also, we suppose that each loop suffers a standard two-frame delay.

As each loop is controlled by an integrator, two natural questions arise: does this two-stage CAO system behave like a double integrator in terms of rejection? And how to characterize the rejection for such a system with two different frame rates? The purpose of the next section is to address these questions due to a modal analysis.

2.2 *Modal Control Analysis*

In a standard AO loop, it is commonplace to analyze rejection by computing the frequency-domain response of the closed-loop controlled system. Once the frequency responses of the rejection transfer function (RTF) and noise propagation transfer function have been calculated, the effects on any incoming second-order stationary stochastic process with known power spectral density (PSD) can be evaluated, allowing in particular one to predict the expected value of the residual phase variance—see, Ref. 44 for the general case of linear controllers. These calculations rely on the hypothesis that the AO system is linear and time-invariant, so to a given input frequency corresponds an output at the same frequency, albeit with possibly a different amplitude and nonzero phase shift.

This is no more true in the case of a two-stage CAO system featuring two different sampling frequencies, as the system looses its time invariance property. Take the case of an incoming disturbance in which temporal spectrum contains energy between $F_1/2$ and $F_2/2$: this disturbance will be aliased by the first stage (with an attenuation due to the averaging by the WFS) at a frequency below $F_1/2$. In addition, the frequency range $[-F_1/2, F_1/2]$ will be periodized at period F_1, which has to be accounted for at the second stage level. Hence, one particular frequency of the turbulent phase entering the whole two-stage system will produce several frequencies at the output of the system, so the linearity in the frequency domain is lost: the RTF cannot be evaluated anymore as a point-by-point ratio of the output and input spectra.

We propose to analyze the rejection and noise propagation produced by this system due to a modal decomposition of the turbulent phase, leading to a simpler scalar temporal and frequency analysis on a single mode. All the simulations are carried out using Matlab-Simulink with DMs and WFSs having unitary gains.

To illustrate the multirate effect, let us take a pure sine wave with frequency $f_0 < F_1/2$ entering the noise-free CAO system. The first stage produces a correction signal at loop frequency F_1, and the continuous-time residual is averaged and upsampled by the second stage at loop frequency F_2. The frequency support $\{-f_0, +f_0\}$ of our initial disturbance spectrum will thus be modified into a support of the form $\{\pm f_0 + mF_1\}$, $m \in \mathbb{Z}$. Figure 2(a) shows the spectrum of the resulting signal at the output of the second stage over the range $[-F_2/2, +F_2/2]$ for a pure sinusoidal signal of amplitude 1 and frequency $f_0 = 40$ Hz and loop frequencies $F_1 = 1$ kHz and $F_2 = 4$ kHz. The relative attenuation of the peaks at high frequency is due to the averaging filter convolution over T_2, which produces a sinc in the frequency domain. When $f_0 > F_1/2$, the resulting frequencies will be of the same form $\{\pm f_0 + mF_1\}$, $m \in \mathbb{Z}$, but only the aliased part of the signal will be corrected by the two stages, whereas the nonaliased part will only be corrected by the second stage. This is shown in Fig. 2(b) and explains the higher value at $\pm f_0$.

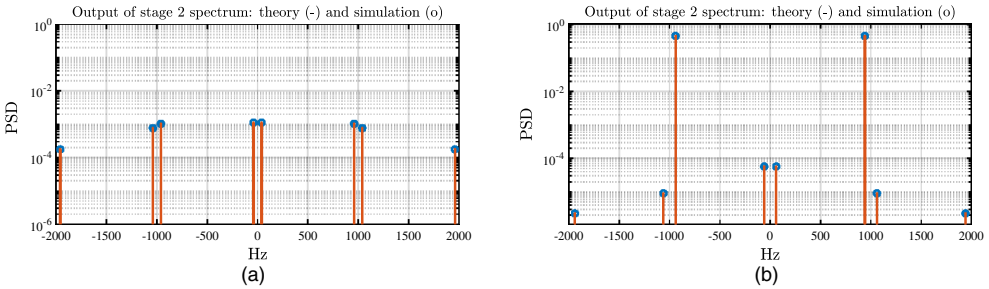

Fig. 2 Illustration of (a) spectrum periodization for an input sinusoidal signal at $f_0 = 40$ Hz and (b) of aliasing and periodization for an input sinusoidal signal at $f_0 = 940$ Hz. Loop frequencies are $F_1 = 1$ kHz and $F_2 = 4$ kHz. The red lines correspond to the theoretical calculations, the blue circles to the empirical PSD computed from the simulation data by nonaveraged periodogram. The y axis is in arbitrary units.

It is thus clear that the theoretical evaluation of the rejection for any given spectrum needs to distinguish what is rejected by both stages and what is only rejected by the second one.

To make this distinction, one can notice that any continuous-time signal ϕ^{tur} can simply be decomposed under the form

$$\phi^{\text{tur}}(t) = \phi^{\text{is}}(t) + \overline{\phi}^{\text{tur}}_k \quad \text{for } (k-1)\ T_1 \le t < kT_1, \tag{1}$$

where $\phi^{\text{is}}(t) = \phi^{\text{tur}}(t) - \overline{\phi}^{\text{tur}}_k$ is the so-called intersampling signal and $\overline{\phi}^{\text{tur}}_k$ is defined as

$$\overline{\phi}^{\text{tur}}_k = \frac{1}{T_1}\int_{(k-1)T_1}^{kT_1} \phi^{\text{tur}}(t)\mathrm{d}t. \tag{2}$$

The inter-sampling signal ϕ^{is} is not affected by the first stage, only $\overline{\phi}^{\text{tur}}$ is. Therefore, the analysis can be conducted by combining three operations:

- compute $\overline{\phi}^{\text{tur}}$, the signal averaged and sampled at T_1, to be rejected by the first stage running at F_1,
- compute ϕ^{is}, the intersampling signal to be compensated by the second stage only at F_2,
- periodize the residual spectrum of the rejection of $\overline{\phi}^{\text{tur}}$ by the first stage at frequency F_1 on $[-F_2/2, F_2/2]$ to obtain the first stage residual $\overline{\phi}^{\text{res},1}$, which is to be compensated by the second stage. The periodization is due to the upsampling at frequency F2, as $\overline{\phi}^{\text{res},1}$ is constant over T_1 and thus upsampled by repeating the same value F_2/F_1 times (effect of the second stage zero-order hold).

The intersampling signal for the second stage, obtained from ϕ^{is} using averages on T_2, has not been considered as it is not affected by the second stage.

The complete residual signal after first stage, namely $\phi^{\text{res},1} = \overline{\phi}^{\text{res},1} + \phi^{\text{is}}$, is compensated by the second stage to give a residual signal denoted by $\phi^{\text{res},2}$. These various signals ϕ^{is}, $\overline{\phi}^{\text{res},1}$, $\phi^{\text{res},1}$, and $\phi^{\text{res},2}$ are shown in Fig. 3 for the 40-Hz sinusoid with amplitude 1 and for $F_1 = 1$ kHz and $F_2 = 4$ kHz. The intersampling signal ϕ^{is} (in green) plus the residual $\overline{\phi}^{\text{res},1}$ (in pink) gives the signal $\phi^{\text{res},1}$ (in blue) to be compensated by the second stage. The residual signal $\phi^{\text{res},2}$ (in red) is obtained at the output of the second stage. It can be noticed that the intersampling signal seems to have a similar energy to that of the residual $\phi^{\text{res},2}$.

The rejection does not affect all these signals in the same way: if we denote by R_1 and R_2 the RTFs of stages 1 and 2, respectively, and considering the decomposition in Eq. (1) and the explanations given above, the PSD $S_{\text{res},2}$ of the residual signal at the output of the 2nd stage will be given by

$$S_{\phi^{\text{res}},2}(e^{i\omega T_2}) = |R_2(e^{i\omega T_2})|^2[S_{\phi^{is}}(e^{i\omega T_2})] + \mathcal{M}(|R_1|^2 S_{\bar{\phi}^{tur}})(e^{i\omega T_2}), \tag{3}$$

where $S_{\phi^{\text{is}}}$ and $S_{\overline{\phi}^{\text{tur}}}$ are the PSDs of ϕ^{is} and $\overline{\phi}^{\text{tur}}$, respectively, and $\mathcal{M}(G)$ is the periodized version of G with period F_1 on the interval $[-F_2/2, +F_2/2]$. To evaluate the rejection and

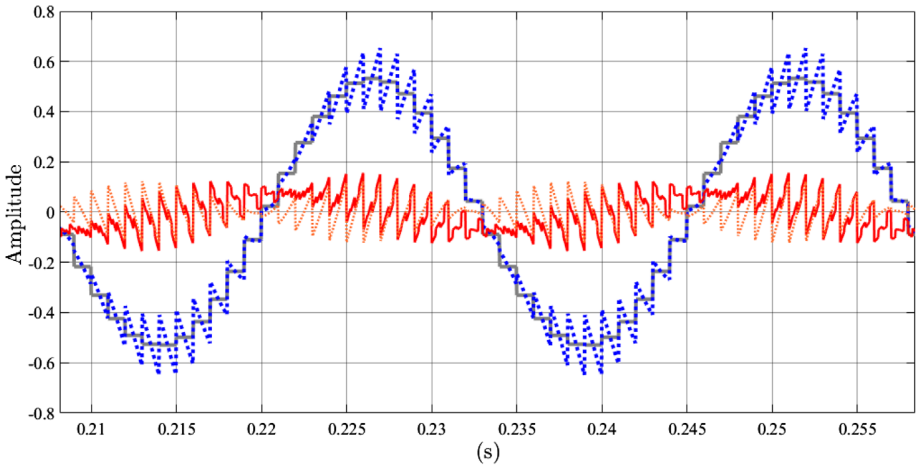

Fig. 3 For an input sinusoidal signal of amplitude 1 at $f_0 = 40$ Hz: intersampling signal ϕ^{is} (dotted orange), residual $\overline{\phi}^{\text{res},1}$ (plain gray), first stage output $\phi^{\text{res},1}$ (dotted-dashed blue) and second stage residual signal $\phi^{\text{res},2}$ (plain red). Loop frequencies are $F_1 = 1$ kHz and $F_2 = 4$ kHz. The y axis is in arbitrary units.

compare it with a double integrator at F_2, Fig. 4 shows the various RTFs that affect the signals passing through the system differently for $F_1 = 1$ kHz and $F_2 = 4$ kHz. The gains for the two integrators are 0.5, and the double integrator (with gain 0.0625) has been stabilized using a lead-lag term $1 + \alpha(1 - z^{-1})$ with $\alpha = 4$ to limit the frequency-domain overshoot. From Fig. 4, one can see that the two-stage CAO system will reject the low-frequency content of a signal like a double integrator until about 100 Hz. However, the intersampling signal (which is only rejected by R_2) has a spectrum that spreads until high frequencies because of F_1 periodization. It will thus not be well attenuated by the second stage and may even be amplified by the overshoot of the integrator. As for high-frequency and high-energy input signals above about 300 Hz, they are unlikely to be present in an atmospheric perturbation. The two-stage system is expected to have a better behavior in the range 180 to 300 Hz because it is well below the overshoot of the double integrator.

Let us take now the example of the temporal spectrum of a Zernike mode of radial order $n_{\text{rad}} = 3$, with cut-off frequency $f_c = 0.3(n_{\text{rad}} + 1)V/D = 1.5$ Hz ($V = 10$ m/s, $D = 8$ m).[45] The schematic PSD, second-stage residual PSD, and double integrator residual PSD are plotted in Fig. 5(a) for a case without measurement noise. The behavior of the second-stage system is similar or better than that of the double integrator for the part of the spectrum until about 600 Hz. The intersampling signal produces the two peaks at high frequency, leading to a global variance that is above the double integrator. In Fig. 5(b), it can be seen that the rejection of $\overline{\phi}^{\text{res},1}$ is to be improved at low frequencies, which is done well by the second stage as shown with the CAO

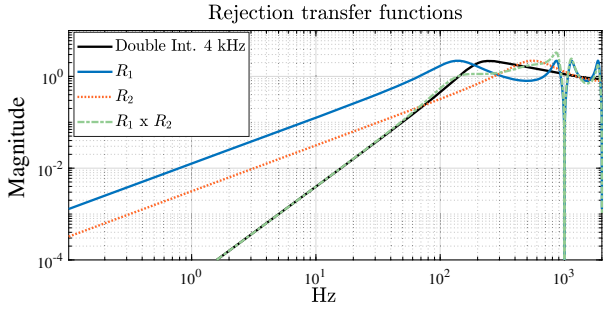

Fig. 4 RTFs over the frequency range $[0, F_2/2]$. The signal $\overline{\phi}^{\text{tur}}$ generated at $F_1 = 1$ kHz and upsampled at $F_2 = 4$ kHz is rejected by $R_1 \times R_2$, and the intersampling signal ϕ^{is} is only rejected by R_2. The double integrator RTF at $F_2 = 4$ kHz is in black. The y axis is in arbitrary units.

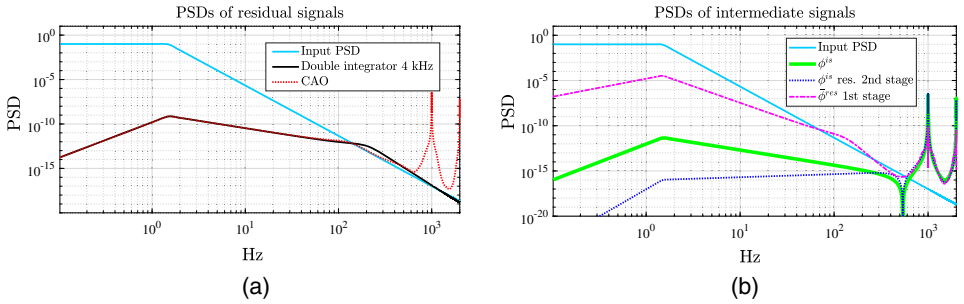

Fig. 5 Theoretical PSDs: (a) schematic input PSD corresponding to a Zernike radial order $n_{\text{rad}} = 3$, with cut-off frequency $f_c = 1.5$ Hz (plain blue), residual PSD $S_{\text{res},2}$ at the output of the second-stage CAO system with loop frequency $F_2 = 4$ kHz (dotted red) and residual PSD with a double integrator at $F_2 = 4$ kHz (black). (b) From top to bottom: input PSD (light blue), PSD of residual signal $\bar{\phi}^{\text{res},1}$ at the output of first stage with loop frequency $F_1 = 1$ kHz (dashed magenta), intersampling signal ϕ^{is} PSD (thick green), and PSD of the residual intersampling signal after rejection by the second-stage RTF R_2 (dotted dark blue).

curve in Fig. 5(a). The high frequencies of the intersampling signal ϕ^{is} stay almost identical after the second stage as they are not attenuated, as noticed previously in Fig. 3 and as it is shown in Fig. 4. The intersampling signal thus dominates the global signal in terms of variance, which can be computed using the equation in Ref. 29

$$\text{Var}(\phi^{\text{is}}) \underline{\text{a.s.}} \int_{-\infty}^{+\infty} (1 - |\text{sinc}(\pi f T_1)|^2) S_{\phi^{\text{tur}}}(f) \text{d}f, \tag{4}$$

where $S_{\phi^{\text{tur}}}(f)$ is the PSD of $\phi^{\text{tur}}(t)$. For this schematic spectrum, with $\text{Var}(\phi^{\text{tur}}) = 3.4$ arbitrary units [arb. units] over $[-F_2/2, F_2/2]$, one finds $\text{Var}(\phi^{\text{is}}) \simeq 1.4\,10^{-5}$ arb. unit when the variance of the residual signal at the output of stage 2 is $\text{Var}(\phi^{\text{res},2}) \simeq 2\,10^{-5}$ arb. unit. The double integrator is of course lower with a residual variance of about $4\,10^{-8}$ arb. unit.

When measurement noise is present, its propagation needs to be accounted for even in a very low noise situation, as shown in the following. The dimensioning of the first and second stages leads one to consider a similar noise variance for each stage, and a value of 410^{-4} arb. units has been chosen. This corresponds to a measurement noise variance about eight thousand times lower than that of the mode, which is a very high flux condition. We have tuned globally the two integrator gains of the CAO and also the gain and parameter of the double integrator and lead-lag filter to obtain the best residual variances: $6.0\,10^{-5}$ arb. units for the CAO and $3.9\,10^{-5}$ arb. units for the double integrator. The corresponding RTFs and noise propagation transfer functions are shown in Fig. 6. In Fig. 6(b), the transfer function of the first stage noise rejected by the second stage corresponds to the noise propagation transfer function of stage 1 multiplied by the stage 2 RTF [illustrated in dotted line in Fig. 6(a)]. It shows that the first stage gain cannot be set at a too high value because of the propagated measurement noise that attacks the second stage RTF. Even in a very high flux situation, as shown in Fig. 9(a) for a magnitude of 3, the first stage gain must be chosen not too high to limit noise propagation.

The theoretical residual phases PSDs when noise is present noise are shown in Fig. 7. The variance of the intersampling signal, $1.4\,10^{-5}$ arb. unit, becomes now moderate compared with the total residual variance of $6.0\,10^{-5}$ arb. units for the CAO.

In summary, this two-stage CAO controller with loop frequencies $F_1 = 1$ kHz and $F_2 = 4$ kHz, when applied to standard atmospheric perturbations, will generate high frequencies (the intersampling signal due to the presence of the first stage) from low-frequency signals. The intersampling signal variance depends on the turbulence strength, with high frequencies not well attenuated by the second stage because of the integrator overshoot. However, its impact is moderate in the presence of measurement noise; propagation has a decisive impact on global performance. The low frequencies (until about 20 Hz) will be on the other hand attenuated at the same level as that of a double integrator, and a better attenuation can be expected with the CAO at frequencies where the double integrator overshoots. We have also seen that the first stage

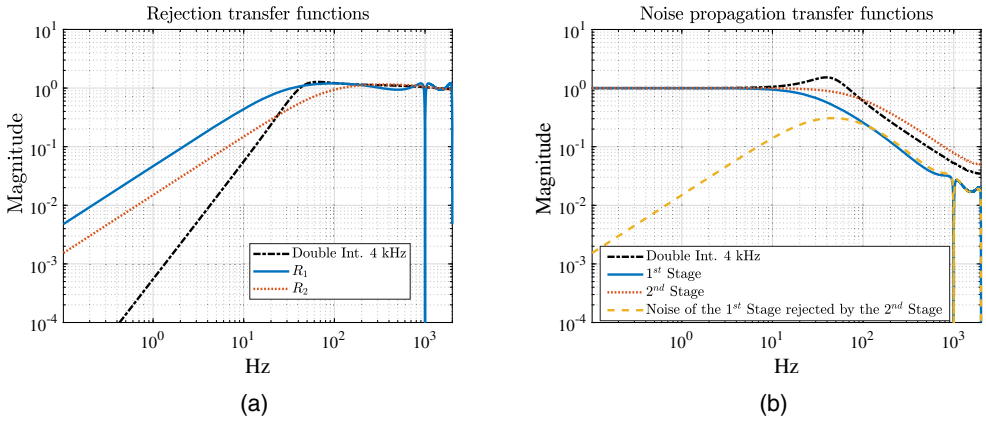

Fig. 6 Transfer functions. (a) RTFs with best tuning for each regulator: double integrator (dashed black line), first stage (blue line), and second stage (dotted red line). (b) Noise propagation transfer functions: double integrator (dashed black line), first stage (blue line), second stage (red dotted line), and first stage noise propagation rejected by second stage (yellow dashed line).

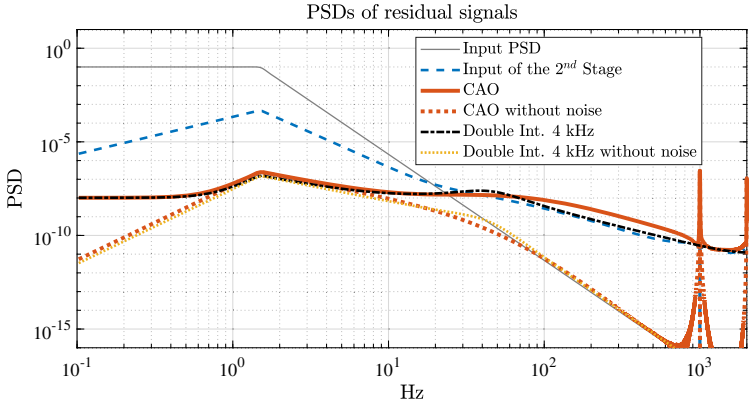

Fig. 7 PSDs in presence of a measurement noise variance of 410^{-4} arb. units: schematic modal input PSD (gray), input of the second stage including intersampling signal (dotted blue), residual at the output of the CAO (plain red and dashed-dotted red for the case without noise), residual for the double integrator (dashed-dotted black and dotted yellow for the case without noise). The peaks of the second stage input are at the same level than that of the CAO.

propagated noise enters the second stage as a disturbance, so the value of the first stage integrator gain should be chosen not too high.

The CAO will provide a better contrast than the single stage system with good correction at low angular separations (corresponding to low order modes and low spatial frequencies).[11] It is clear here that a regulator designed specifically to compensate the second stage input disturbance while limiting the second stage noise propagation should further improve the global rejection, which is left for future work. The two-stage system presented here is simple to tune, and its stability margins can be set separately in each loop by a proper choice of the two integrator gains. This modal control analysis has now to be completed by a performance analysis in terms of contrast and speckle lifetime, which is the purpose of the following section.

3 *Performance Simulations*

Operation and performance of a CAO system with two stages can be studied with the help of numerical simulations. As the CAO features two WFSs, we have to make assumptions about the WFS types, the framerate at which these are running, and the beam-splitting between the two. We choose the Shack–Hartmann sensor (SHS) to drive the first stage, consistent with the CAO

concepts for SPHERE+[16] and RISTRETTO,[17] which are currently in early development phases for ESO telescopes. The second stages of these concepts (and our simulations) are driven by a unmodulated pyramid WFS (PWS), which provides significantly better sensitivity and wavefront sensing accuracy than the SHS.[43] In particular, the advantage of a high-order AO system operated by a PWS is greatest near the image center, which is where most exoplanets appear and where the exoplanet science case benefits most from a better WFS.[11,46] The first stage's SHS is chosen to control about 800 Karhunen–Loève modes sampled by 36×36 subapertures at 1 kHz similar to what SPHERE SAXO[47] and the AOF provide.[20] The second stage's PWS has a twice coarser one-dimensional (1D) sampling (18×18) and controls 200 modes but runs four times faster (4 kHz) to efficiently reduce temporal error. These ballpark figures are consistent with what is considered for the second stage AO systems under development mentioned earlier.

We explore two different options for the beam-splitting between the two stages: (a) gray beam-splitting with a variable fraction of the I-band intensity distributed between the two stages and (b) dichroic beam-splitting with the first stage operating at a longer wavelength in the J-band and the second stage operating in I-band. These two beam-splitting cases are scientifically and technically motivated. The science case for SPHERE+ is focused on young stellar objects, and RISTRETTO is ultimately designed for the observations of Proxima b, which is an approximately Earth-mass planet orbiting our nearest neighboring star Proxima Centauri.[48] Temperate small planets were also found around several other very nearby stars,[49–51] and many more are expected to be identified by existing and future RV instruments.[52,53] The exoplanet host stars for these science cases, either very young or very nearby, are typically of a late spectral type and emit most of their flux in the I-band or longer wavelengths. This is also where important molecular lines can be found in the planetary spectra such as the A-band of molecular oxygen at 760 nm, which is the science wavelength we consider for our analysis. We choose the PWS of the second stage to operate in I-band to have it as close as possible to the science wavelength and minimize chromatic residuals.[11] The first stage WFS could then operate in the near IR, e.g., the J-band, and the light would be split between the two by a dichroic.

The first stage could also operate in I-band in which case a gray beam-splitter would be used. This would be a technically simple solution keeping the existing first stages of SPHERE and AOF, and we explore the best splitting ratio between the two stages hereafter. Table 1 summarizes the observation and instrument parameters used for the numerical simulations.

To simulate these CAO concepts, we use the AO simulation package OOMAO[54] running under Matlab, and we implemented an integrated solution for simulating both stages in a single simulation run. For this, we generate the input phase at the fastest frequency (in our case, 4 kHz) and input an average of four consecutive turbulent phase screens to the first stage (1 kHz) at every fourth step and update the first stage DM. Then, the residual phase generated by the first stage is sent as an input to the second stage at each step. This configuration allows us to take into account changes of the turbulent phase at the fast rate on the second stage. We will now describe how the two main operation parameters of the CAO, the beam-splitting ratio between the two stages and their integrator gains, were optimized.

3.1 *Optimization of Integrator Gains and Gray Beam-Splitting Ratio*

Depending on the WFS incident flux, the integrator gains must be adjusted for optimum performance. For simplicity, we assume a global gain for a given stage, but note that a modal gain optimization[55] can lead to an improved correction performance especially for faint stars. The incident flux on the WFS detector takes into account the assumed transmission to the detector listed in Table 1 and the WFS wavelength bandpass. For the dichroic beam-splitting, we assume a stellar with spectral type M5 (e.g., Proxima Centauri with I-J = 2.06) as a template red star, to calculate the flux intensities in the different bands. For example, a $J = 0.94$ and $I = 3$ star provides 15,710 and 2600 photons/subaperture/frame on stages 1 and 2, respectively. For the gray beam-splitting case, five different split ratios between the first stage and the second stage were simulated: 20%/80%, 35%/65%, 50%/50%, 65%/35%, and 80%/20%. For example, an $I = 3$ star observed with an 80/20 beam-splitter provides 2199 and 521 photons/subaperture/frame on stages 1 and 2, respectively. Here, the relative photon flux approximately corresponds to the split ratio, because the second stage has four times bigger subapertures than the first stage but runs four times faster.

Table 1 System parameters.

Atmosphere	
r_0	0.10 (m) and 0.157 (m) at 550 (nm)
L_0	25 (m)
Fractional r_0	[53.28 1.45 3.5 9.57 10.83 4.37 6.58 3.71 6.71]%
Altitude	[42 140 281 562 1125 2250 4500 9000 18,000] m
Wind speed	[15 13 13 9 9 15 25 40 21] m/s
Wind direction	[38 34 54 42 57 48 −102 −83 −77] $\times \pi/180$
Telescope	
Diameter	8 (m)
Secondary diameter	1.16 (m)
Photometric system	
I band	Wavelength: $0.790e-6$; bandwidth: $0.150e-6$
J band	Wavelength: $1.215e-6$; bandwidth: $0.260e-6$
Guide-star (Proxima Centauri)	
I-J color index	2.06
Apparent magnitude (J)	5.35
Apparent magnitude (I)	7.41
Science camera	
λ_i	I-band
First stage	
WFS	Shack–Hartmann
Order WFS	36×36
Control modes	800
n_{pix} camera	216×216 (pixels)
DM	37×37
λ_{wfs}	J-band or I-band
Transmission	0.2
QE	0.5
Readout noise	0.5 (electron per pixel)
Loop frequency F_1	1 kHz

Table 1 (*Continued*).

Second stage	
WFS	Pyramid
Modulation	Unmodulated
Order WFS	18×18
Control modes	200
n_{pix} camera	216×216 (pixels)
DM	19×19
λ_{wfs}	I-band
Transmission	0.2[a]
QE	0.5
Readout noise	0.5 (electron per pixel)
Loop frequency F_2	4 kHz

[a]The additional transmission losses for the second stage due to the slightly increased number of optical surfaces is negligible and the same transmission has been assumed for both WFS.

To determine the optimum gray beam-splitting ratio, we first individually optimize the integrator gains for both stages depending of the incident flux and split ratio. These results are shown in Fig. 8. Apart from the faintest stars, the best overall performance is obtained when 80% of the light is sent to the first stage and 20% is sent to the second stage for both values of r_0 evaluated. This reflects the higher sensitivity of the PWS when compared with the SHS. The second stage maintains a high performance on significantly lower photon flux than what is required for the first stage.

Then, we jointly optimize the gain values of both stages for both beam-splitting cases. To limit the size of the already large simulation parameter grid, we only consider the 80/20 split ratio for this analysis. The rationale for the joint optimization of the gains is that the PSD of the input disturbance to the second stage is modified by the RTF of the firts stage controller (as described in Sec. 2.2). A higher gain for the first stage will lead to better low frequency rejection but more overshoot at high frequencies. It therefore shuffles energy from low to high frequencies where

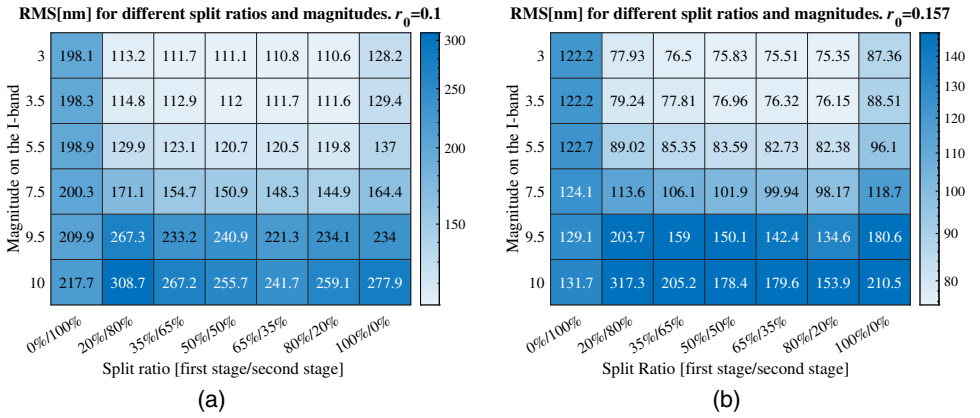

Fig. 8 Wavefront error (nm) for different split-ratios (gray beam-splitter case) and magnitude. (a) The simulation were done using $r_0 = 0.1$ m and (b) $r_0 = 0.157$ m. The darker the color, the bigger the WFE. In terms of RMS, the best overall performance is achieved using an 80%/20% split ratio for magnitudes up to 8 in I-band.

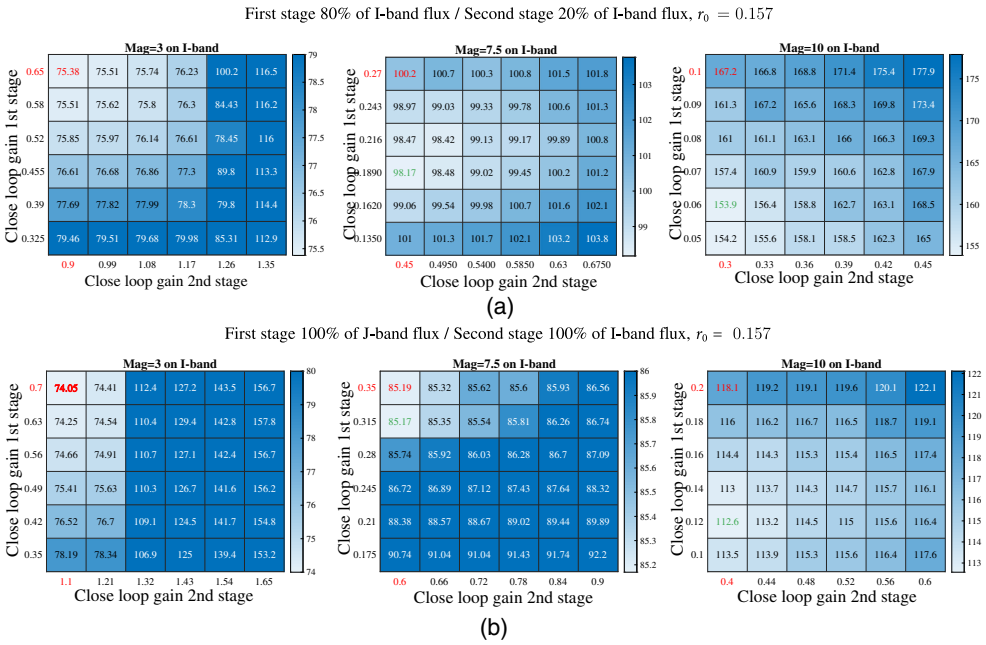

Fig. 9 Residual WFE (nm RMS) as a function of close loop gain and three different magnitudes. (a) The gray beam-splitting case using a 80%/20% split-ratio and (b) we assume a dichroic beam-splitter. The starting point of the joint optimization is the individually optimized gains shown in red with the corresponding WFE in the upper left corner. From there, we explored reduced stage 1 gains and increased stage 2 gains. The minimum residual WFE obtained by the joint optimization is shown in green. For the bright guide star case ($I = 3$), the individually optimized gains were already optimum.

the correction by the second stage is less effective. Hence, a first stage gain that optimizes its own residual wavefront variance may not lead to the minimum residual wavefront variance at the output of the second stage. Figure 9 shows example results of the joint gain optimization for a bright, a medium, and a faint guide star, respectively. For each magnitude, we diminish the first stage closed-loop gain obtained by the individual optimization from a factor 1 to 0.5 in 10% steps, and we amplify the second stage closed-loop gain obtained by the individual optimization from a factor 1 to 1.5 in 10% steps. The resulting gains for stages 1 and 2 are shown on the Y- and X-axes of the heatmaps, respectively. The results for the individual optimization of the integrator gains are shown in red, and the joint optimization results are shown in green. We see that in general, the joint gain optimization leads to a reduced first stage gain with respect to the individual optimization but maintains the second stage gain. For bright magnitude = 3 stars, there is no evident improvement in performance using the joint gain optimization probably because the high-frequency amplification mostly consists of noise, so the reduction of the fitting error of modes not controlled by the second stage is more relevant than the amplification of the low level of noise at high temporal frequencies.

Note that the optimum gains for the second stage include the optical gains of the PWS,[56,57] which are always smaller than one. Using a published method,[57] we calculate optical gain values ranging between 0.75 for $r_0 = 0.1$ m and 0.87 for $r_0 = 0.157$ m as shown in Fig. 10. The optical gains are relatively large because the second stage PWS only sees the residuals of the first stage and therefore operates in a very small residual WFE regime. Then, the pure integrator control gain would be obtained by multiplying the second stage gain with the respective optical gain.

3.2 *Residual WFE and Contrast Performance*

Having determined the optimum integrator gains and split ratios for the CAO system, we can now compare the performance of both splitting concepts and quantify the correction improvement provided by the second stage. For the gray beam-splitting case, 80% of the flux is sent to the first stage and 20% is sent to the second stage. This ratio is optimum for all but the faintest

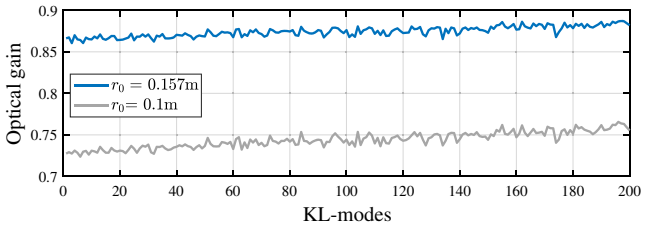

Fig. 10 Optical gains for the second stage PWFS as a function of the Karhunen–Loève modes for two different values of the Fried parameter r_0.

stars as shown in Sec. 3.1, and it is kept fixed because a single optical beam-splitters would not allow one to change the ratio depending on observing conditions. For the dichroic beam-splitting case, the star is assumed to have a red I-J color of 2.06, as motivated in Sec. 3.1.

Figure 11 shows the CAO systems' residual WFE after 10,000 iterations on the first stage (i.e., after 10 s of closed-loop operation) as a function of guide star I-band magnitude for good and median seeing values. Figure 11 shows that the CAO (orange-dashed line) consistently outperforms the single stage AO for all guide star magnitudes independently from how the beam-splitting is done. Not surprisingly, dichroic beam-splitting leads to a better correction performance overall because it provides more photons for each WFS individually, leading to a better correction performance overall. The curves exhibit the expected behavior of a rather constant bright guide star performance dominated by fitting error residuals and a degradation for fainter stars where measurement noise is dominating the error budget.

Besides the residual RMS WFE, the residual point spread function (PSF) contrast presents another important performance metric for HCI. We calculate the residual PSF from the residual WFE assuming that Airy diffraction pattern has been removed by an idealized perfect coronagraph.[58] The 1D residual PSF contrast is then given by the standard deviation of the flux intensities in a thin annulus of a given angular radius normalized by the peak intensity of the noncoronagraphic PSF.

Figure 12 shows the residual coronagraphic PSF and its contrast for the gray beam-splitting case in median and good seeing, and Fig. 13 shows the same for the dichroic beam-splitting case. The simulated observations represent the flux case of Proxima Centauri with $I = 7.4$, so neither very bright nor very faint. Imaging is done in I-band where the A-band of molecular oxygen is located. The improvement provided by the fast second correction stage is demonstrated by the better contrast in the controlled region of the second stage DM at separations smaller than about 9 λ/D. The second stage removes the elongated wind-driven halo,[59] which is a signpost for the

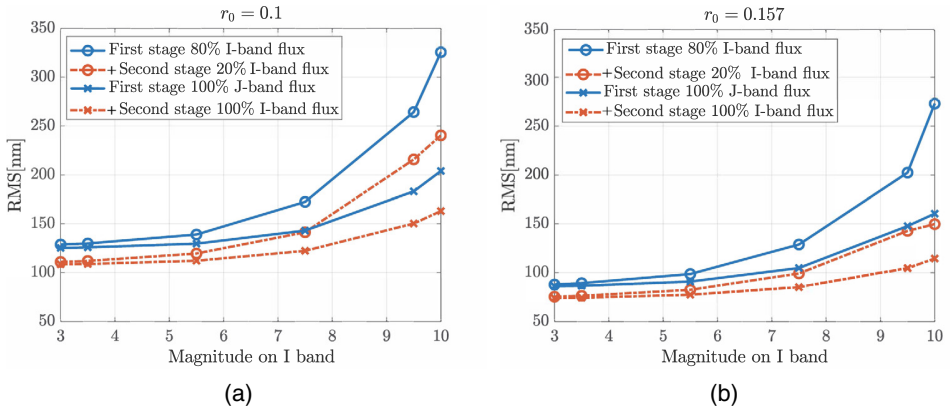

Fig. 11 RMS in nanometers in terms of magnitude for the first stage only (solid blue line) and with the second stage (dashed orange line) for (a) $r_0 = 0.1$ and (b) $r_0 = 0.157$. In the case where both WFSs work on the I-band, the full flux is divided in a 80%/20% split ratio between both stages (circle markers). In the other case, the flux is divided in different wavelengths for each stage, and 100% of the flux is sent (cross markers).

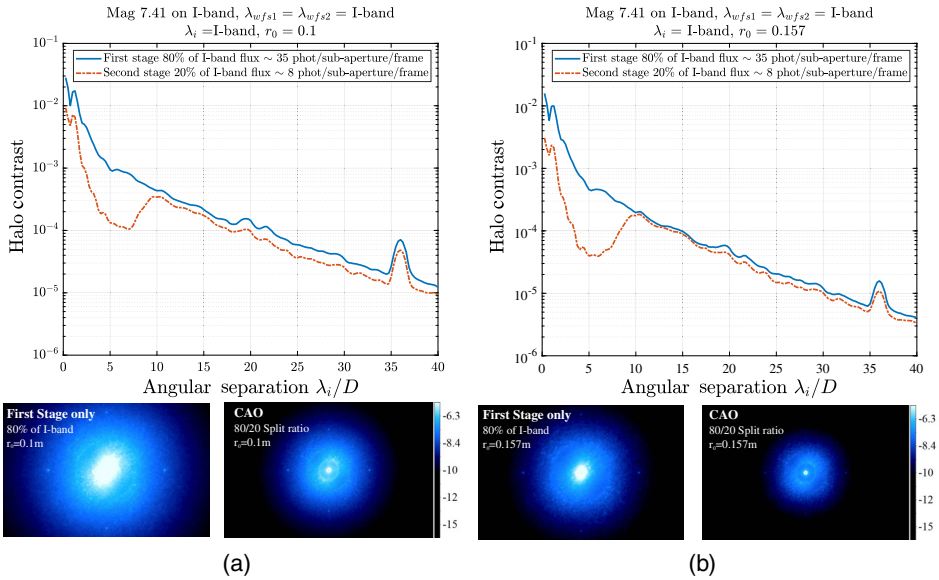

Fig. 12 Contrast performance and PSF for (a) $r_0 = 0.1$ and (b) $r_0 = 0.157$. Both stages operate their WFS in I-band, and the optimum gray beamsplitting ratio (80%/20%) was used. Scientific analysis is done in I-band as well.

temporal error of the AO and improves the residual halo contrast at these angular separations by almost one order of magnitude. This is consistent with the analytical prediction that the temporal error is proportional to $f_c^{-5/3}$ (with f_c denoting the correction frequency), so one would expect an approximately ten times improvement for a four times faster correction.

The best performance for the Proxima Centauri case is achieved by beam-splitting with a dichroic and reaches a contrast of 2×10^{-4} for good seeing at the maximum angular separations of Proxima b of about 40 mas or $2\,\lambda/D$ for an 8-m telescope observing at 760 nm as it is shown in Figs. 13 and 14. Such a contrast performance should allow us to detect oxygen in a hypothetical Proxima b atmosphere with an Earth-like composition in a few hundred hours.[60] Such an observation would require the AO WFS to work at a waveband slightly longer than I-band (e.g., between 800 and 950 nm) to send all the 760-nm photons to the spectrograph.

Using a PWS for the fast second stage combines several beneficial effects at the same time. It reduces temporal error, aliasing error,[61] and noise error.[11] The aliasing error of the first stage SHS[62] should be around 30- and 45-nm RMS for an r_0 of 0.157 and 0.1 m, respectively, while the temporal errors[63] for an assumed time delay of two frames, so 2 ms, should be 50 and 75 nm. The photon-noise-limited SHS centroiding error[64] assuming a noise propagation on n reconstructed modes proportional to $\log(n)$[62] yields about 50 nm RMS. Therefore, aliasing and photon noise cannot be neglected and a significant contrast improvement is already expected when adding a slow second stage with a PWS.

The yellow dotted line in Fig. 13 shows the simulated contrast from a "slow" 1 kHz second stage PWS. The reduction of aliasing and the higher sensitivity of the PWS compared to the SHS already results in a significant gain in contrast of a factors 2 to 3. Another factor 3 to 5 is then gained by running the second stage faster and reduce the temporal error as seen by the red dotted line on the same figure.

Figure 14 shows how the contrast at 40 mas is improved by the second stage as a function of stellar I-band magnitude. Again, the CAO system provides a contrast improvement of roughly one order of magnitude when compared with the single stage AO. Similar to the residual wavefront error shown in Fig. 11, we see that the correction and contrast performance degrade with stellar magnitude due to the increased noise and reduced optimum integrator gains. In contrast to the residual wavefront error, the contrast in the bright end does not level out because of a dominating fitting error that occurs at spatial frequencies beyond the correction radius of the AO and would not affect the contrast at small angular separations. We rather see that aliasing and residual

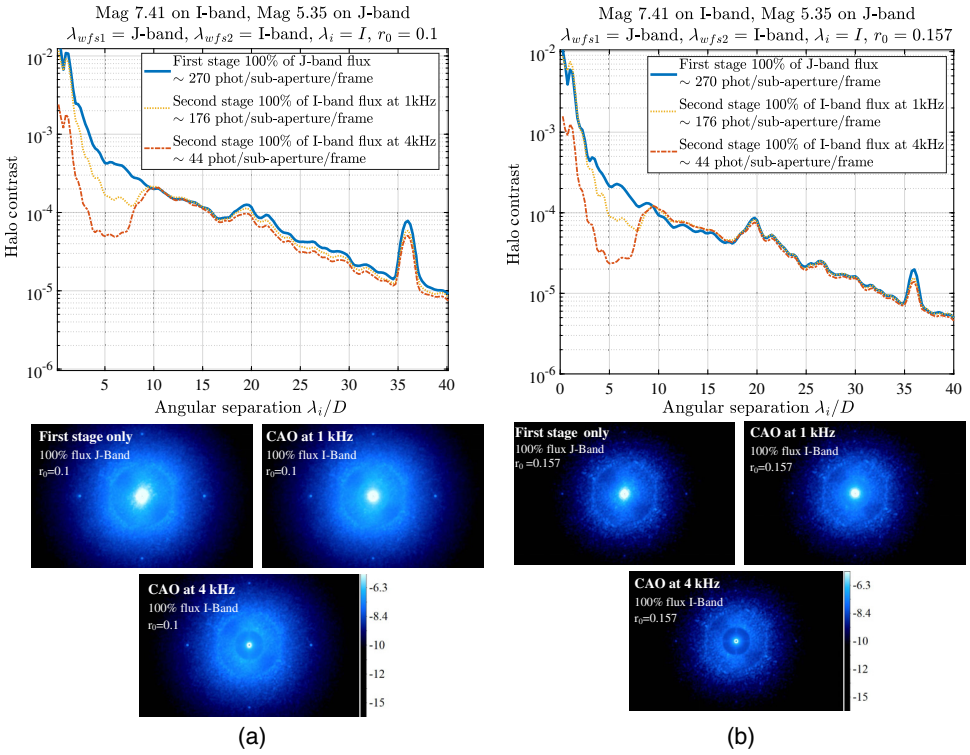

Fig. 13 Contrast performance and PSF for (a) $r_0 = 0.1$ and (b) $r_0 = 0.157$ and dichroic beamsplitting. All the J-band flux was sent to the first stage, and all the I-band flux was sent to the second stage. Scientific analysis is done in I-band.

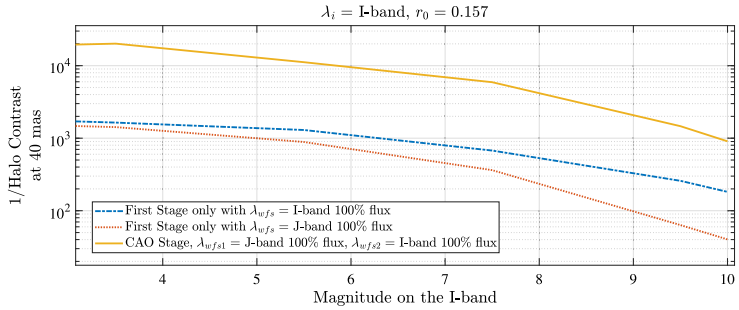

Fig. 14 PSF residual contrast as a function of magnitude at an angular separations of 40 mas.

temporal error for the system approaching the maximum stable gain and thereby operating at its maximum correction bandwidth set the contrast cap for very bright stars. In the faint end, the CAO system degrades less rapidly because its second stage is operated by the more sensitive pyramid WFS.

3.3 *Analysis of AO Residual Speckle Lifetime*

Another important parameter for HCI is the lifetime of speckles in the AO residual PSF. If we assume that the speckle noise would reduce with $1/\sqrt{t_{dc}}$, where t_{dc} is the speckle decorrelation time, a residual speckle halo with typical intensity contrast of about 10^{-5} would require 10^6 independent realizations to reach a level of 10^{-8} in the absence of other speckle correction techniques, such as angular, spectral, or polarimetric differential imaging. Depending on the speckle lifetime, accumulating that many realizations of the speckle pattern can be a very long process.

Long-lived quasistatic speckles are produced by instrument aberrations, which are left uncorrected by the AO system[65] and are one of the dominating factors affecting contrast especially at low angular separations.[11] These residual aberrations can occur in the instrument's science camera optical path, which is not seen by the AO WFS, or in the optical path to the AO WFS, which is not seen by the science camera. Therefore, they are called noncommon path aberrations (NCPA). NCPA change only slowly on timescales on which the instrument orientation and the gravity vector changes during an observation tracking a target in the sky. Also, temperature variations that produce thermal expansions in the instrument may introduce NCPA. Residuals from the atmospheric turbulence can induce a fast partial decorrelation of the PSF over a few seconds before transiting to a linear decorrelation regime at small angular separations.[66] A refined analysis further revealed another speckle decorrelation time scale of <2 ms, which can be attributed to the AO correction.[67]

Our simulations do not include NCPA, so we are solely looking at the temporal evolution of residual atmospheric turbulence speckle intensities. Assuming Taylor's frozen flow hypothesis, it was shown in Ref. 68 that an integrator-controlled AO system does not change the speckle lifetime compared with uncorrected turbulence but leads to an overall reduction in speckle intensity. This is explained by the idea that the correction always trails behind incoming turbulence leaving a residual with unchanged temporal characteristics. Moreover, the speckle lifetime is proportional to the ratio between telescope diameter (D) and wind-speed (v), more specifically $0.6D/v$. In the case of the VLT, with winds of 10 m/s, the atmospheric residual speckle lifetime is therefore of the order of half a second, whereas speckles are expected to decorrelate on timescales of several seconds in the ELT case. Such lifetimes would lead to unfeasible long exposure time requirements (more than 100 h for the 10^6 independent realizations motivated above) for reaching very high contrast. These considerations underline the high interest in reducing the lifetime of residual atmospheric speckles, even if the frozen flow assumption may be pessimistic in this context.

In Sec. 2.2, we showed that the low frequency part of the CAO's loop correction transfer function is very similar to the one of a double-integrator controller. The CAO system therefore presents a much more efficient reduction of the aberration energy at low temporal frequencies, and an effect on the speckle lifetime should be observable in the image plane. Therefore, we apply published analysis[69] on our simulated coronagraphic images and compare speckle lifetimes for single and double stage AO correction. We analyzed three annular regions at different angular separations from the PSF center: $A_1 = 2-5[\frac{\lambda}{D}]$, $A_2 = 5-8[\frac{\lambda}{D}]$, and $A_3 = 12-15[\frac{\lambda}{D}]$ as shown in Fig. 15. While A_1 and A_2 are inside the correction radius and controlled by both stages of the CAO, A_3 is only affected by the first stage and could therefore show a different speckle lifetime. We simulated a short 2.5 s observation with $r_0 = 0.157$ m and an elevated wind speed, 50% higher than the wind speed used for the performance simulations (see Table 1). For each of the three regions, we arranged the 2.5 s worth of imaging data in a matrix that contains the evolution over time for each pixel. We then subtracted the mean intensity of each pixel and calculated the temporal autocorrelation functions. Finally, the autocorrelation functions of all the pixels were averaged to derive the typical temporal correlation of the residual speckles in the three considered regions.

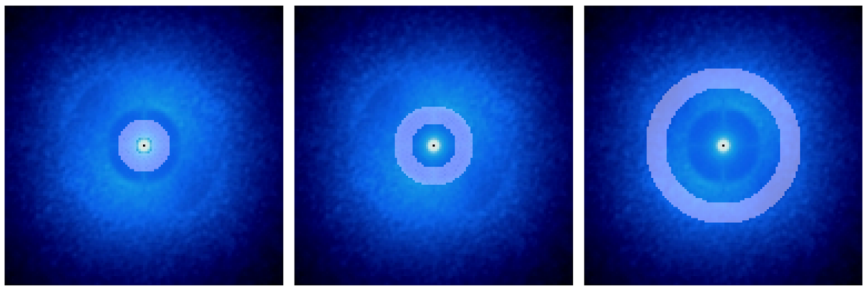

Fig. 15 Long exposure perfect coronagraph PSF with different regions A over imposed. (a) $A_1 = 2-5[\frac{\lambda}{D}]$, (b) $A_2 = 5-8[\frac{\lambda}{D}]$, and (c) $A_3 = 12-15[\frac{\lambda}{D}]$.

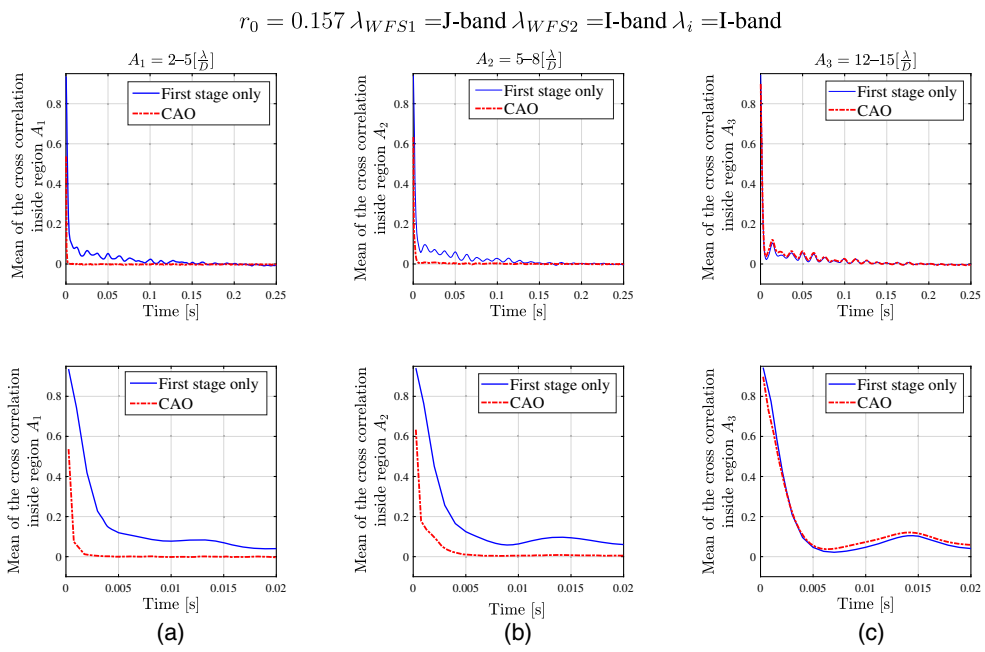

Fig. 16 Temporal decorrelations of all the pixels inside A for three different regions: (a) $A_1 = 2 - 5[\frac{\lambda}{D}]$, (b) $A_2 = 5 - 8[\frac{\lambda}{D}]$, and (c) $A_3 = 12 - 15[\frac{\lambda}{D}]$. The panels on the bottom zoom in on very short timescales.

The results are shown Fig. 16. In the regions A_1 and A_2 we clearly see the effect of the second stage. While the lifetime of residual speckles after the first stage is of the order of 0.15 s, it is reduced to just a few ms after the second stage. This reduction of a factor 30 to 50 is much larger than the fourfold increased correction speed offered by the second stage. We also see that the decorrelation time in region A_3 is not affected by the CAO. This is the expected behavior because A_3 is outside of the control region of the second stage. Compared with the relatively long lifetime of residual atmospheric speckle of a single stage AO, the fast decorrelation of residual speckles of the CAO will help to smoothen the residual PSF efficiently. The more than 100 h for 10^6 independent realizations would then shorten to just a few hours, which is consistent with typical HCI observing times.

4 *Summary and Discussion*

A two-stage CAO system with a faster second stage presents an efficient way to significantly improve the contrast performance of an existing extreme adaptive optics (XAO) system limited by temporal error, which is of paramount interest for the exoplanet science case. While a single stage XAO system running at high speed and equipped with a high order DM could probably provide better results than the proposed CAO system, it would require a more powerful RTC and a fast response and large stroke of the high-order DM. The proposed CAO system instead provides a cost and resource effective solution to improve the performance of an existing XAO system. Further benefits are that the second stage can easily be integrated and tested standalone and retrofitted into an existing instrument. The main complication introduced by this concept is that the first stage increases the relative content of high temporal frequency disturbance input to the second stage because of its controller overshoot and the intersampling signal (see Sec. 2.2). Possibilities to mitigate this effect include running the first stage at a reduced gain in noisy conditions or designing the second stage controller in a way that effectively copes with the intersampling signal. A straightforward solution would be to include a notch filter in the second stage loop. Also, a global design of an optimized second stage predictive controller would be of great interest. These developments deserve a complete study and are left for future work. We also showed that the low temporal frequency rejection of the CAO is partly the same than that

of an SCAO system controlled with a double-integrator and is much higher than that of an SCAO system controlled with a standard integrator.

Numerical simulations of a first stage SHS AO system running at 1 kHz (similar to the existing VLT-SPHERE or AOF) show that a fast second stage employing a sensitive WFS such as the unmodulated PWS would improve the correction performance for all GS magnitudes. A simple integrator control for both stages where the second stage runs at four times the framerate of the first one increases the contrast by about one order of magnitude, which would translate into a similar reduction of science exposure time required to reach a certain S/N. The integrator gains of both stages must be jointly optimized to reach optimum performance to cope with the first stage altering the input disturbance to the second stage. The two-stage CAO can provide at 2 λ/D an I-band contrast of the order 1:5000 for an 8-m telescope with a first stage AO correcting 800 modes at a framerate of 1 kHz. Such a performance would for example bring the detection of oxygen in the atmosphere of Proxima b (if it were present at an Earth-like abundance) within reach.

AO systems that already use the sensitive PWS and run at high framerates such as KPIC[70] or MagAO-X[71] are already able to reduce all relevant AO residual error terms (aliasing, temporal, and noise errors) to the minimum and therefore would not benefit from a CAO architecture in the same way as the system we have studied. In particular, the double-integrator behavior of the CAO for low frequencies can also be obtained by a single-stage AO.

Finally, a CAO with a four times faster second stage reduces the decorrelation or lifetime of atmospheric turbulence speckles by a factor 30 to 50 over the lifetime observed with the first stage only. While this obviously does not reduce photon noise, it helps to smooth the residual halo more rapidly and reduce its "granularity." This CAO therefore leads to a reduction of atmospheric speckle noise such that spatial low-pass filtering methods can be used to improve the final image contrast effectively.

Acknowledgments

This work has received funding from the European Unions Horizon 2020 research and innovation program, Grant Agreement No. 730890.

References

1. M. Mayor and D. Queloz, "A Jupiter-mass companion to a solar-type star," *Nature* **378**, 355–359 (1995).
2. E. Han et al., "Exoplanet orbit database. II. Updates to Exoplanets.org," *Publ. Astron. Soc. Pac.* **126**(943), 827 (2008).
3. C. Marois et al., "Direct imaging of multiple planets orbiting the star HR 8799," *Science* **322**, 1348 (2008).
4. C. Marois et al., "Images of a fourth planet orbiting HR 8799," *Nature* **468**, 1080–1083 (2010).
5. A.-M. Lagrange et al., "A giant planet imaged in the disk of the young star Beta Pictoris," *Science* **329**, 57 (2010).
6. J. Rameau et al., "Discovery of a probable 4-5 Jupiter-mass exoplanet to HD 95086 by direct imaging," *Astrophys. J. Lett.* **772**, L15 (2013).
7. V. Bailey et al., "HD 106906 b: a planetary-mass companion outside a massive debris disk," *Astrophys. J. Lett.* **780**, L4 (2014).
8. B. Macintosh et al., "Discovery and spectroscopy of the young Jovian planet 51 Eri b with the Gemini Planet Imager," *Science* **350**, 64–67 (2015).
9. G. Chauvin et al., "Discovery of a warm, dusty giant planet around HIP 65426," *Astron. Astrophys.* **605**, L9 (2017).
10. G. P. P. L. Otten et al., "Direct characterization of young giant exoplanets at high spectral resolution by coupling SPHERE and CRIRES+," *Astron. Astrophys.* **646**, A150 (2021).
11. O. Guyon, "Limits of adaptive optics for high-contrast imaging," *Astrophys. J.* **629**, 592–614 (2005).

12. J. Chilcote et al., "GPI 2.0: upgrading the Gemini Planet Imager," *Proc. SPIE* **11447**, 114471S (2020).
13. J. R. Males and O. Guyon, "Ground-based adaptive optics coronagraphic performance under closed-loop predictive control," *J. Astron. Telesc. Instrum. Syst.* **4**, 019001 (2018).
14. C. Z. Bond et al., "Adaptive optics with an infrared pyramid wavefront sensor at Keck," *J. Astron. Telesc. Instrum. Syst.* **6**(3), 039003 (2020).
15. J. Lozi et al., "SCExAO, an instrument with a dual purpose: perform cutting-edge science and develop new technologies," *Proc. SPIE* **10703**, 1070359 (2018).
16. A. Boccaletti et al., "SPHERE+: imaging young Jupiters down to the snowline," arXiv: Earth and Planetary Astrophysics (2020).
17. B. Chazelas et al., "RISTRETTO: a pathfinder instrument for exoplanet atmosphere characterization," *Proc. SPIE* **11448**, 1144875 (2020).
18. M. D. Perrin et al., "The structure of high Strehl ratio point-spread functions," *Astrophys. J.* **596**, 702–712 (2003).
19. J. L. Beuzit et al., "SPHERE: the Exoplanet imager for the Very Large Telescope," *Astron. Astrophys.* **631**, A155 (2019).
20. P. Y. Madec et al., "Adaptive optics facility: from an amazing present to a brilliant future," *Proc. SPIE* **10703**, 1070302 (2018).
21. C. Dessenne, P.-Y. Madec, and G. Rousset, "Modal prediction for closed-loop adaptive optics," *Opt. Lett.* **22**, 1535–1537 (1997).
22. D. T. Gavel and D. Wiberg, "Toward Strehl-optimizing adaptive optics controllers," *Proc. SPIE* **4839**, 890–901 (2003).
23. B. Le Roux et al., "Optimal control law for classical and multiconjugate adaptive optics," *J. Opt. Soc. Am. A* **21**, 1261 (2004).
24. L. A. Poyneer, B. A. Macintosh, and J.-P. Véran, "Fourier transform wavefront control with adaptive prediction of the atmosphere," *J. Opt. Soc. Am. A* **24**, 2645 (2007).
25. P. Piatrou and M. C. Roggemann, "Performance study of Kalman filter controller for multiconjugate adaptive optics," *Appl. Opt.* **46**(9), 1446–1455 (2007).
26. K. Hinnen, M. Verhaegen, and N. Doelman, "Exploiting the spatiotemporal correlation in adaptive optics using data-driven H2-optimal control," *J. Opt. Soc. Am. A* **24**(6), 1714–1725 (2007).
27. C. Petit et al., "Linear quadratic Gaussian control for adaptive optics and multiconjugate adaptive optics: experimental and numerical analysis," *J. Opt. Soc. Am. A* **26**, 1307–1325 (2009).
28. R. Fraanje et al., "Fast reconstruction and prediction of frozen flow turbulence based on structured Kalman filtering," *J. Opt. Soc. Am. A* **27**, A235–A245 (2010).
29. C. Kulcsár et al., "Minimum variance prediction and control for adaptive optics," *Automatica* **48**, 1939–1954 (2012).
30. C. M. Correia et al., "Spatio-angular minimum-variance tomographic controller for multi-object adaptive-optics systems," *Appl. Opt.* **54**, 5281 (2015).
31. O. Guyon and J. Males, "Adaptive optics predictive control with empirical orthogonal functions (EOFS)," arXiv: Instrumentation and Methods for Astrophysics (2017).
32. M. Glück, J. Pott, and O. Sawodny, "Model predictive control of multi-mirror adaptive optics systems," in *IEEE Conf. Control Technol. and Appl. (CCTA)*, pp. 909–914 (2018).
33. L. Prengère, C. Kulcsár, and H.-F. Raynaud, "Zonal-based high-performance control in adaptive optics systems with application to astronomy and satellite tracking," *J. Opt. Soc. Am. A* **37**(7), 1083–1099 (2020).
34. X. Liu et al., "Wavefront prediction using artificial neural networks for open-loop adaptive optics," *Mon. Not. R. Astron. Soc.* **496**, 456–464 (2020).
35. C. Dessenne, P.-Y. Madec, and G. Rousset, "Sky implementation of modal predictive control in adaptive optics," *Opt. Lett.* **24**(5), 339–341 (1999).
36. N. Doelman, R. Fraanje, and R. den Breeje, "Real-sky adaptive optics experiments on optimal control of tip-tilt modes," in *Second Int. Conf. Adapt. Opt. for Extremely Large Telesc.*, p. 51 (2011).
37. G. Sivo et al., "First on-sky SCAO validation of full LQG control with vibration mitigation on the CANARY pathfinder," *Opt. Express* **22**(19), 23565–23591 (2014).

38. O. Lardière et al., "Multi-object adaptive optics on-sky results with Raven," *Proc. SPIE* **9148**, 91481G (2014).
39. B. Sinquin et al., "On-sky results for adaptive optics control with data-driven models on low-order modes," *Mon. Not. R. Astron. Soc.* **498**(3), 3228–3240 (2020).
40. C. Petit et al., "SPHERE eXtreme AO control scheme: final performance assessment and on sky validation of the first auto-tuned LQG based operational system," *Proc. SPIE* **9148**, 91480O (2014).
41. L. A. Poyneer et al., "Performance of the Gemini Planet Imager's adaptive optics system," *Appl. Opt.* **55**(2), 323–340 (2016).
42. C. M. Correia et al., "Modeling astronomical adaptive optics performance with temporally filtered Wiener reconstruction of slope data," *J. Opt. Soc. Am. A* **34**, 1877 (2017).
43. R. Ragazzoni and J. Farinato, "Sensitivity of a pyramidic wave front sensor in closed loop adaptive optics," *Astron. Astrophys.* **350**, L23–L26 (1999).
44. R. Juvénal et al., "Linear controller error budget assessment for classical adaptive optics systems," *J. Opt. Soc. Am. A* **35**, 1465 (2018).
45. J. M. Conan, G. Rousset, and P. Y. Madec, "Wave-front temporal spectra in high-resolution imaging through turbulence," *J. Opt. Soc. Am. A* **12**, 1559–1570 (1995).
46. C. Vérinaud, "On the nature of the measurements provided by a pyramid wave-front sensor," *Opt. Commun.* **233**, 27–38 (2004).
47. T. Fusco et al., "Final performance and lesson-learned of SAXO, the VLT-SPHERE extreme AO: from early design to on-sky results," *Proc. SPIE* **9148**, 91481U (2014).
48. G. Anglada-Escudé et al., "A terrestrial planet candidate in a temperate orbit around Proxima Centauri," *Nature* **536**, 437–440 (2016).
49. I. Ribas et al., "A candidate super-Earth planet orbiting near the snow line of Barnard's star," *Nature* **563**, 365–368 (2018).
50. R. F. Díaz et al., "The SOPHIE search for northern extrasolar planets. XIV. A temperate ($T^{eq} \sim 300$ K) super-earth around the nearby star Gliese 411," *Astron. Astrophys.* **625**, A17 (2019).
51. M. Zechmeister et al., "The CARMENES search for exoplanets around M dwarfs. Two temperate Earth-mass planet candidates around Teegarden's Star," *Astron. Astrophys.* **627**, A49 (2019).
52. A. Quirrenbach et al., "CARMENES: high-resolution spectra and precise radial velocities in the red and infrared," *Proc. SPIE* **10702**, 107020W (2018).
53. F. Wildi et al., "NIRPS: an adaptive-optics assisted radial velocity spectrograph to chase exoplanets around M-stars," *Proc. SPIE* **10400**, 1040018 (2017).
54. R. Conan and C. Correia, "Object-oriented Matlab adaptive optics toolbox," *Proc. SPIE* **9148**, 91486C (2014).
55. E. Gendron and P. Lena, "Astronomical adaptive optics. I. Modal control optimization," *Astron. Astrophys.* **291**, 337–347 (1994).
56. V. Korkiakoski, C. Vérinaud, and M. Le Louarn, "Applying sensitivity compensation for pyramid wavefront sensor in different conditions," *Proc. SPIE* **7015**, 701554 (2008).
57. V. Deo et al., "A modal approach to optical gain compensation for the pyramid wavefront sensor," *Proc. SPIE* **10703**, 1070320 (2018).
58. C. Cavarroc et al., "Fundamental limitations on Earth-like planet detection with extremely large telescopes," *Astron. Astrophys.* **447**, 397–403 (2006).
59. F. Cantalloube et al., "Wind-driven halo in high-contrast images - I. Analysis of the focal-plane images of SPHERE," *Astron. Astrophys.* **638**, A98 (2020).
60. C. Lovis et al., "Atmospheric characterization of Proxima b by coupling the SPHERE high-contrast imager to the ESPRESSO spectrograph," *Astron. Astrophys.* **599**, A16 (2017).
61. C. Vérinaud et al., "Adaptive optics for high-contrast imaging: pyramid sensor versus spatially filtered Shack–Hartmann sensor," *Mon. Not. R. Astron. Soc.* **357**, L26–L30 (2005).
62. F. J. Rigaut, J.-P. Veran, and O. Lai, "Analytical model for Shack–Hartmann-based adaptive optics systems," *Proc. SPIE* **3353**, 1038–1048 (1998).
63. D. L. Fried, "Time-delay-induced mean-square error in adaptive optics," *J. Opt. Soc. Am. A* **7**, 1224–1225 (1990).

64. J. Hardy, *Adaptive Optics for Astronomical Telescopes*, Oxford Series in Optical and Imaging Sciences, Oxford University Press (1998).
65. C. Marois et al., "Effects of quasi-static aberrations in faint companion searches," *EAS Publ. Ser.* **8**, 233–243 (2003).
66. J. Milli et al., "Adaptive optics in high-contrast imaging," in *Astronomy at High Angular Resolution: A Compendium of Techniques in the Visible and Near-Infrared*, pp. 17–41, Springer International Publishing, Cham (2016).
67. S. B. Goebel et al., "Measurements of speckle lifetimes in near-infrared extreme adaptive optics images for optimizing focal plane wavefront control," *Publ. Astron Soc. Pac.* **130**, 104502 (2018).
68. B. Macintosh et al., "Speckle lifetimes in high-contrast adaptive optics," *Proc. SPIE* **5903**, 59030J (2005).
69. J. Milli et al., "Speckle lifetime in XAO coronagraphic images: temporal evolution of SPHERE coronagraphic images," *Proc. SPIE* **9909**, 99094Z (2016).
70. D. Mawet et al., "Keck planet imager and characterizer: status update," *Proc. SPIE* **10703**, 1070306 (2018).
71. J. R. Males et al., "MagAO-X first light," *Proc. SPIE* **11448**, 114484L (2020).

Nelly Cerpa-Urra is a PhD student in the Institut d'Optique Graduate School (Palaiseau, France) and was part of the Adaptive Optics Systems Group at the European Southern Observatory, Garching, Germany. She graduated as an electrical engineer from the Universidad de Los Andes, Santiago, Chile, in 2015. Her research interests include contrast optimization using optimized control schemes for extreme adaptive optics systems (XAO) as also evaluation, definition, and simulation of double-stages adaptive optic systems.

Markus Kasper has extensive experience in astronomical instrumentation, adaptive optics, and high-contrast imaging. He was involved in many of ESO AO projects such as MACAO and NACO LGS and was the ESO project lead for VLT SPHERE. He was the principal investigator for the ELT/EPICS phase-A study (2008 to 2010) and for NEAR, the mid-IR imaging experiment to search for habitable planets in the Alpha Centauri. He is currently carrying out R&D; for the ELT-PCS planet imager.

Caroline Kulcsár is a professor at the Institut d'Optique Graduate School (IOGS) and is leading the adaptive optics team at the Laboratoire Charles Fabry (IOGS-CNRS-Université Paris-Saclay). She received her PhD in control theory from the Université Paris 11-Orsay, in 1995. Her research activities include codesign of imaging systems and control and identification of stochastic dynamical systems, with applications to adaptive optics systems. She is the cochair of the OPTICA (ex-OSA) Adaptive Optics topical meeting.

Henri-François Raynaud is a member of the Adaptive Optics team at Laboratoire Charles Fabry (IOGS-CNRS-University Paris-Saclay) and associate professor at Université Paris 13. He received his PhD in applied mathematics and control theory at the Université Paris 11 Orsay in 1990. His research interests include adaptive control, stochastic modeling, linear systems theory, and identification for control. He has been involved since the early 2000s in the design of high-performance controllers for adaptive optics system.

Cedric Taïssir Heritier is an engineering and technology research fellow in the Adaptive Optics Department at the European Southern Observatory, Garching, Germany. He received his PhD in instrumentation for astrophysics in 2019 from Aix-Marseille University (LAM-ONERA-ESO-INAF). His research interests include the calibration of complex adaptive optics systems, in particular in the context of large adaptive telescopes, system parameters identification, and wave-front sensing with pyramid wave-front sensors.

3.3 Numerical simulation environment

The numerical simulations of the CAO system were done using the OOMAO toolbox (Conan and Correia, 2014). OOMAO is made up from a series of classes to perform numerical modeling of an AO system using MATLAB. Each class contains the necessary parameters and functions to assemble MATLAB objects that enable to simulate a complete an AO system. Wavefront is propagated through the system using overloaded MATLAB operators (in specific $.*$ or *mtimes*). Overload operators are used to change the behavior of an specific operation.

3.3.1 Simulation components

This section will describe each class used for the numerical simulation and its parameters. Firstly we create a **source** object. This class acts as a link between classes, and it carries the wavefront amplitude and phase between the different objects of the system. The **source** class represents a celestial object and can create an on-axis source with infinite height. Then we only need to specify the wavelength and the magnitude. In the case of the CAO system simulation, we use two different source objects to not only separate the amount of flux entering to each stage, but also to specify on which WFS wavelength each stage is working on.

The **atmosphere** class will create an atmosphere object that the source will propagate through. We can include each layer's turbulence profile, including wind speed, wind direction, and Fried parameter. For a CAO system simulation, a unique atmosphere object is needed

The **telescope** class will create a telescope object. For this, we have to specify the telescope diameter, the obstruction ratio, and the field of view. The telescope object also defines the number of pixels to sample the pupil. In the context of this simulation, this is what we call the "resolution". It is defined by the number of pixels per subaperture by the number of lenslets of the WFS.

Because the CAO system uses two WFSs, we must create two WFS objects. Firstly, the **ShackHartmann** class makes a SHWFS defined by the number of lenslets and the detector resolution. We can also include other properties like the minimum light intensity ratio between a partially and a fully illuminated lenslet. Then, we initialize the WFS by computing the valid lenslets, which are the lenslets receiving sufficient light according to our minimum ratio (see Fig. 3.1). In our simulations, a diffractive model is used for the SHWFS.

The **Pyramid** class creates a PWFS object. OOMAO uses a diffractive model to simulate the PWFS. Similar to the **ShackHartmann** class, The PWFS objects define a phase mask object and a detector object. In the case of the CAO system simulations, we want to use a four-face pyramid as presented in section 2.5; hence

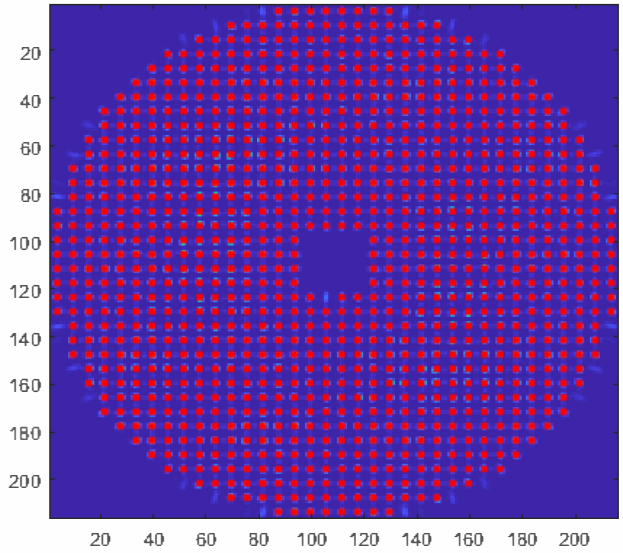

Figure 3.1: Image of the valid lenslets (red dots) calculated for a SHWFS object with a 36×36 lenslet array and a 216×216 resolution camera using OOMAO. In this case, the minimum ratio of light intensity between a partially and a fully illuminated lenslet is 50%.

we will produce four pupils on the detector. Among the parameters needed to generate a PWFS object in OOMAO, we can find the resolution, the obstruction ratio, the modulation, and the calibration modulation. In the calibration, the mask corresponding to the valid subapertures is obtained by considering the illumination of the pixels. For this, we applied a large modulation (in our case, we used $30\lambda/D$) to get a uniform illumination on each pupil. Then OOMAO uses the sum of the four quadrants to set a threshold and calculate the valid detector mask for calculating the slopes as seen on figure 3.2.

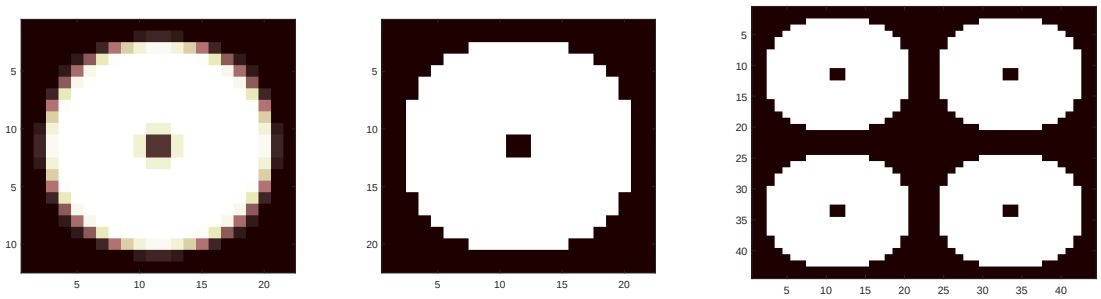

(a) (b)

Figure 3.2: On the left, sum of the four quadrants and the valid subapertures. On the right, the detector mask with the four pupils used for the slopes computation.

The influence function as we mentioned in Section 2.6 is commonly taken as a Gaussian function, and the class **GaussianInfluenceFunction** creates an influence function object with such characteristics. The influence function is created with two arguments: the actuator coordinates and the mechanical coupling. An example of the Gaussian influence function used for both DM's of the CAO simulations is given in figure 3.3.

The DM object is created thanks to the **DeformableMirror** class, with a given number of actuators and the previously defined influence function sampled at the same resolution as the telescope.

Once the WFSs and the DM are generated, we can compute the interaction matrices. The process is done with the **InteractionMatrix** function by replicating the models into the DM and saving the corresponding WFS slopes vectors in a matrix. For the CAO simulations, we use a K-L basis.

3.3.2 Simulation structure

For the CAO numerical simulations, we need to be able to simulate two closed-loop systems at the same time. In OOMAO to generate a phase screen, we need

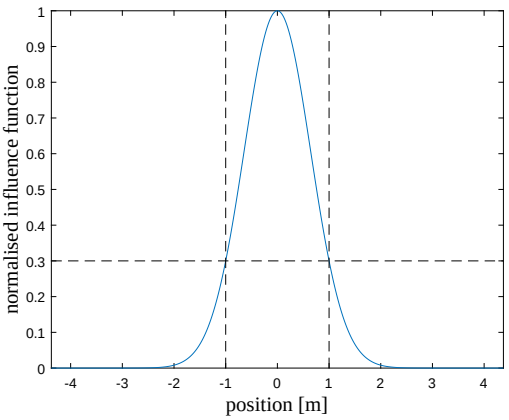

Figure 3.3: Gaussian influence function with a mechanical coupling of 30%.

to bound the atmosphere object to the telescope object. Only that way, the phase screens are created with the telescope object resolution. Because of this, the resolution of both WFSs needs to be the same, to be able to run the loop with only one telescope and atmosphere object. We achieve this by adjusting the number of subapertures or the number of pixels per subaperture on each WFS. In the case of the CAO numeral simulations, we use a resolution of 216×216 pixels to produce the phases. For the first stage SHWFS, we use 36×36 subapertures and 6 pixels per subapertures, and for the second stage PWFS, we use 18×18 lenslets and 12 pixels per subaperture.

Because we are using two different sampling frequencies for each stage, in OOMAO we generate the input phase at the fastest frequency (in our case, 4 kHz). The average of four consecutive turbulent phase screens enters to the first stage (1 kHz) at every fourth step, and the first stage DM is updated. Then, the residual phase generated by the first stage is sent as an input to the second stage at each step (See figure 3.4). This configuration allows us to take into account changes in the turbulent phase at the fast rate for the second stage and run both loops simultaneously.

3.4 Conclusions

In this chapter, we introduced the CAO system and how it could be simulated using OMAOO. We emphasize how to deal with the difference in the running frequency of both loops and how that can affect the system's final performance. Finally, we presented the simulation tool we used for the numerical simulations and how each element of the AO system is represented.

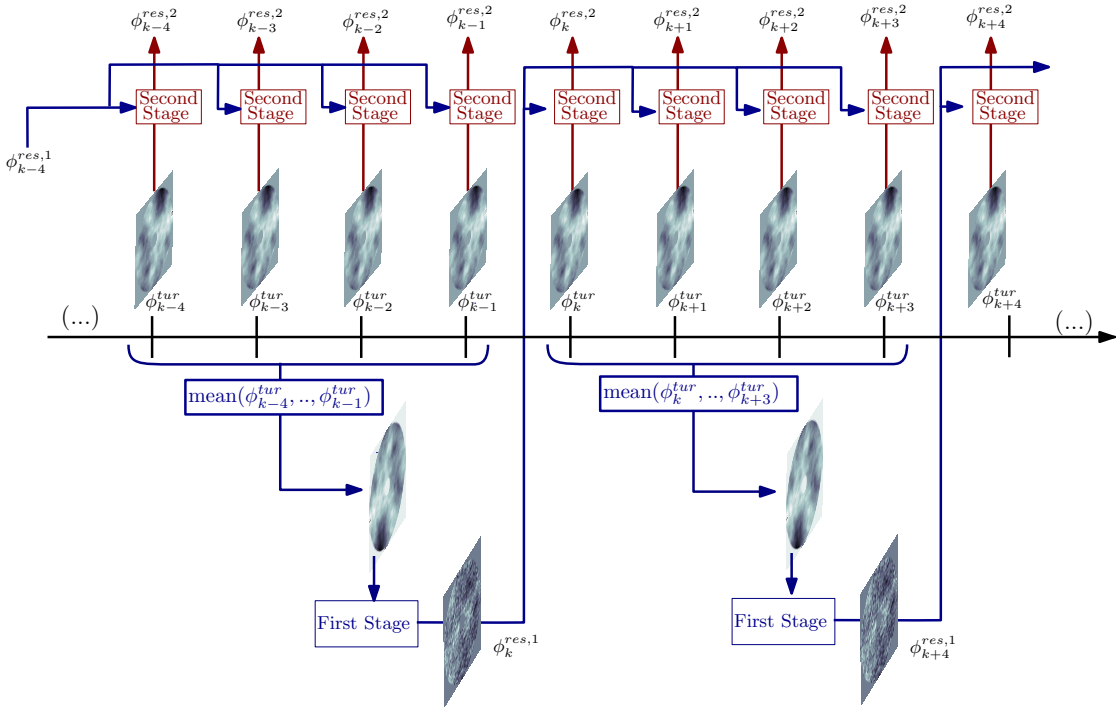

Figure 3.4: Configuration for the numerical simulations using OOMAO, where we generate the input phases at the fast rate and for the first stage we input the average of four consecutive turbulent phases. Then the residual phase of the first stage is sent four times as an input to the second stage.

We studied the CAO controller properties, and we analyze in particular how part of the disturbance is transferred from low to high temporal frequencies with a nefarious effect of the 2nd stage integrator overshoot. Possibilities to mitigate this effect are analyzed in the next chapter.

By running a numerical simulation, we demonstrated how a CAO system can be an efficient way to improve the contrast performance of an existing XAO system and how an un-modulated PWFS can improve performance. A simple integrator control for both stages, where the second stage runs at four times the framerate of the first one, increases the contrast by about one order of magnitude and reduces the decorrelation or lifetime of atmospheric turbulence speckles by a factor of 30 to 50 over the lifetime observed with the first stage only.

Although very good performance results were obtained in the paper, it is worth wondering whether the impact of the non-stationary and high-frequency signal coming from the 1st stage could be better handled in order to limit its nefarious effect in the 2nd stage. Also, we could investigate what performance improvement

could be brought by an LQG regulator instead of an integrator in the 2^{nd} stage. These question are the purpose of Chapter 4.

Chapter 4

Disentangled CAO with integrator and LQG controllers

4.1 Introduction

In the previous chapter, we have described and analyzed the CAO system with two stages. As a result, we could demonstrate that a 2-stage CAO system can improve wavefront correction and contrast for the XAO case even using simple integrators for both stages. Because of the different sampling rates of the two stages, the residual entering the 2^{nd} stage exhibits oscillations resulting from the upsampled 1^{st} stage correction effort. As this upsampled signal is non stationary, it cannot be efficiently compensated by any linear time-invariant controller. A refined control strategy for the 2-stage CAO is however possible if the 2^{nd} stage is informed about the 1^{st} stage control actions in order to « disentangle » the CAO (Raynaud, Kulcsár, Cerpa Urra, et al., 2022). This disentangled CAO system together with a mechanism that allows to close the 2^{nd} stage's loop without bumps in the trajectory are presented in the first part of this chapter in Sections 4.2 and 4.3.

In the second part of this Chapter, we propose to use an LQG regulator for our disentangled CAO control. First, we present in Section 4.4 the modeling of the incoming turbulence that is used to build the LQG controller. We also show how to implement this modal predictive control in the CAO numerical simulations. Finally, we present in Section 4.5 the results of the numerical simulations using disentangled CAO, with the 2^{nd} stage featuring an integrator or the LQG regulator. We analyze improvements in terms of contrast and speckle lifetime, which are critical for the exoplanet case.

4.2 Disentangled CAO control

In the 2-stage CAO system we have evaluated in Chapter 3, the 1st stage's sampling frequency is $F_1 = 1$ kHz and the residual phase enters a faster 2nd stage running at sampling frequency $F_2 = 4$ kHz. The faster 2nd stage is therefore subject to the control actions of the 1st stage DM in the form of "jumps" in the residual wavefront and will then have to correct for them. As already mentioned, these see-saw high-frequency oscillations are not properly compensated by the 2nd stage controller using a time-invariant controller like the one presented in (Cerpa-Urra et al., 2022). However, it is possible to anticipate the impact of the 1st stage commands on the inputs and outputs generated by the 2nd stage controller. This enables to disentangle the rejection transfer functions of the 1st and 2nd stage controllers. As a result, the CAO system will effectively behave as a woofer-tweeter system, with the total control effort corresponding to the 2nd stage rejection transfer function efficiently split between the two DMs (Raynaud, Kulcsár, Cerpa Urra, et al., 2022).

To describe the disentangling procedure, let us assume that we have a 2-stage controller, where $y_{2,k}$ is the 2nd stage measurement vector at time k. This measurement is a function of the residual phase ϕ^{res}_{k-1}, the 2nd stage WFS matrix D_2 and a Gaussian measurement noise $w_{2,k}$:

$$y_{2,k} = \mathbf{D}_2\phi^{res}_{k-1} + w_k = \mathbf{D}_2(\phi_{k-1} - \phi^{corr}_{k-1}) + w_{2,k}\,, \tag{4.1}$$

were the total correction phase ϕ^{corr} is the sum of the corrections generated by the two stages. Assuming a computational delay of one frame in each stage, at the faster 2nd stage rate this total correction is given by

$$\phi^{corr}_k = \phi^{corr,1}_k + \phi^{corr,2}_k = \mathbf{N}_2 u_{2,k-1} + \mathbf{N}_1 u_{1,k-4}\,, \tag{4.2}$$

where $\mathbf{N}_1$ and $\mathbf{N}_2$ are the DMs' influence functions of the two stages.

Let us now assume that the 2nd stage controller is implemented in standard state-space form, namely:

$$\begin{cases} x_{k+1} &= \mathbf{A}_u x_k + \mathbf{B}_u y_{2,k} \\ u_{2,k} &= \mathbf{C}_u x_{k+1} \end{cases}. \tag{4.3}$$

Obviously, if no 1st stage correction were applied, the total correction would be instead

$$\phi^{corr}_k = \phi^{corr,2}_k = \mathbf{N}_2 u_{2,k-1} = \mathbf{N}_2\mathbf{C}_u x_k\,. \tag{4.4}$$

Conversely, to make the CAO control equivalent to this 2nd-stage-only setup when the 1st stage is running, it suffices to ensure that

$$\mathbf{N}_2 u_{2,k-1} + \mathbf{N}_1 u_{1,k-4} = \mathbf{N}_2\mathbf{C}_u x_k. \tag{4.5}$$

Solving this equation in u_2, we get:

$$u_{2,k} = \mathbf{C}_u x_{k+1} - \mathbf{N}_2^{\dagger}\mathbf{N}_1 u_{1,k-3}\,. \tag{4.6}$$

As we can see in Figure 4.1,

This procedure effectively splits the control effort $\mathbf{C}_u x$ computed by the 2nd stage controller between the 1st and the 2nd stage DMs, thus disentangling the rejection transfer functions of the two stages. More precisely, all the turbulence modes lying in the correction space of the 2nd stage DM will be attenuated by the disentangled CAO system according to the 2nd stage stand-alone rejection transfer function. As for the turbulent modes which can be corrected only by the 1st stage (assuming that the correction space of the 1st stage is larger than that of the 2nd stage), they will be compensated according to the 1st stage rejection transfer function.

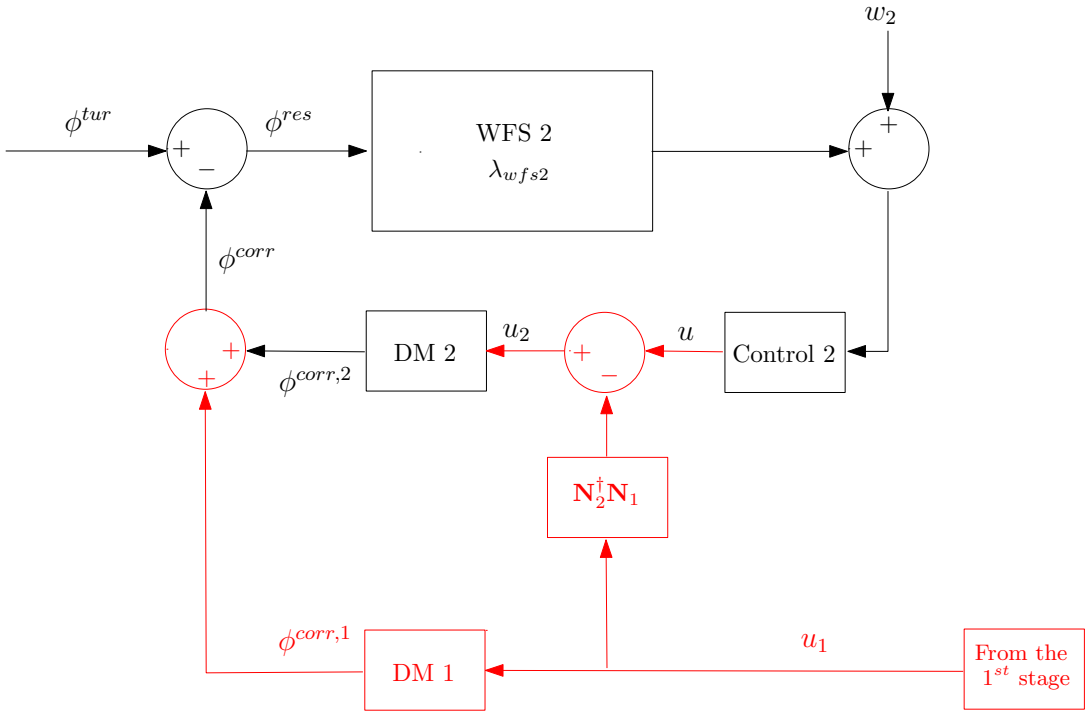

Figure 4.1: Block diagram of a disentangled AO loop where a stand-alone system equivalent to the 2-stages is used to compensate for the total incoming turbulence.

In principle, implementing the disentangled CAO control is a simple and straightforward procedure, but in practice, it maybe not be so easy. As we can see in equation 4.6, the effects of the 1st stage command must be mapped into the 2nd stage DM's space. Both influence matrices thus need to be adequately calibrated.

4.3 Bumpless switching

The standard operating procedure for a CAO system would be to engage the 1st stage loop and to wait for the residual to decrease before closing the 2nd stage. In this way, the 2nd stage residual, measurement and command signals should hopefully be of smaller amplitude. This is especially important when the 2nd stage uses a pyramid WFS with a narrow linear range.

However, switching on a disentangled 2nd stage controller with its internal state initialized at zero is guaranteed to generate a violent transient "bump" on the total CAO correction. To understand why, assume that the disentangled 2nd stage controller is switched on at $k = k_S$, with initial state $x_{k_S} = 0$. The correction phases immediately before and after would then be respectively equal to

$$\phi^{corr}_{k_S} = \mathbf{N}_1 u_{1,k_S-4}\,, \tag{4.7}$$

$$\phi^{corr}_{k_S+1} = \mathbf{N}_2\mathbf{C}_u x_{k_S+1} = \mathbf{N}_2\mathbf{C}_u\mathbf{B}_u y_{k_S}\,. \tag{4.8}$$

When $\phi^{corr}_{k_S} \simeq \phi_{k_S}$ and $y_{k_S} \simeq 0$, this will result in a control bump. In our simulations, this bump was violent enough to throw the pyramid WFS way outside its effective linear range, making the whole CAO loop diverge.

In order to prevent this, the 2nd stage controller state x_{k_S} needs to be initialized to a value which ensures a reasonable continuity between the pre- and post-switching trajectories of ϕ^{corr}. To achieve this, we used the so-called adapter procedure proposed in (Raynaud, Kulcsár, Juvénal, et al., 2016). The basic idea is to compare the last portion of the pre-switching control trajectory with the virtual trajectory which the 2nd stage controller would have generated if it had been active prior to switching, and to select the controller state so as to minimize the mismatch between the two.

In the case of the disentangled 2nd stage AO controller, for $k \leq k_S$ we have $\phi^{corr}_k = \mathbf{N}_1 u_{1,k-4}$, which translates into the reference trajectory $u^*_{2,k} = \mathbf{N}_2^\dagger \mathbf{N}_1 u_{1,k-3}$ for all $k < k_S$. The next step in the adapter approach is to select a "stitching horizon" k_H and to minimize the mismatch between the sequence $u^*_{2,k_S-k_H}, \ldots, u^*_{2,k_S-1}$ and the corresponding virtual trajectory $u^v_{2,k_S-k_H}, \ldots, u^v_{2,k_S-1}$ that the 2nd stage controller would have generated if it had been activated at $k = k_S - k_H$ from an arbitrary initial condition $x_{k_S-k_H} = z$. To obtain the bump-avoiding value of x_{k_S}, one then propagates (also virtually) the optimal value of z forward in time through the controller's dynamics.

In the case of an integrator, where $x_k = u_{2,k-1}$ and $\mathbf{A}_u = \mathbf{C}_u = I$, it is immediately checked that for $k_H = 1$, one achieves $u^v_{2,k_S-1} = u^*_{2,k_S-1}$ by taking $x_{k_S-1} = u^*_{2,k_S-2}$, which then propagates into $x_{k_S} = u^*_{2,k_S-1}$.

For an LQG controller, we instead select an optimal value of $z = x_{k_S - k_H}$ by minimizing the quadratic stitching criterion

$$J = \| u^*_{2,k_S-1} - u^v_{2,k_S-1} \|^2 + \varepsilon^2 I \,, \tag{4.9}$$

with $\varepsilon \simeq 0$. The optimal value of the controller state is then given as a linear combination of u^*_{2,k_S-1} and y_{k_S-1}:

$$x_{k_S} = \mathbf{M}_u u^*_{2,k_S-1} + \mathbf{M}_y y_{k_S-1} \,, \tag{4.10}$$

where

$$\mathbf{M}_u = \mathbf{A}_u \Lambda^{-1} \mathbf{A}_u^{\mathrm{T}} \mathbf{C}_u^{\mathrm{T}} \,, \tag{4.11}$$

$$\mathbf{M}_y = (I - \mathbf{M}_u \mathbf{C}_u) \mathbf{B}_u \,, \tag{4.12}$$

$$\tag{4.13}$$

with

$$\Lambda = \mathbf{A}_u^{\mathrm{T}} \mathbf{C}_u^{\mathrm{T}} \mathbf{C}_u \mathbf{A}_u + \varepsilon^2 I \,. \tag{4.14}$$

4.4 Disentangled LQG CAO control

As mentioned in Chapter 1, a way of reducing temporal error, besides running fast, is to resort to predictive control. AO Predictive controllers have been proposed in the literature in many different forms (Correia, Jackson, et al., 2015; Dessenne, Madec, and Rousset, 1997; Fraanje et al., 2010; Gavel and Wiberg, 2003; Glück, Pott, and Sawodny, 2018; Guyon and Males, 2017; Hinnen, Verhaegen, and Doelman, 2007; Kulcsár, Raynaud, Petit, and Conan, 2012; Le Roux et al., 2004; Liu et al., 2020; Petit, Conan, Kulcsár, and Raynaud, 2009; Piatrou and Roggemann, 2007a; Poyneer, Macintosh, and Véran, 2007; Prengère, Kulcsár, and Raynaud, 2020), and some on-sky tests have been performed (Dessenne, Madec, and Rousset, 1999; Doelman, Fraanje, and Breeje, 2011; Lardière et al., 2014; Sinquin et al., 2020; Sivo, Kulcsár, Conan, Raynaud, Gendron, et al., 2014; Tesch et al., 2015). A natural next step to improve the performance of the CAO is thus to implement a disentangled 2$^{\mathrm{nd}}$ stage LQG controller. In this section, we will present the modeling done for the turbulent phase dynamics and how we use this model to implement an LQG predictive control on the 2$^{\mathrm{nd}}$ stage using a K-L mode basis.

LQG control is based on a state-space representation of the system, for which we must identify the turbulent phase dynamics. We choose to expand the wavefront on a K-L basis. Because K-L modes are statistically independent, this translates into a diagonal spatial turbulence covariance matrix $\mathbf{\Sigma}_\phi$. If we also assume that each mode is temporally independent of the other, then we can write a global model in a state-space form as:

$$\begin{cases} X_{k+1} &= \mathbf{A}X_k + \Gamma v_k \,, \\ \phi_k &= \mathbf{C}_\phi X_k \,, \\ y_k &= \mathbf{C}X_k + w_k - \mathbf{M}_{int}u_{k-2} \,, \end{cases} \tag{4.15}$$

where v and w are mutually independent vector-valued zero-mean Gaussian white noises, with covariance matrices Σ_v and Σ_w.

The matrix $\mathbf{C}_\phi$ extracts the corresponding turbulent phase for each mode from the state vector X_k. The matrix $\mathbf{A}$ will be block-diagonal, with each block defining the temporal dynamics of one particular mode:

$$\mathbf{A} = \begin{bmatrix} \mathbf{A}^{(1)} & 0 & \cdots & 0 \\ 0 & \ddots & & \vdots \\ \vdots & & \mathbf{A}^{(i)} & 0 \\ 0 & \cdots & 0 & \mathbf{A}^{(n_{mod})} \end{bmatrix}, \tag{4.16}$$

were $\dim(\mathbf{A}^{(i)}) = n_{mod}$ is the order chosen for all of the identified models. The variance of the turbulence generated by the model is then given by $\Sigma_\phi = \mathbf{C}\Sigma_x\mathbf{C}^{\mathrm{T}}$, where Σ_x is the solution of the Lyapunov equation

$$\Sigma_x = \mathbf{A}\Sigma_x\mathbf{A}^{\mathrm{T}} + \Gamma\Sigma_v\Gamma^{\mathrm{T}} \,. \tag{4.17}$$

Once $\mathbf{A}$, $\mathbf{\Gamma}$ and $\mathbf{C}$ have been chosen, the value of Σ_v can be adjusted so that the corresponding value of Σ_ϕ matches the spatial covariance matrix of the K-L modes.

Finally, the measurement model matrix $\mathbf{C}$ is given by $\mathbf{C} = \mathbf{D}\mathbf{C}_\phi$, where $\mathbf{D}$ is the WFS matrix in the K-L basis. This model enables to compute and implement the associated Kalman filter and LQG controller, following the procedure described in Chapter 2.

To identify the models for the different K-L modes, we use here the standard approach presented in the case of AO in (Kulcsár, Massioni, et al., 2012) and (Juvenal et al., 2015), which combines the subspace identification algorithm N4SID with the Prediction Error Minimization (PEM) method. N4SID identifies the turbulence model for each K-L mode from previously recorded modal trajectories, directly in state-space form (Van Overschee and De Moor, 1996; Verhaegen and Verdult, 2007). The dimension of the state component $X^i(k)$ for the i-th K-L mode is taken equal to n_{ord}. Modal models estimated by N4SID are then refined using the PEM method, described in (Ljung, 1999), which works by minimizing the variance of the one-step ahead prediction error along the trajectory. In our case, we ran experiments with models orders $n_{ord} = 4$ and $n_{ord} = 6$. This same

method can be operated using measured on-sky data, but in this study, the models were identified from simulated turbulence trajectories.

For our simulations, we use the **n4sid.m** and **pem.m** functions already implemented in MATLAB, where **pem.m** is by default initialized using **n4sid.m**.

To verify how good is the prediction made by the identified model, we can calculate the 1-step-ahead prediction error (residuals) given by the model. These residuals are thus differences between the 1-step-ahead prediction calculated using the model and the data itself. Thus, the residuals represent the part of the data that could not be predicted by the model. Therefore, if the model perfectly predicts the data, the residuals should correspond to a white noise. To appreciate the efficacy of the prediction, we evaluate the autocorrelation of the residuals produced by the identified model for KL-mode 3, 10 and 50. This is to be compared with the case where the 1-step-ahead prediction is obtained by simply using the current value (that is without using the identified model). We can see in Figure 4.2 (a)-(c) that the autocorrelations of the residuals are close to a white noise, while the autocorrelation without using the model (d) is flat around 0. This means that we have a good model, with residuals very well decorrelated.

4.5 Performance simulations with disentangled CAO control

We used numerical simulations to study the functioning and performance of the disentangling procedure presented before. As in the previous chapters, we made the same assumptions as in (Cerpa-Urra et al., 2022), where we chose the SHWFS to drive the 1st stage and an unmodulated PWFS for the 2nd stage.

The 1st stage's SHWFS is chosen so as to control about 800 Karhunen-Loève modes sampled by 36x36 subapertures at 1 kHz. The 2nd stage's PWS has a twice coarser one-dimensional sampling (18x18) and controls 200 modes but runs four times faster (4 kHz) as in the previous simulations. More details on the observational and instruments parameters can be found in Table 1 from Chapter 3.2.

Contrary to what was done in (Cerpa-Urra et al., 2022), we did not evaluate the disentangled control using a gray beam-splitting, but only the dichroic beam-splitting option. As we showed in previous chapters, the dichroic beam-splitting with the 1st stage operating at a longer wavelength in the J-band and the 2nd stage operating in I-band presented better results in terms of contrast and SR.

Another benefit of using the disentangling procedure is that, because the 2nd stage now behaves like a stand-alone 2nd stage, it decouples the gain optimization between the stages. This means that when using a standard integrator, it is not

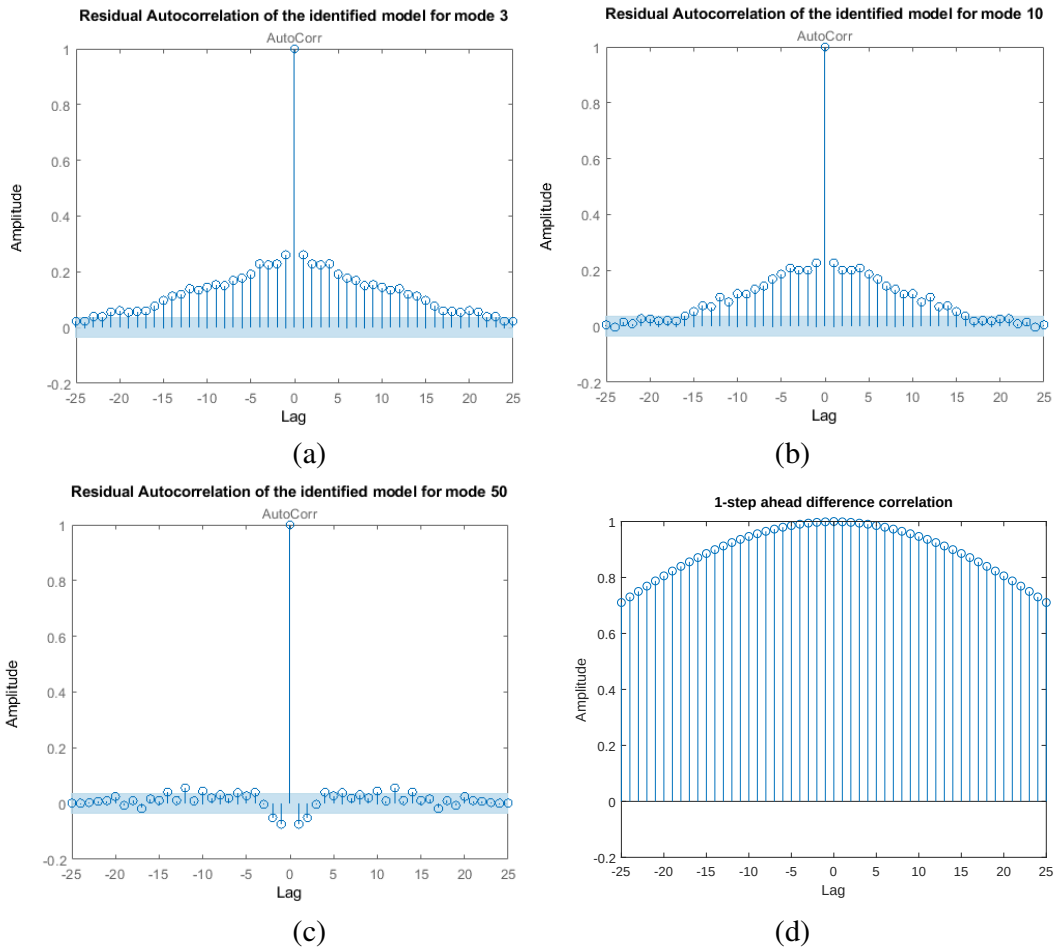

Figure 4.2: Autocorrelation of the residuals for three different models of three different modes (a) for KL-mode 3, (b) for KL-mode number 10 and (c) for KL-mode number 50, and (d) autocorrelation of the 1-step-ahead residuals without any model.

necessary to run a joint optimization of the closed loop gain values of both stages as in Chapter 3.2. As shown in Figure 4.3, it is only necessary to optimize the gain values for each stage independently.

Besides using a standard integrator on both stages, we also repeat the performance evaluations using the LQG regulator presented in Chapter 4.4 for the 2$^{\text{nd}}$ stage, while retaining integrator control for the 1$^{\text{st}}$ stage.

4.5.1 Residual WFE and contrast performance

Having determined the optimum integrator gains for each stage, we can now compare the performance of the CAO system with and without a disentangled control in the 2$^{\text{nd}}$ stage. As mentioned in previous chapters, the simulated observations represent the flux case of Proxima Centauri with I = 7.4, and imaging is done in I-band.

Figure 4.4 show the residual variance for each of the 200 2$^{\text{nd}}$ stage K-L mode afters 10,000 iterations of the 1$^{\text{st}}$ stage (i.e., after 10 seconds of closed-loop operation). We can see that a significant improvement can be achieved using the 2$^{\text{nd}}$ stage integrator with disentangled control over nearly all the modes. We can see that we get a good total correction, and what we achieve with this compensation scheme is that we have offloaded part of the correction effort to the 1$^{\text{st}}$ stage.

In Figure 4.4, if we compare the residual variance of the 1$^{\text{st}}$ stage (blue dashed line) with the residual variance after the disentangled 2$^{\text{nd}}$ stage (yellow line), we can see the difference in implementing a standard controller at 1 kHz and one running at 4 kHz. This is consistent with the analytical prediction that the temporal error is proportional to $f_c^{-5/3}$ (with f_c denoting the correction frequency), so one would expect an about ten times improvement for a four times faster correction.

We can also see in Figure 4.4 that an even better correction is achieved using the LQG controller on the 2$^{\text{nd}}$ stage. Moreover, this gain in overall correction is achieved by the significant improvement in the low order modes (under mode 20), which should result in substantial improvements in contrast at small angular separations.

As we mentioned and showed in Chapter 3, the residual point spread function (PSF) contrast in figure 4.5 presents another important performance metric for high-contrast imaging. We calculate the residual PSF from the residual WFE assuming that Airy diffraction pattern has been removed by an idealized perfect coronagraph (Cavarroc et al., 2006).

In Figure 4.5 we can see the improvement provided by the disentangled 2$^{\text{nd}}$ stage controller (yellow line) correction demonstrated by a better contrast at separations smaller than $4\lambda/D$. Then, this is a new best performance compared to our results presented in Chapter 3. The best performance for the Proxima Centauri case is achieved by beam-splitting with a dichroic, using 2$^{\text{nd}}$ stage a disentangled LQG

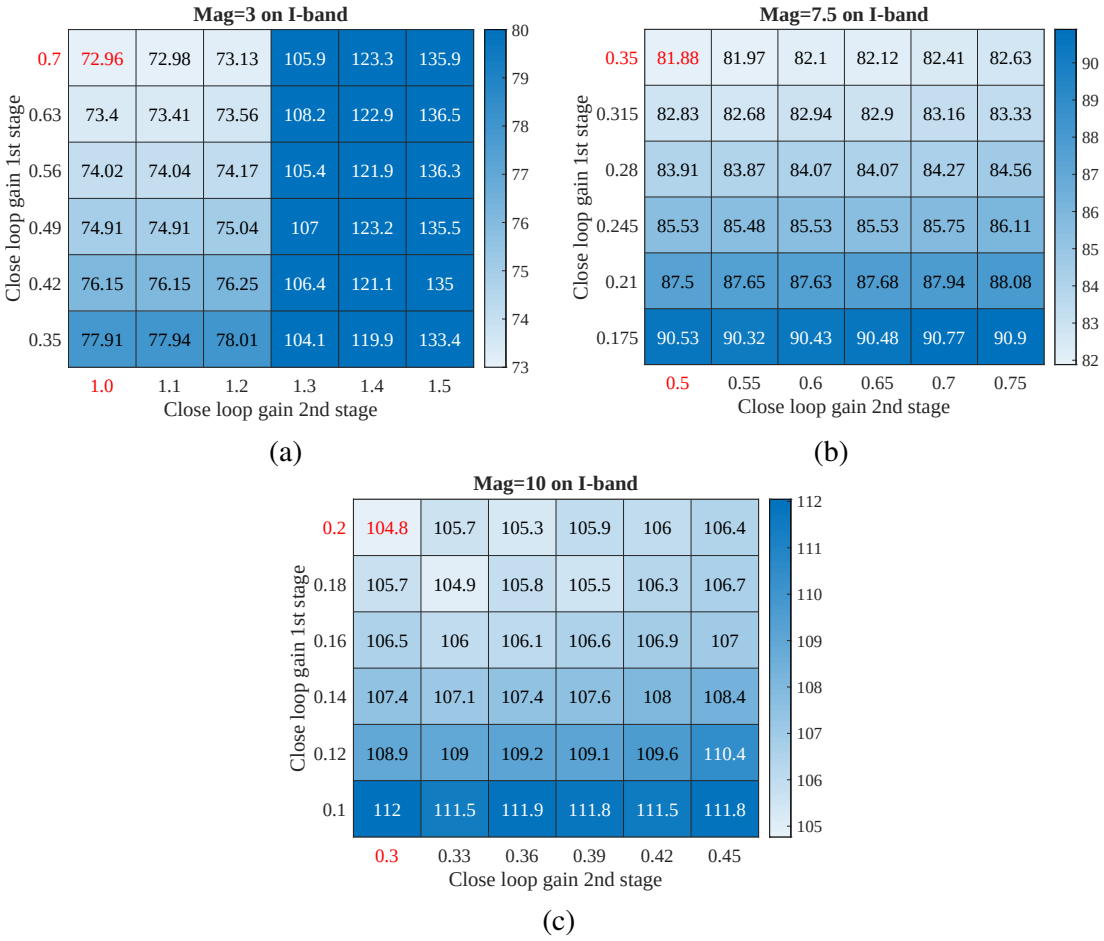

Figure 4.3: Residual WFE [nm RMS] as a function of closed loop gains and three different magnitudes assuming a dichroic beam-splitter and using the disentangling procedure. The gains obtained by independently optimizing each stage are the ones in red (upper left corner of the heatmaps), and we can see that there is no need for a joint optimization process.

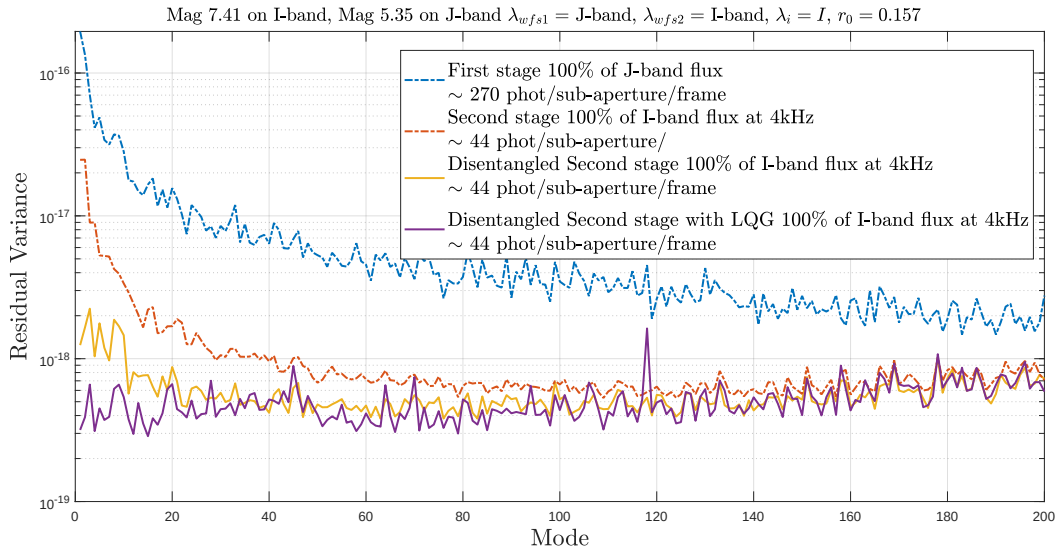

Figure 4.4: Residual Variance in terms of K-L modes for an atmosphere with $r_0 = 0.157$, dichroic beamsplitting. We present results with and without using 2$^{\text{nd}}$ stage disentangled control and with an LQG controller on the 2$^{\text{nd}}$ stage.

regulator. This configuration at the maximum angular separations of Proxima b of about 40 mas or 2 λ/D for an 8-m telescope observing at 760 nm reaches a contrast of 1×10^{-4} for $r_0 = 0.1$, and 2×10^{-5} for $r_0 = 0.157$.

With the help of the disentangling procedure, we can fully exploit a 2-stage CAO with a fast 2$^{\text{nd}}$ stage. This way, we can combine the benefits of the PWFS of reducing aliasing error and noise error Vérinaud et al. (2005), and also reduce the temporal error significantly. Disentangling the control of a 4 kHz 2$^{\text{nd}}$ stage added after a 1 kHz 1$^{\text{st}}$ stage increases the raw PSF contrast by a factor of more than 10, compared to a factor 3-5 achieved without such a procedure (Cerpa-Urra et al., 2022).

We can also compare the improvement of the 2$^{\text{nd}}$ stage in contrast at 40 mas as a function of stellar I-band magnitude. In Figure 4.6, we can see that the disentangled CAO system (with integrator or LQG for the 2$^{\text{nd}}$ stage) provides an additional contrast improvement compared to the standard CAO. Even though in Figure 4.4 the reduction of the residual variance of the disentangled CAO using LQG seems to be rather small, the improvement in the low order modes translates into a significant gain in HCI performance.

We further see that with disantangled CAO also the correction and contrast performance degrade with stellar magnitude due to the increased noise and reduced

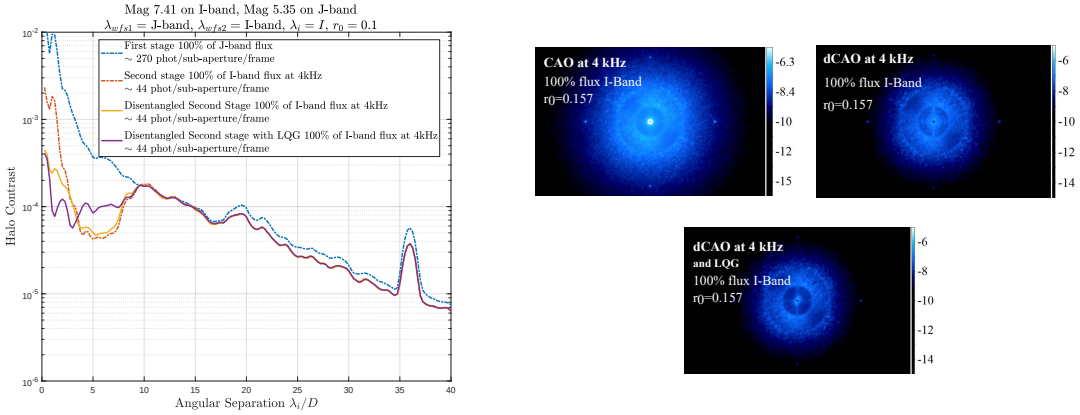

(a)

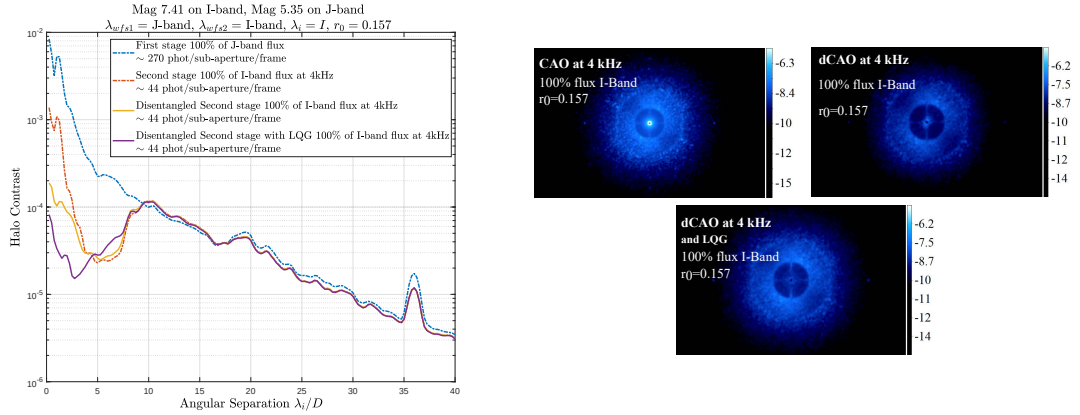

(b)

Figure 4.5: Contrast performance and PSF for (a) $r_0 = 0.1$ and (b) $r_0 = 0.157$ for different CAO schemes, using a dichroic beamsplitting. All the J-Band flux was sent to the 1st stage, and all the I-band flux was sent to the 2nd stage. Scientific analysis is done in I-band."dCAO" stands for Disentangled CAO.

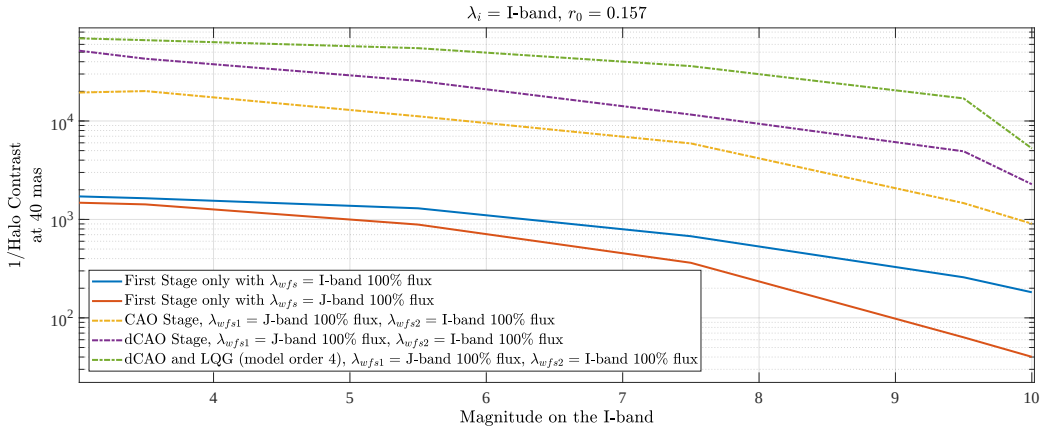

Figure 4.6: PSF residual contrast as a function of magnitude at an angular separations of 40 mas for different configurations of CAO. "dCAO" stands for Disentangled CAO.

optimum integrator gains. In contrast to the residual wavefront error, the contrast in the bright end does not levels out quickly because of a dominating fitting error which occurs at spatial frequencies beyond the correction radius of the AO and would not affect the contrast at small angular separations. In the faint end, the CAO system, with or without disentangled control, degrades less rapidly because its 2$^{\text{nd}}$ stage stage is operated by the more sensitive Pyramid WFS.

4.5.2 Analysis of AO residual speckle lifetime

We analyzed the speckle lifetime of the disentangled CAO residual PSF in the same way as it was done for the standard CAO in Chapter 3 .

It is important to emphasize that our simulations do not include NCPAs, so we are only looking at the temporal evolution of residual atmospheric turbulence speckle intensities.

Again, we apply published analysis Milli, Banas, et al., 2016 on our simulated coronagraphic images and compare speckle lifetimes for single and double-stage AO correction. We analysed three annular regions at different angular separations from the PSF center: $A_1 = 2$–$5[\frac{\lambda}{D}]$, $A_2 = 5$–$8[\frac{\lambda}{D}]$ and $A_3 = 12$–$15[\frac{\lambda}{D}]$ as indicated in Fig. 4.7. While A_1 and A_2 are inside the correction radius and controlled by both stages of the CAO, A_3 is only affected by the 1$^{\text{st}}$ stage and could therefore show a different speckle lifetime. We simulated a short 2.5 seconds observation with $r_0 = 0.157$ m and an elevated wind speed, 50 % higher than the wind speed used for the performance simulations.

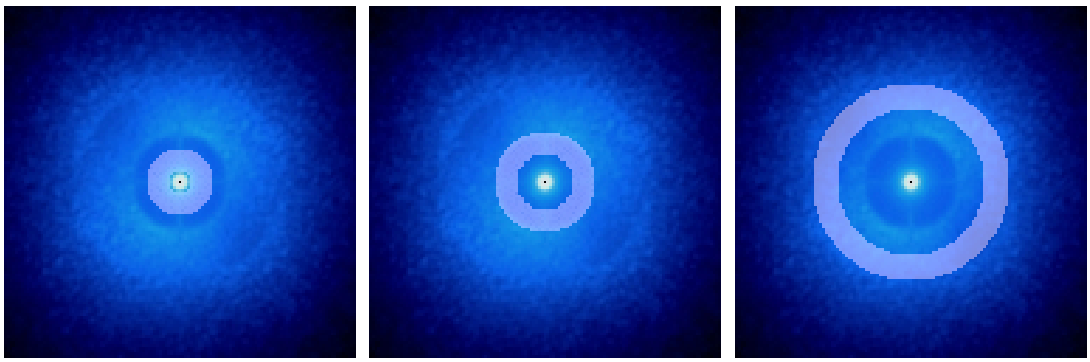

(a) (b) (c)

Figure 4.7: Long exposure perfect coronagraph PSF with different regions A over imposed. (a): $A_1 = 2\text{–}5[\frac{\lambda}{D}]$ (b): $A_2 = 5\text{–}8[\frac{\lambda}{D}]$ and (c): $A_3 = 12\text{–}15[\frac{\lambda}{D}]$.

The results are shown Fig. 4.8. In Section 3.2, we showed that for a standard CAO system, the low-frequency part of the CAO's loop correction transfer function is very similar to the one of a double-integrator controller. For example, in the regions A_1 and A_2, we clearly see the effect of the 2^{nd} stage, but in the case of the disentangled CAO, this is no longer the case. Now the CAO system behaves like a stand-alone stage. Furthermore, even when using an LQG controller, the speckle lifetime is not much reduced compared to the 1^{st} stage.

4.6 Conclusions

In this chapter, we have studied what we have called disentangled CAO, and have applied this strategy using an integrator and an LQG regulator for the 2^{nd} stage. We showed how the disentangled CAO control worked and the theory behind it. We showed that the 2^{nd} stage was modified in such a way that it then behaves like a stand-alone controller. To be able to implement an LQG regulator, we presented the modeling of the incoming turbulence that is used to build the LQG controller. Because of the nature of the CAO system, we had to use the so-called adapter procedure proposed in (Raynaud, Kulcsár, Juvénal, et al., 2016) and implement a bumpless-switch. This switch prevented a violent transient "bump" on the total CAO correction when we switch on a disentangled 2^{nd} stage controller with its internal state initialized at zero.

By running a numerical simulation, we demonstrated how a disentangled CAO system using an LQG regulator in the 2^{nd} stage can be an even more efficient way to improve the contrast performance of an existing XAO system at very small

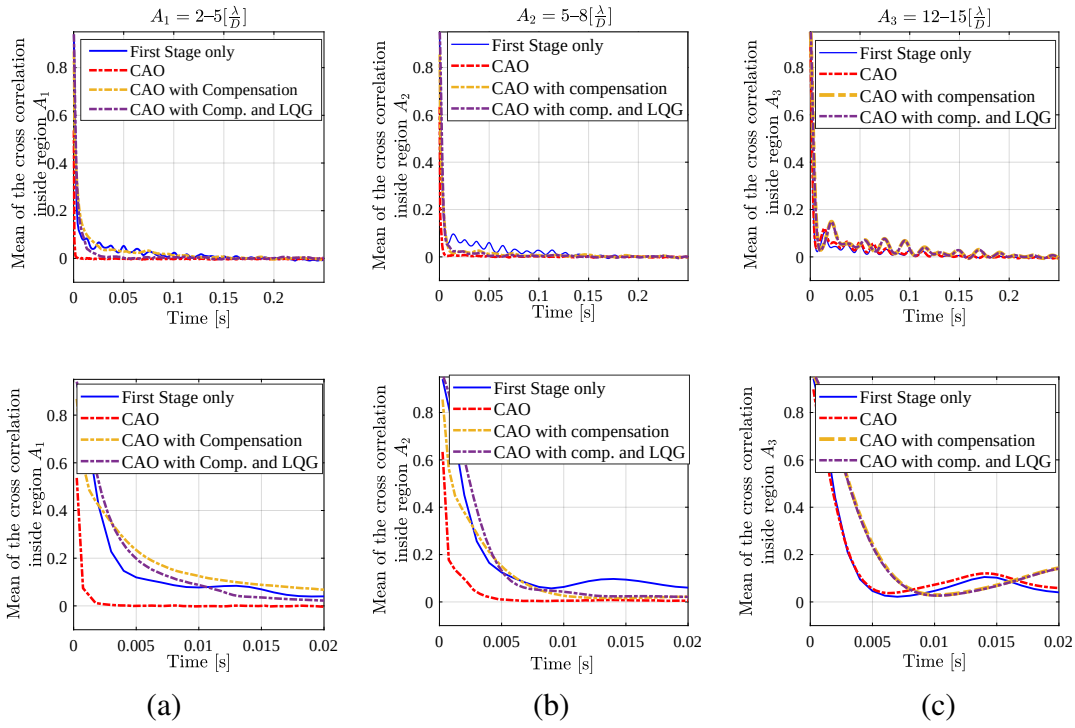

Figure 4.8: Temporal decorrelations of all the pixels inside A for three different regions: (a) $A_1 = 2\text{–}5[\frac{\lambda}{D}]$, (b) $A_2 = 5\text{–}8[\frac{\lambda}{D}]$ and (c) $A_3 = 12\text{–}15[\frac{\lambda}{D}]$ using the disentangled CAO with an LQG regulator. The panels on the bottom zoom in on very short timescales.

angular separation. Then, this is a new best performance compared to our results presented in Chapter 3, and we can fully exploit a 2-stage CAO with a fast 2^{nd} stage by reducing the impact of the non-stationary and high-frequency signal coming from the 1^{st} stage.

Using a standard CAO with a four times faster 2^{nd} stage, we reduce the decorrelation or lifetime of atmospheric turbulence speckles by a factor of 30-50 over the lifetime observed with the 1^{st} stage only, because of the double-integrator like rejection transfer function for the low temporal frequencies. That is no longer the case of the disentangled CAO, and even though we do not achieve to smoothen the residual PSF as efficiently as with the regular CAO, we are still able to increase significantly the raw contrast of the PSF, hence the contrast performance. To achieve even better corrections using a disentangled CAO system, then we would need to increase the rejection at low temporal frequencies. For this, we could use an additional integrator to the LQG by augmenting the state. This way, we could customize the disturbance rejection and reduce the speckle lifetime using a disentangled CAO system. Of course, this would come with more amplification somewhere else due to water-bed effect, and needs a careful tuning to reach a good compromise.

Chapter 5

Conclusions and perspectives

5.1 Conclusions

In the first part of this manuscript, we focused on presenting the research context. We introduced AO and, more specifically, XAO. We established how the next generation of large-scale telescopes like the ELT will enable scientists to image Earth-like planets around the nearest stars and how the limits of AO are being pushed further and further. Then we focused on the exoplanet science case. We introduced exoplanetary science as one of the most rapidly developing fields in astrophysics and described the methods currently used. We explained how by using RV, transits, and other methods, scientists have developed a basic statistical understanding of the inner regions of planetary systems. However, these methods detect no light from the exoplanets themselves. Hence, even the most fundamental physical parameters of these planets (luminosity and temperature) are not measured, and direct imaging is needed for a comprehensive study of exoplanet population and properties.

We describe in Chapter 1 how direct imaging will allow us to characterize the planets and their atmospheres (Kasper, Cerpa Urra, et al., 2021). Nevertheless, the very demanding contrast requirements for Earth-like planets observations are not yet achievable with the current telescopes and instrumentation. This is where XAO is used at its most capacity. The XAO objective is to increase the Strehl ratio of the corrected PSF to well above 70% at the observing wavelength. We explained how each component of an XAO system is pushed to its limits, and a significant amount of research and development is done to be able to minimize as much as possible the residual variance of the wavefront. Then, we described in Chapter 2 each component of the AO system. With a particular emphasis on the control theory of AO. We studied the chronogram of an AO loop and described the most common controllers, namely an integral action controller (or

integrator) and a Linear Quadratic Gaussian (LQG) controller. We highlighted the importance of obtaining excellent contrast sensitivity for exoplanet imaging at small angular separations and how it was crucial to minimize this residual halo typically dominated by the AO temporal delay at small angular separations (Guyon, 2005).

In Chapter 3, we introduced that a straightforward approach to reduce the temporal delay would be to run the AO system faster at the expense of increased detector read-noise, and we proposed a Cascade Adaptive optics (CAO) system with two stages. The work was focused on (i) developing a modal control analysis by computing the frequency response of the closed-loop system, (ii) analyzing the performance by numerical simulations in terms of contrast, and (iii) analyzing the performance of the system in terms of residual speckle lifetime. From the modal control analysis, we could see that the 1st stage residuals propagate in the 2nd stage under the form of a non-stationary signal with a high-frequency content that the 2nd stage cannot properly handle due to the integrator overshoot. To run the numerical simulations, we have to make assumptions about the WFS types, the framerate at which these are running, and the beam-splitting between the two. We choose the Shack-Hartmann Wavefront Sensor (SHWFS) to drive the 1st stage, and for the 2nd, we choose an unmodulated Pyramid WFS (PWS). We also explored two different options for the beam-splitting between the two stages: a) an optimized gray beam-splitting with a variable fraction of the I-band intensity distributed between the two stages, and b) dichroic beam-splitting with the 1st stage operating at a longer wavelength in the J-band, and the 2nd stage operating in I-band. Also, to obtain the best possible performance, we had to jointly optimize the gain values of both stages for both beam-splitting cases. Having determined the optimum integrator gains and split ratios for the CAO system, we then compared the performance of both splitting concepts. We quantified the correction improvement provided by the 2nd stage. We demonstrated that a CAO system using a dichroic beam-splitting could be an efficient way to improve the contrast performance of an existing XAO system. We also showed how an unmodulated PWFS could improve performance. We showed how using a simple integrator control for both stages, where the second stage runs at four times the framerate of the first one, increases the contrast by about one order of magnitude and reduces the decorrelation or lifetime of atmospheric turbulence speckles by a factor of 30 to 50 over the lifetime observed with the first stage only.

However, it was natural to wonder if the impact of the non-stationary and high-frequency signal coming from the 1st stage could be better handled to limit its nefarious effect in the 2nd stage and how an LQG regulator in the 2nd stage could impact the performance. So, in Chapter 4 we presented a new CAO configuration using a woofer-tweeter kind of compensation method which we dubbed «

disentangled CAO control ». In this new CAO scheme, the control applied in the 1st stage is sent to the 2nd stage which then behaves as if it were compensating for the whole incoming turbulence, but with the control effort split between both stages. We demonstrated that by using this scheme, the CAO system does not show the behavior of a double integrator at low temporal frequencies but of a single integrator. This translates into an increased speckle lifetime (compared to the standard CAO presented in Chapter 3). However, there is an important increase in performance at separations smaller than $4\lambda/D$. The use of the LQG controller then achieves even better performance. As the LQG controller is based on a model of the disturbance, we proposed a modal modeling of the turbulent phase using a Prediction Error Minimization(PEM) approach. PEM has proved to be suitable for cases where there may not be prior information on the disturbance. This method could identify, for each mode, a full state model directly from a temporal sequence of K-L modes. The disentangled CAO system showed a significant improvement of the proposed CAO structure over a single-stage XAO system or over the standard CAO structure proposed initially. Using the LQG regulator further improves the contrast, particularly at low angular separation. Such a performance would, for example, bring the detection of oxygen in the atmosphere of Proxima b (if it were present in an Earth-like abundance) within reach.

5.2 Perspectives

In this thesis's framework, we demonstrated how the CAO system could be an efficient way to improve the performance of already existing XAO systems (i.e., SAXO+, KPIC, MagAO, SCeXAO).

One of CAO's main advantages is that it can relax the DM requirements for a 2nd stage. DMs with a high number of actuators, fast response, and large stroke are nonexistent to date and would be extremely difficult to build in the ELT context. With CAO, we can use a fast DM with a smaller stroke and still achieve high performance for XAO.

The RTC requirements for a CAO system are not that far from the ordinary. The 1st stage is a standard AO system that may even be already implemented, and even though the frequency rate of the 2nd stage is high, the potentially lower number of actuators of the 2nd stage relaxes the RTC requirements.

As mentioned in Chapter 2, CAO architecture is already being studied to be part of future XAO instruments. For the ELT, M4 does not have enough actuators and speed for XAO in the optical/NIR needed for PCS. A second DM is required, and a 2-stage CAO seems to be a very efficient way to control the PCS XAO.

Future studies could be carried out to further improve CAO system performance. As presented in Section 4.5, the speckle lifetime at small angular separa-

tions of the PSF is not reduced using the disentangled CAO controller. For this, we could study ways to increase rejection further at low temporal frequencies. One way would be to modify the 2nd stage control strategy by using the 1st stage measurements in such a way that low temporal frequency compensation is enforced. For this, a simple solution could be to combine the LQG regulator with a leaky integrator, as often done to cut static errors (Anderson and Moore, 1990, p. 94).

Also one could have a closer look at the 2nd stage PWFS linearity. In our study, we did not address potential non-linearities. We assumed that these were probably not too much of an issue because we are dealing with the 1st stage residual errors only, instead of a full atmospheric turbulence. It would be interesting to use an optical gain compensation (Deo, Gendron, Rousset, Vidal, Sevin, et al., 2019) to evaluate its impact on performance.

Also, all the introduced methods and simulations should now be tested experimentally. The GPU-based High-Order adaptive opticS Testbench (GHOST) (Engler et al., 2022) can be a good starting point. GHOST has been developed by ESO, ETH Zurich and ANU, and is located at ESO's AO laboratory. It features a Spatial Light Modulator (SLM) to inject programmable turbulence, and its XAO system consists of a PWFS using a GPU-based RTC. The RTC is built around the COSMIC framework so it is flexible enough to implement various 2nd stage controllers. The SLM can be used to replicate 1st stage residuals, and the 2nd stage can be tested using the bench components. Eventually, after successful laboratory testing, promising methods to control a CAO should be tested on sky. For this, SAXO+ (Vidal et al., 2022) can be a good opportunity, leading to add a fast 2nd stage to the SAXO system of the SPHERE instrument.

With all this, CAO could be part of ongoing or future instruments. Imaging small Exoplanets around nearby stars with the ELT is possible if we have a carefully designed XAO and a two-stage CAO system.

Abbreviations

ADI Angular Differential Imaging.

AO Adaptive Optics.

AU Astronomical Units.

CCD Charge Coupled Device.

DDSPC data-driven subspace predictive control.

DM Deformable Mirror.

ELT Extremly Large Telescope.

EOF Empirical Orthogonal Functions.

ESO European Southern Observatory.

GHOST GPU-based High-Order adaptive opticS Testbench.

GPI Gemini Planet Imager.

HARPS High Accuracy Radial velocity Planet Searcher.

HCI High-contrast Imaging.

HDS High-Dispersion Spectrum.

JWST James Webb Space Telescope.

LGS Laser Guide Stars.

LQG Linear Quadratic Gaussian.

NCPA Non-common Path Aberrations.

NEAR New Earths in the Alpha Cen Region.

NIR Near-InfraRed.

NOAO US National Optical Astronomy Observatories.

OG Optical Gain.

OMGI Optimized Modal Gain Integrator.

OOMAO Object Oriented Matlab Adaptive Optics.

PCS ELT Planetary Camera and Spectrograph.

PEM Prediction Error Minimization.

PSD Power Spectral Density.

PSF Point Spread Function.

PWFS Pyramid Wave-front Sensor.

RV Radial Velocity.

SCExAO Subaru Coronagraphic Extreme Adaptive Optics.

SHWFS Shack-Hartmann Wavefront Sensor.

SLM Spatial Light Modulator.

SPHERE Spectro-Polarimetric High-contrast Exoplanet Research.

SR Strehl ratio.

TSVD Truncated Singular Values Decomposition.

VLT Very Large Telescope.

WFS Wavefront Sensor.

XAO Extreme Adaptive Optics.

Bibliography

Aime, C. and R. Soummer (Sept. 2004). "The Usefulness and Limits of Coronagraphy in the Presence of Pinned Speckles". In: *apjl* 612.1, pp. L85–L88. DOI: 10.1086/424381.

Alibert, Y. et al. (Oct. 2013). "Theoretical models of planetary system formation: mass vs. semi-major axis". In: *A&A* 558, A109. DOI: 10.1051/0004-6361/201321690.

Anderson, B. and John B. Moore (1990). "Optimal control: linear quadratic methods". In.

Anglada-Escudé, G. et al. (Aug. 2016). "A terrestrial planet candidate in a temperate orbit around Proxima Centauri". In: *Nature* 536, pp. 437–440. DOI: 10.1038/nature19106.

Babcock, H. W. (Oct. 1953). "The Possibility of Compensating Astronomical Seeing". In: *PASP* 65, p. 229. DOI: 10.1086/126606. URL: https://doi.org/10.1086/126606.

Baraffe, I. et al. (May 2003). "Evolutionary models for cool brown dwarfs and extrasolar giant planets. The case of HD 209458". In: *A&A* 402, pp. 701–712. DOI: 10.1051/0004-6361:20030252.

Beuzit, J. -L. et al. (Nov. 2019a). "SPHERE: the exoplanet imager for the Very Large Telescope". In: *A&A* 631, A155. DOI: 10.1051/0004-6361/201935251.

— (Nov. 2019b). "SPHERE: the exoplanet imager for the Very Large Telescope". In: *A&A* 631. _eprint: 1902.04080, A155. DOI: 10.1051/0004-6361/201935251.

Bloemhof, E. E. et al. (Sept. 2001). "Behavior of Remnant Speckles in an Adaptively Corrected Imaging System". In: *apjl* 558.1, pp. L71–L74. DOI: 10.1086/323494.

Boccaletti, A. et al. (2020). *SPHERE+: Imaging young Jupiters down to the snow-line*. arXiv: Earth and Planetary Astrophysics.

Bond, Charlotte Z. et al. (2020). "Adaptive optics with an infrared pyramid wavefront sensor at Keck". In: *JATIS* 6.3, pp. 1–21. DOI: 10.1117/1.JATIS.6.3.039003. URL: https://doi.org/10.1117/1.JATIS.6.3.039003.

Boss, A. P. (1997). "Giant planet formation by gravitational instability." In: *Science* 276, pp. 1836–1839. DOI: 10.1126/science.276.5320.1836.

Boyer, Corinne, Vincent Michau, and Gerard Rousset (Aug. 1990). "Adaptive optics: interaction matrix measurements and real time control algorithms for the COME-ON project." In: *Amplitude and Intensity Spatial Interferometry*. Ed. by Jim B. Breckinridge. Vol. 1237. Society of Photo-Optical Instrumentation Engineers (SPIE) Conference Series, pp. 406–421. DOI: 10.1117/12.19313.

Burrows, A. et al. (Dec. 1997). "A Nongray Theory of Extrasolar Giant Planets and Brown Dwarfs". In: *ApJ* 491, pp. 856–875. DOI: 10.1086/305002.

Campbell, H. I. and A. Greenaway (2006). "Wavefront sensing: From historical roots to the state-of-the-art". In: *Eas Publications Series* 22, pp. 165–185.

Cantalloube, F. et al. (2020). "Wind-driven halo in high-contrast images - I. Analysis of the focal-plane images of SPHERE". In: *A&A* 638, A98. DOI: 10.1051/0004-6361/201937397. URL: https://doi.org/10.1051/0004-6361/201937397.

Carter, Aarynn et al. (Aug. 2022). *The JWST Early Release Science Program for Direct Observations of Exoplanetary Systems I: High Contrast Imaging of the Exoplanet HIP 65426 b from 2-16 μm*. DOI: 10.48550/arXiv.2208.14990.

Cavarroc, C. et al. (Feb. 2006). "Fundamental limitations on Earth-like planet detection with extremely large telescopes". In: *A&A* 447, pp. 397–403. DOI: 10.1051/0004-6361:20053916.

Cerpa-Urra, Nelly et al. (Jan. 2022). "Cascade adaptive optics: contrast performance analysis of a two-stage controller by numerical simulations". In: *Journal of Astronomical Telescopes, Instruments, and Systems* 8, 019001, p. 019001. DOI: 10.1117/1.JATIS.8.1.019001. arXiv: 2201.11690 [astro-ph.IM].

Chambouleyron, V. et al. (Dec. 2020). "Pyramid wavefront sensor optical gains compensation using a convolutional model". In: *A&A* 644. _eprint: 2006.08294, A6. DOI: 10.1051/0004-6361/202037836.

Charbonneau, D. et al. (Jan. 2007). "When Extrasolar Planets Transit Their Parent Stars". In: *Protostars and Planets V*. Ed. by Bo Reipurth, David Jewitt, and Klaus Keil, p. 701. arXiv: astro-ph/0603376 [astro-ph].

Chazelas, Bruno et al. (Dec. 2020). "RISTRETTO: a pathfinder instrument for exoplanet atmosphere characterization". In: *Adaptive Optics Systems VII*. Vol. 11448. International Society for Optics and Photonics, p. 1144875. DOI: 10.1117/12.2576316. URL: https://www.spiedigitallibrary.org/conference-proceedings-of-spie/11448/1144875/RISTRETTO-a-pathfinder-instrument-for-exoplanet-atmosphere-characterization/10.1117/12.2576316.short (visited on 01/16/2021).

Chilcote, Jeffrey et al. (2020). "GPI 2.0: upgrading the Gemini Planet Imager". In: *Ground-based and Airborne Instrumentation for Astronomy VIII*. Ed. by Christopher J. Evans, Julia J. Bryant, and Kentaro Motohara. Vol. 11447.

SPIE, pp. 394–407. DOI: 10.1117/12.2562578. URL: https://doi.org/10.1117/12.2562578.

Claudi, R. U. et al. (July 2008). "SPHERE IFS: the spectro differential imager of the VLT for exoplanets search". In: *Society of Photo-Optical Instrumentation Engineers (SPIE) Conference Series*. Vol. 7014. Society of Photo-Optical Instrumentation Engineers (SPIE) Conference Series, p. 3. DOI: 10.1117/12.788366.

Conan, Rodolphe and C Correia (2014). "Object-oriented Matlab adaptive optics toolbox". In: *Adaptive optics systems IV*. Vol. 9148. International Society for Optics and Photonics, p. 91486C.

Correia, C, J-P Véran, et al. (2011). "Advanced NGS-mode control in NFIRAOS using split-tomography". In: *Adaptive Optics: Methods, Analysis and Applications*. Optica Publishing Group, AMB4.

Correia, C. M., K. Jackson, et al. (June 2015). "Spatio-angular minimum-variance tomographic controller for multi-object adaptive-optics systems". In: *Appl. Opt.* 54, p. 5281. DOI: 10.1364/AO.54.005281.

De Souza, Carlos and Graham Goodwin (Sept. 1984). "Intersample variances in discrete minimum variance control". In: *Automatic Control, IEEE Transactions on* 29, pp. 759–761. DOI: 10.1109/TAC.1984.1103632.

Dekany, Richard et al. (Oct. 2013). "PALM-3000: Exoplanet Adaptive Optics for the 5 m Hale Telescope". In: *apj* 776.2, 130, p. 130. DOI: 10.1088/0004-637X/776/2/130. arXiv: 1309.1216 [astro-ph.IM].

Deo, V., É. Gendron, G. Rousset, Vidal, and T. Buey (2018). "A modal approach to optical gain compensation for the pyramid wavefront sensor". In: *Adaptive Optics Systems VI*. Ed. by Laird M. Close, Laura Schreiber, and Dirk Schmidt. Vol. 10703. Backup Publisher: International Society for Optics and Photonics. SPIE, pp. 653–670. DOI: 10.1117/12.2311631. URL: https://doi.org/10.1117/12.2311631.

Deo, V., É. Gendron, G. Rousset, F. Vidal, A. Sevin, et al. (Sept. 2019). "A telescope-ready approach for modal compensation of pyramid wavefront sensor optical gain". In: *A&A* 629, A107. DOI: 10.1051/0004-6361/201935847.

Dessenne, C, P-Y Madec, and G Rousset (1999). "Sky implementation of modal predictive control in adaptive optics". In: *Optics letters* 24.5. Publisher: Optical Society of America, pp. 339–341.

— (Oct. 1997). "Modal prediction for closed-loop adaptive optics". In: *Optics Letters* 22, pp. 1535–1537. DOI: 10.1364/OL.22.001535.

Díaz, R. F. et al. (May 2019). "The SOPHIE search for northern extrasolar planets. XIV. A temperate ($T_{eq} \sim 300$ K) super-earth around the nearby star Gliese 411". In: *A&A* 625, A17. DOI: 10.1051/0004-6361/201935019.

Doelman, N., R. Fraanje, and R. Breeje (2011). "Optimal control of tip-tilt modes: on-sky adaptive optics demonstration". In: *2nd International Conference on Adaptive Optics for Extremely Large Telescopes (AO4ELT)*.

Doelman, Niek, Rufus Fraanje, and Remco den Breeje (2011). "Real-sky adaptive optics experiments on optimal control of tip-tilt modes". In: *Second International Conference on Adaptive Optics for Extremely Large Telescopes*. P. 51.

Dohlen, K. et al. (July 2008). "The infra-red dual imaging and spectrograph for SPHERE: design and performance". In: *Society of Photo-Optical Instrumentation Engineers (SPIE) Conference Series*. Vol. 7014. Society of Photo-Optical Instrumentation Engineers (SPIE) Conference Series, p. 3. DOI: 10.1117/12.789786.

Engler, Byron et al. (2022). "The GPU-based High-order adaptive OpticS Testbench". In: *Adaptive Optics Systems VIII*. Ed. by Laura Schreiber, Dirk Schmidt, and Elise Vernet. Vol. 12185. International Society for Optics and Photonics. SPIE, p. 1218558. DOI: 10.1117/12.2630595. URL: https://doi.org/10.1117/12.2630595.

ESO (2022). *The Extremely Large Telescope Official Web-page*. URL: https://elt.eso.org/ (visited on 07/05/2022).

Esposito, S., A. Puglisi, et al. (Apr. 2020). "On-sky correction of non-common path aberration with the pyramid wavefront sensor". In: *aap* 636, A88, A88. DOI: 10.1051/0004-6361/201937033.

Esposito, S. and A. Riccardi (Apr. 2001). "Pyramid Wavefront Sensor behavior in partial correction Adaptive Optic systems". In: *aap* 369, pp. L9–L12. DOI: 10.1051/0004-6361:20010219.

Esposito, Simone, Enrico Pinna, et al. (Oct. 2015). "Non common path aberration correction with non linear WFSs". In: *Adaptive Optics for Extremely Large Telescopes IV (AO4ELT4)*, E36, E36.

Fauvarque, Olivier et al. (Jan. 2017). "General formalism for Fourier-based wave front sensing: application to the pyramid wave front sensors". In: *Journal of Astronomical Telescopes, Instruments, and Systems* 3, 019001, p. 019001. DOI: 10.1117/1.JATIS.3.1.019001. arXiv: 1607.03269 [astro-ph.IM].

Fontanella, J C (Nov. 1985). "Wavefront sensing deconvolution and adaptive optics". In: *J. Opt.* 16.6, pp. 257–268. DOI: 10.1088/0150-536x/16/6/002. URL: https://doi.org/10.1088/0150-536x/16/6/002.

Fraanje, Rufus et al. (Nov. 2010). "Fast reconstruction and prediction of frozen flow turbulence based on structured Kalman filtering". In: *JOSA A* 27.11. Publisher: OSA, A235–A245.

Fried, D. L. (Mar. 1977). "Least-squares fitting a wave-front distortion estimate to an array of phase-difference measurements". In: *Journal of the Optical Society of America (1917-1983)* 67.3, p. 370.

Fusco, T., G. Rousset, et al. (Jan. 2006). "High-order adaptive optics requirements for direct detection of extrasolar planets: Application to the SPHERE instrument". In: *Optics Express* 14.17, p. 7515. DOI: 10.1364/OE.14.007515.

Fusco, T., J.-F. Sauvage, et al. (Aug. 2014). "Final performance and lesson-learned of SAXO, the VLT-SPHERE extreme AO: from early design to on-sky results". In: *Society of Photo-Optical Instrumentation Engineers (SPIE) Conference Series*. Vol. 9148. Society of Photo-Optical Instrumentation Engineers (SPIE) Conference Series, p. 1. DOI: 10.1117/12.2055423.

Gaffard, J. P. and Corinne Boyer (Sept. 1987). "Adaptive optics for optimization of image resolution". In: *Appl. Opt.* 26.18, pp. 3772–3777. DOI: 10.1364/AO.26.003772. URL: http://ao.osa.org/abstract.cfm?URI=ao-26-18-3772.

Gavel, Donald T. and Donald Wiberg (Feb. 2003). "Toward Strehl-optimizing adaptive optics controllers". In: *Adaptive Optical System Technologies II*. Ed. by Peter L. Wizinowich and Domenico Bonaccini. Vol. 4839. Society of Photo-Optical Instrumentation Engineers (SPIE) Conference Series, pp. 890–901. DOI: 10.1117/12.459684.

Gendron, Eric (Mar. 1995). "Optimisation de la commande modale en optique adaptative : applications à l'astronomie". Theses. Université Denis Diderot (Paris 7). URL: https://hal.archives-ouvertes.fr/tel-01418424.

Glück, M., J. Pott, and O. Sawodny (2018). "Model Predictive Control of Multi-Mirror Adaptive Optics Systems". In: *2018 IEEE Conference on Control Technology and Applications (CCTA)*, pp. 909–914. DOI: 10.1109/CCTA.2018.8511551.

Goebel, Sean B. et al. (Sept. 2018). "Measurements of Speckle Lifetimes in Near-infrared Extreme Adaptive Optics Images for Optimizing Focal Plane Wavefront Control". In: *PASP* 130.992, p. 104502. ISSN: 1538-3873. DOI: 10.1088/1538-3873/aad8ed. URL: https://doi.org/10.1088/1538-3873/aad8ed (visited on 02/15/2021).

Goldreich, P. and S. Tremaine (Oct. 1980). "Disk-satellite interactions". In: *ApJ* 241, pp. 425–441. DOI: 10.1086/158356.

Guyon, O. (Aug. 2005). "Limits of Adaptive Optics for High-Contrast Imaging". In: *ApJ* 629.1, pp. 592–614. ISSN: 0004-637X, 1538-4357. DOI: 10.1086/431209. URL: https://iopscience.iop.org/article/10.1086/431209 (visited on 12/20/2020).

— (Sept. 2018). "Extreme Adaptive Optics". In: *araa* 56, pp. 315–355. DOI: 10.1146/annurev-astro-081817-052000.

Guyon, O. and J. Males (2017). *Adaptive Optics Predictive Control with Empirical Orthogonal Functions (EOFs)*. arXiv: Instrumentation and Methods for Astrophysics.

Guyon, O., E. A. Pluzhnik, M. J. Kuchner, et al. (Nov. 2006). "Theoretical Limits on Extrasolar Terrestrial Planet Detection with Coronagraphs". In: *apjs* 167.1, pp. 81–99. DOI: 10.1086/507630. arXiv: astro-ph/0608506 [astro-ph].

Guyon, Olivier, Eugene A. Pluzhnik, Raphael Galicher, et al. (Mar. 2005). "Exoplanet Imaging with a Phase-induced Amplitude Apodization Coronagraph. I. Principle". In: *APJ* 622.1, pp. 744–758. DOI: 10.1086/427771. arXiv: astro-ph/0412179 [astro-ph].

Haffert, Sebastiaan Y, Jared R Males, Laird M Close, et al. (2021). "Data-driven subspace predictive control of adaptive optics for high-contrast imaging". In: *Journal of Astronomical Telescopes, Instruments, and Systems* 7.2, p. 029001.

Haffert, Sebastiaan Y., Jared R. Males, Kyle Van Gorkom, et al. (2022). "Advanced wavefront sensing and control demonstration with MagAO-X". In: *Adaptive Optics Systems VIII*. Ed. by Laura Schreiber, Dirk Schmidt, and Elise Vernet. Vol. 12185. International Society for Optics and Photonics. SPIE, p. 1218581. DOI: 10.1117/12.2630425. URL: https://doi.org/10.1117/12.2630425.

Hardy, J. W., J. E. Lefebvre, and C. L. Koliopoulos (Mar. 1977). "Real-time atmospheric compensation". In: *JOSA* 67.3, pp. 360–369. DOI: 10.1364/JOSA.67.000360. URL: http://www.osapublishing.org/abstract.cfm?URI=josa-67-3-360.

Heritier, Cedric Taïssir (Nov. 2019). "Innovative Calibration Strategies for Large Adaptive Telescopes with Pyramid Wave-Front Sensors". Theses. Aix Marseille Université. URL: https://tel.archives-ouvertes.fr/tel-02390861.

Hinnen, Karel, Michel Verhaegen, and Niek Doelman (2007). "Exploiting the spatiotemporal correlation in adaptive optics using data-driven H_2-optimal control". In: *JOSA A* 24.6. Publisher: Optical Society of America, pp. 1714–1725.

Jovanovic, N. et al. (Sept. 2015). "The Subaru Coronagraphic Extreme Adaptive Optics System: Enabling High-Contrast Imaging on Solar-System Scales". In: *pasp* 127.955, p. 890. DOI: 10.1086/682989. arXiv: 1507.00017 [astro-ph.IM].

Juvenal, Rémy et al. (Oct. 2015). "Tip-tilt modelling and control for GeMS: a performance comparison of identification techniques". In: *Adaptive Optics for Extremely Large Telescopes IV (AO4ELT4)*, E64, E64.

Kasper, M., R. Arsenault, et al. (Sept. 2017). "NEAR: Low-mass Planets in α Cen with VISIR". In: *The Messenger* 169, pp. 16–20. DOI: 10.18727/0722-6691/5033.

Kasper, M., N. Cerpa Urra, et al. (Mar. 2021). "PCS — A Roadmap for Exoearth Imaging with the ELT". In: *The Messenger* 182, pp. 38–43. DOI: 10.18727/0722-6691/5221. arXiv: 2103.11196 [astro-ph.IM].

Kasper, Markus (2021). "Extreme Adaptive Optics". In: *The WSPC Handbook of Astronomical Instrumentation*. Chap. Chapter 18, pp. 325–343. DOI: 10.1142/9789811203787_0018. eprint: https://www.worldscientific.com/doi/

pdf/10.1142/9789811203787_0018. URL: https://www.worldscientific.com/doi/abs/10.1142/9789811203787_0018.

Kasper, Markus, Jean-Luc Beuzit, et al. (July 2010). "EPICS: direct imaging of exoplanets with the E-ELT". In: *Ground-based and Airborne Instrumentation for Astronomy III*. Ed. by Ian S. McLean, Suzanne K. Ramsay, and Hideki Takami. Vol. 7735. Society of Photo-Optical Instrumentation Engineers (SPIE) Conference Series, 77352E, 77352E. DOI: 10.1117/12.856850.

Kolmogorov, A. (Jan. 1941a). "The Local Structure of Turbulence in Incompressible Viscous Fluid for Very Large Reynolds' Numbers". In: *Akademiia Nauk SSSR Doklady* 30, pp. 301–305.

Kolmogorov, Andrej Nikolaevich (1941b). "On the degeneration of isotropic turbulence in an incompressible viscous fluid". In: *Dokl. Akad. Nauk SSSR* 31, pp. 319–323. URL: https://cds.cern.ch/record/739747.

Kolmogorov, Andrey Nikolaevich (Apr. 1941c). "Dissipation of Energy in Locally Isotropic Turbulence". In: *Akademiia Nauk SSSR Doklady* 32, p. 16.

Korkiakoski, Visa, Christophe Vérinaud, and Miska Le Louarn (July 2008). "Applying sensitivity compensation for pyramid wavefront sensor in different conditions". In: *Adaptive Optics Systems*. Ed. by Norbert Hubin, Claire E. Max, and Peter L. Wizinowich. Vol. 7015. Society of Photo-Optical Instrumentation Engineers (SPIE) Conference Series, p. 701554. DOI: 10.1117/12.789011.

Korkiakoski, Visa, Christophe Vérinaud, and Miska Le Louarn (Jan. 2008). "Improving the performance of a pyramid wavefront sensor with modal sensitivity compensation". In: *ao* 47.1, p. 79. DOI: 10.1364/AO.47.000079.

Kulcsár, Caroline, Paolo Massioni, et al. (July 2012). "Vibration mitigation in adaptive optics control". In: *Adaptive Optics Systems III*. Ed. by Brent L. Ellerbroek, Enrico Marchetti, and Jean-Pierre Véran. Vol. 8447. Society of Photo-Optical Instrumentation Engineers (SPIE) Conference Series, 84470Z, 84470Z. DOI: 10.1117/12.926050.

Kulcsár, Caroline, Henri-François Raynaud, Cyril Petit, and Jean-Marc Conan (Sept. 2012). "Minimum variance prediction and control for adaptive optics". In: *Automatica* 48.9, pp. 1939–1954. ISSN: 00051098. DOI: 10.1016/j.automatica.2012.03.030. URL: https://linkinghub.elsevier.com/retrieve/pii/S0005109812002750 (visited on 12/20/2020).

Kulcsár, Caroline, Henri-François Raynaud, Cyril Petit, Jean-Marc Conan, and Patrick Viaris de Lesegno (Aug. 2006). "Optimal control, observers and integrators in adaptive optics". In: *Optics Express* 14.17, p. 7464. DOI: 10.1364/OE.14.007464.

Lardière, Olivier et al. (2014). "Multi-object adaptive optics on-sky results with Raven". In: *Adaptive Optics Systems IV*. Vol. 9148. International Society for Optics and Photonics, 91481G.

Le Roux, Brice et al. (July 2004). "Optimal control law for classical and multiconjugate adaptive optics". In: *Journal of the Optical Society of America A* 21.7, p. 1261. ISSN: 1084-7529, 1520-8532. DOI: 10.1364/JOSAA.21.001261. URL: https://www.osapublishing.org/abstract.cfm?URI=josaa-21-7-1261 (visited on 09/03/2018).

Liu, Xuewen et al. (June 2020). "Wavefront prediction using artificial neural networks for open-loop adaptive optics". In: *Monthly Notices of the Royal Astronomical Society* 496.1, pp. 456–464. ISSN: 0035-8711. DOI: 10.1093/mnras/staa1558. URL: https://doi.org/10.1093/mnras/staa1558.

Ljung, L. (1999). *System Identification: Theory for the User*. Prentice Hall information and system sciences series. Prentice Hall PTR. ISBN: 9780136566953. URL: https://books.google.cl/books?id=nHFoQgAACAAJ.

Looze, Douglas P. et al. (1999). "Optimal compensation and implementation for adaptive optics systems". In: *IEEE CDC proc.* Vol. 2. IEEE Conf. on Decision and Control. Phoenix, AZ, USA, pp. 1715–1720.

López-Morales, Mercedes et al. (June 2019). "Optimizing Ground-based Observations of O2 in Earth Analogs". In: *AJ* 158.1, p. 24. DOI: 10.3847/1538-3881/ab21d7. URL: https://doi.org/10.3847/1538-3881/ab21d7.

Lovelock, J. E. (Aug. 1965). "A Physical Basis for Life Detection Experiments". In: *Nature* 207.4997, pp. 568–570. ISSN: 1476-4687. DOI: 10.1038/207568a0. URL: https://doi.org/10.1038/207568a0.

Lozi, Julien et al. (July 2018). "SCExAO, an instrument with a dual purpose: perform cutting-edge science and develop new technologies". In: *Adaptive Optics Systems VI*. Ed. by Laird M. Close, Laura Schreiber, and Dirk Schmidt. Vol. 10703. Society of Photo-Optical Instrumentation Engineers (SPIE) Conference Series. _eprint: 1809.08301, p. 1070359. DOI: 10.1117/12.2314282.

Macintosh, Bruce, James Graham, et al. (July 2006). "The Gemini Planet Imager". In: vol. 6272. DOI: 10.1117/12.672430.

Macintosh, Bruce, Lisa Poyneer, et al. (2005). "Speckle lifetimes in high-contrast adaptive optics". In: *Astronomical Adaptive Optics Systems and Applications II*. Ed. by Robert K. Tyson and Michael Lloyd-Hart. Vol. 5903. International Society for Optics and Photonics. SPIE, pp. 170–177. DOI: 10.1117/12.627854. URL: https://doi.org/10.1117/12.627854.

Madec, P. -Y. (July 2012). "Overview of deformable mirror technologies for adaptive optics and astronomy". In: *Adaptive Optics Systems III*. Ed. by Brent L. Ellerbroek, Enrico Marchetti, and Jean-Pierre Véran. Vol. 8447. Society of Photo-Optical Instrumentation Engineers (SPIE) Conference Series, 844705, p. 844705. DOI: 10.1117/12.924892.

Madec, P. -Y. et al. (July 2018). "Adaptive Optics Facility: from an amazing present to a brilliant future..." In: *Adaptive Optics Systems VI*. Ed. by Laird

M. Close, Laura Schreiber, and Dirk Schmidt. Vol. 10703. Society of Photo-Optical Instrumentation Engineers (SPIE) Conference Series, p. 1070302. DOI: 10.1117/12.2312428.

Mahajan, Virendra N. (Sept. 1982). "Strehl ratio for primary aberrations: some analytical results for circular and annular pupils". In: *J. Opt. Soc. Am.* 72.9, pp. 1258–1266. DOI: 10.1364/JOSA.72.001258. URL: http://opg.optica.org/abstract.cfm?URI=josa-72-9-1258.

— (Jan. 1983). "Strehl ratio for primary aberrations in terms of their aberration variance". In: *Journal of the Optical Society of America (1917-1983)* 73, p. 860.

Males, J. R. and O. Guyon (Jan. 2018). "Ground-based adaptive optics coronagraphic performance under closed-loop predictive control". In: *Journal of Astronomical Telescopes, Instruments, and Systems* 4.1, p. 019001. DOI: 10.1117/1.JATIS.4.1.019001.

Males, Jared R., Laird M. Close, et al. (July 2018). "MagAO-X: project status and first laboratory results". In: *Adaptive Optics Systems VI*. Ed. by Laird M. Close, Laura Schreiber, and Dirk Schmidt. Vol. 10703. Society of Photo-Optical Instrumentation Engineers (SPIE) Conference Series, p. 1070309. DOI: 10.1117/12.2312992.

Marley, M. S. et al. (Jan. 2007). "On the Luminosity of Young Jupiters". In: *ApJ* 655, pp. 541–549. DOI: 10.1086/509759.

Marois, C. et al. (2003). "Effects of Quasi-Static Aberrations in Faint Companion Searches". In: *EAS Publications Series* 8, pp. 233–243. ISSN: 1633-4760, 1638-1963. DOI: 10.1051/eas:2003067. URL: https://www.eas-journal.org/articles/eas/abs/2003/03/eas0821/eas0821.html (visited on 02/15/2021).

Massioni, P. et al. (2011). "Fast computation of an optimal controller for large-scale adaptive optics". In: 28.11, pp. 2298–2309.

Mawet, Dimitri et al. (Sept. 2012). "Review of small-angle coronagraphic techniques in the wake of ground-based second-generation adaptive optics systems". In: *Space Telescopes and Instrumentation 2012: Optical, Infrared, and Millimeter Wave*. Ed. by Mark C. Clampin et al. Vol. 8442. Society of Photo-Optical Instrumentation Engineers (SPIE) Conference Series, 844204, p. 844204. DOI: 10.1117/12.927245. arXiv: 1207.5481 [astro-ph.IM].

Mayor, M. and D. Queloz (Nov. 1995). "A Jupiter-mass companion to a solar-type star". In: *Nature* 378, pp. 355–359. DOI: 10.1038/378355a0.

Meeker, Seth R. et al. (Dec. 2020). "Design and performance of the PALM-3000 3.5 kHz upgrade". In: *Society of Photo-Optical Instrumentation Engineers (SPIE) Conference Series*. Vol. 11448. Society of Photo-Optical Instrumentation Engineers (SPIE) Conference Series, 114480W, 114480W. DOI: 10.1117/12.2562931. arXiv: 2012.08659 [astro-ph.IM].

Milli, J., T. Banas, et al. (2016). "Speckle lifetime in XAO coronagraphic images: temporal evolution of SPHERE coronagraphic images". In: *Adaptive Optics Systems V*. Ed. by Enrico Marchetti, Laird M. Close, and Jean-Pierre Véran. Vol. 9909. International Society for Optics and Photonics. SPIE, pp. 1455–1472. DOI: 10.1117/12.2231703. URL: https://doi.org/10.1117/12.2231703.

Milli, J., D. Mouillet, et al. (Oct. 2017). "Performance of the extreme-AO instrument VLT/SPHERE and dependence on the atmospheric conditions". In: *arXiv e-prints*, arXiv:1710.05417, arXiv:1710.05417. arXiv: 1710.05417 [astro-ph.IM].

Milli, Julien, Dimitri Mawet, et al. (Jan. 2016a). "Adaptive Optics in High-Contrast Imaging". In: *Astronomy at High Angular Resolution*. Ed. by Henri M. J. Boffin et al. Vol. 439. Astrophysics and Space Science Library, p. 17. DOI: 10.1007/978-3-319-39739-9_2. arXiv: 1701.00836 [astro-ph.IM].

— (2016b). "Adaptive optics in high-contrast imaging". In: *arXiv:1701.00836 [astro-ph]* 439. arXiv: 1701.00836, pp. 17–41. DOI: 10.1007/978-3-319-39739-9_2. URL: http://arxiv.org/abs/1701.00836 (visited on 09/04/2018).

Noll, R. J. (Mar. 1976). "Zernike polynomials and atmospheric turbulence." In: *J. Opt. Soc. Am. A (1917-1983)* 66, pp. 207–211.

Nousiainen, J., C. Rajani, M. Kasper, T. Helin, et al. (May 2022). "Towards on-sky adaptive optics control using reinforcement learning". In: *arXiv e-prints*, arXiv:2205.07554, arXiv:2205.07554. arXiv: 2205.07554 [astro-ph.IM].

Nousiainen, Jalo, Chang Rajani, Markus Kasper, and Tapio Helin (May 2021). "Adaptive optics control using model-based reinforcement learning". In: *Optics Express* 29.10, p. 15327. DOI: 10.1364/OE.420270. arXiv: 2104.13685 [astro-ph.IM].

Oberti, Sylvain et al. (Aug. 2022). "Super-resolution wavefront reconstruction". In: *arXiv e-prints*, arXiv:2208.12052, arXiv:2208.12052. arXiv: 2208.12052 [astro-ph.IM].

Otten, G. P. P. L. et al. (Feb. 2021). "Direct characterization of young giant exoplanets at high spectral resolution by coupling SPHERE and CRIRES+". In: *A&A* 646. _eprint: 2009.01841, A150. DOI: 10.1051/0004-6361/202038517.

Paschall, R.N., M.A. Von Bokern, and B.M. Welsh (1991). "Design of a linear quadratic Gaussian controller for an adaptive optics system". In: *[1991] Proceedings of the 30th IEEE Conference on Decision and Control*, 1761–1769 vol.2. DOI: 10.1109/CDC.1991.261709.

Paschall, Randall N and David J Anderson (1993). "Linear Quadratic Gaussian control of a deformable mirror adaptive optics system with time-delayed measurements". In: *Appl. Opt.* 32.31. Publisher: Optical Society of America, pp. 6347–6358.

Pearson, James E., R. H. Freeman, and Harold C. Reynolds (1979). "CHAPTER 8 - Adaptive Optical Techniques for Wave-Front Correction". In: ed. by Robert R.

Shannon and James C. Wyant. Vol. 7. Applied Optics and Optical Engineering. ISSN: 0197-8535. Elsevier, pp. 245–340. DOI: https://doi.org/10.1016/B978-0-12-408607-4.50015-3. URL: https://www.sciencedirect.com/science/article/pii/B9780124086074500153.

Perrin, Marshall D. et al. (Oct. 2003). "The Structure of High Strehl Ratio Point-Spread Functions". In: *ApJ* 596.1, pp. 702–712. DOI: 10.1086/377689.

Petit, C, J-F Sauvage, et al. (2014). "SPHERE eXtreme AO control scheme: final performance assessment and on sky validation of the first auto-tuned LQG based operational system". In: *Adaptive Optics Systems IV*. Vol. 9148. International Society for Optics and Photonics, 91480O.

Petit, Cyril, Jean-Marc Conan, Caroline Kulcsár, and Henri-François Raynaud (June 2009). "Linear quadratic Gaussian control for adaptive optics and multiconjugate adaptive optics: experimental and numerical analysis". In: *J. Opt. Soc. Am. A* 26.6. Publisher: OSA, pp. 1307–1325. DOI: 10.1364/JOSAA.26.001307. URL: http://josaa.osa.org/abstract.cfm?URI=josaa-26-6-1307.

Petit, Cyril, Jean-Marc Conan, Caroline Kulcsár, Henri-Francois Raynaud, and Thierry Fusco (Jan. 2008). "First laboratory validation of vibration filtering with LQG control law for Adaptive Optics". In: *Optics Express* 16.1, p. 87. DOI: 10.1364/OE.16.000087.

Piatrou, Piotr and Michael C Roggemann (2007a). "Performance study of Kalman filter controller for multiconjugate adaptive optics". In: *Applied optics* 46.9. Publisher: Optical Society of America, pp. 1446–1455.

— (Mar. 2007b). "Performance study of Kalman filter controller for multiconjugate adaptive optics". In: 46.9, pp. 1446–1455.

Pou, B et al. (2022). "Adaptive optics control with multi-agent model-free reinforcement learning". In: *Optics express* 30.2, pp. 2991–3015.

Poyneer, L. A. and B. Macintosh (May 2004). "Spatially filtered wave-front sensor for high-order adaptive optics". In: *Journal of the Optical Society of America A* 21, pp. 810–819. DOI: 10.1364/JOSAA.21.000810.

Poyneer, L. A., B. A. Macintosh, and J.-P. Véran (2007). "Fourier transform wavefront control with adaptive prediction of the atmosphere". In: *Journal of the Optical Society of America A* 24, p. 2645. DOI: 10.1364/JOSAA.24.002645.

Poyneer, Lisa A, David W Palmer, et al. (2016). "Performance of the Gemini Planet Imager's adaptive optics system". In: *Applied Optics* 55.2. Publisher: Optical Society of America, pp. 323–340.

Poyneer, Lisa A. and Jean-Pierre Véran (Nov. 2010). "Kalman filtering to suppress spurious signals in adaptive optics control". In: 27.11, A223–A234.

Prengère, Léonard, Caroline Kulcsár, and Henri-François Raynaud (2020). "Zonal-based high-performance control in adaptive optics systems with application to

astronomy and satellite tracking". In: *JOSA A* 37.7. Publisher: Optical Society of America, pp. 1083–1099.

Ragazzoni, R. and J. Farinato (Oct. 1999). "Sensitivity of a pyramidic Wave Front sensor in closed loop Adaptive Optics". In: *A&A* 350, pp. L23–L26.

Ragazzoni, Roberto (Feb. 1996). "Pupil plane wavefront sensing with an oscillating prism". In: *Journal of Modern Optics* 43.2, pp. 289–293. DOI: 10.1080/09500349608232742.

Raynaud, Henri-François, Caroline Kulcsár, Nelly Cerpa Urra, et al. (July 2022). "Want to improve your cascade 2-stage AO system? Turn it into a high-performance woofer-tweeter system!" In: *Optica Imaging and Applied Optics Congress*. Optica.

Raynaud, Henri-François, Caroline Kulcsár, Rémy Juvénal, et al. (June 2016). "The control switching adapter: a practical way to ensure bumpless switching between controllers while AO loop is engaged". In: *Proc. SPIE Conference on Astronomical Telescopes and Instrumentation*. Edimburgh, U.K.

Ribas, I. et al. (Nov. 2018). "A candidate super-Earth planet orbiting near the snow line of Barnard's star". In: *Nature* 563.7731, pp. 365–368. DOI: 10.1038/s41586-018-0677-y.

Rigaut, Francois et al. (Jan. 1991). "Adaptive optics on a 3.6-m telescope - Results and performance". In: *A&A* 250, pp. 280–290.

Roddier, F. (Jan. 1981). "The effects of atmospheric turbulence in optical astronomy". In: *Progess in Optics* 19, pp. 281–376. DOI: 10.1016/S0079-6638(08)70204-X.

— ed. (1999). *Adaptive optics in astronomy*. Cambridge, U.K. ; New York: Cambridge University Press. ISBN: 978-0-521-55375-9.

Rousset, G. et al. (Apr. 1990). "First diffraction-limited astronomical images with adaptive optics". In: *aap* 230.2, pp. L29–L32.

Rousset, Gérard (1999). "Wave-front sensors". In: *Adaptive Optics in Astronomy*. Ed. by FrançoisEditor Roddier. Cambridge University Press, pp. 91–130. DOI: 10.1017/CBO9780511525179.005.

Sauvage, Jean-Francois et al. (May 2016). "SAXO: The extreme adaptive optics system of SPHERE (I) system overview and global laboratory performance". In: *Journal of Astronomical Telescopes, Instruments, and Systems* 2, p. 025003. DOI: 10.1117/1.JATIS.2.2.025003.

Singh, Garima et al. (Sept. 2017). "A Demonstration of a Versatile Low-order Wavefront Sensor Tested on Multiple Coronographs". In: *pasp* 129.979, p. 095002. DOI: 10.1088/1538-3873/aa76c1.

Sinquin, Baptiste et al. (2020). "On-sky results for adaptive optics control with data-driven models on low-order modes". In: *MNRAS* 498.3. Publisher: Oxford University Press, pp. 3228–3240.

Sivo, G., C. Kulcsár, J.-M. Conan, H.-F. Raynaud, Gendron. É., et al. (Sept. 2011). "MOAO real-time LQG implementation on CANARY". In: *Second International Conference on Adaptive Optics for Extremely Large Telescopes*.

Sivo, Gaetano, Caroline Kulcsár, Jean-Marc Conan, Henri-François Raynaud, Éric Gendron, et al. (2014). "First on-sky SCAO validation of full LQG control with vibration mitigation on the CANARY pathfinder". In: *Optics express* 22.19. Publisher: Optical Society of America, pp. 23565–23591.

Snellen, I. et al. (Apr. 2015). "Combining high-dispersion spectroscopy with high contrast imaging: Probing rocky planets around our nearest neighbors". In: *aap* 576, A59, A59. DOI: 10.1051/0004-6361/201425018. arXiv: 1503.01136 [astro-ph.EP].

Snik, Frans et al. (Sept. 2012). "The vector-APP: a broadband apodizing phase plate that yields complementary PSFs". In: *Modern Technologies in Space- and Ground-based Telescopes and Instrumentation II*. Ed. by Ramón Navarro, Colin R. Cunningham, and Eric Prieto. Vol. 8450. Society of Photo-Optical Instrumentation Engineers (SPIE) Conference Series, 84500M, p. 84500M. DOI: 10.1117/12.926222. arXiv: 1207.2970 [astro-ph.IM].

Soummer, R., C. Aime, and P. E. Falloon (Jan. 2003). "Stellar coronagraphy with prolate apodized circular apertures". In: *aap* 397, pp. 1161–1172. DOI: 10.1051/0004-6361:20021573.

Soummer, Rémi, André Ferrari, et al. (Nov. 2007). "Speckle Noise and Dynamic Range in Coronagraphic Images". In: *apj* 669.1, pp. 642–656. DOI: 10.1086/520913. arXiv: 0706.1739 [astro-ph].

Spake, J. et al. (May 2018). "Helium in the eroding atmosphere of an exoplanet". In: *Nature* 557. DOI: 10.1038/s41586-018-0067-5.

Tesch, Jonathan et al. (Apr. 2015). "On-sky demonstration of optimal control for adaptive optics at Palomar Observatory". In: *Opt. Lett.* 40.7, pp. 1575–1578.

Thalmann, Christian et al. (July 2008). "SPHERE ZIMPOL: overview and performance simulation". In: *Ground-based and Airborne Instrumentation for Astronomy II*. Ed. by Ian S. McLean and Mark M. Casali. Vol. 7014. Society of Photo-Optical Instrumentation Engineers (SPIE) Conference Series, 70143F, 70143F. DOI: 10.1117/12.789158.

Thomas, S., T. Fusco, et al. (Sept. 2006). "Comparison of centroid computation algorithms in a Shack-Hartmann sensor". In: *mnras* 371.1, pp. 323–336. DOI: 10.1111/j.1365-2966.2006.10661.x.

Thomas, S. J., S. Adkins, et al. (June 2008). "Study of optimal wavefront sensing with elongated laser guide stars". In: *mnras* 387.1, pp. 173–187. DOI: 10.1111/j.1365-2966.2008.13110.x.

Van Overschee, Peter and Bart De Moor (Jan. 1996). "Subspace identification for linear systems. Theory, implementation, applications. Incl. 1 disk". In: vol. xiv, pp. xiv + 254. ISBN: 0-7923-9717-7. DOI: 10.1007/978-1-4613-0465-4.

Verhaegen, Michel and Vincent Verdult (2007). *Filtering and System Identification: A Least Squares Approach*. Cambridge University Press. DOI: 10.1017/CBO9780511618888.

Vérinaud, C. et al. (Feb. 2005). "Adaptive optics for high-contrast imaging: pyramid sensor versus spatially filtered Shack-Hartmann sensor". In: *mnras* 357.1, pp. L26–L30. DOI: 10.1111/j.1745-3933.2005.08638.x.

Vérinaud, Christophe (Mar. 2004). "On the nature of the measurements provided by a pyramid wave-front sensor". In: *Optics Communications* 233.1, pp. 27–38. ISSN: 0030-4018. DOI: 10.1016/j.optcom.2004.01.038. URL: https://www.sciencedirect.com/science/article/pii/S0030401804000628 (visited on 02/13/2021).

Vidal, Fabrice et al. (2022). "SAXO+ upgrade: system choices and numerical simulations". In: *Adaptive Optics Systems VIII*. Ed. by Laura Schreiber, Dirk Schmidt, and Elise Vernet. Vol. 12185. International Society for Optics and Photonics. SPIE, p. 121854D. DOI: 10.1117/12.2629325. URL: https://doi.org/10.1117/12.2629325.

von Kármán, Theodore (Nov. 1948). "Progress in the Statistical Theory of Turbulence". In: *Proceedings of the National Academy of Science* 34.11, pp. 530–539. DOI: 10.1073/pnas.34.11.530.

Wagner, K. et al. (Feb. 2021). "Imaging low-mass planets within the habitable zone of Alpha Centauri". In: *Nature Communications* 12.1, p. 922. ISSN: 2041-1723. DOI: 10.1038/s41467-021-21176-6. URL: https://doi.org/10.1038/s41467-021-21176-6.

Zechmeister, M. et al. (July 2019). "The CARMENES search for exoplanets around M dwarfs. Two temperate Earth-mass planet candidates around Teegarden's Star". In: *A&A* 627, A49. DOI: 10.1051/0004-6361/201935460.

Zidi, Amal et al. (2022a). "The MICADO first light imager for the ELT: SCAO LQG control performance with windshake, vibrations and mirror dynamics". In: *Adaptive Optics Systems VIII*. Vol. 12185. SPIE, pp. 892–897.

— (2022b). "The MICADO first light imager for the ELT: SCAO LQG control performance with windshake, vibrations, and mirror dynamics". In: *Adaptive Optics Systems VIII*. Ed. by Laura Schreiber, Dirk Schmidt, and Elise Vernet. Vol. 12185. International Society for Optics and Photonics. SPIE, 121852P. DOI: 10.1117/12.2629863. URL: https://doi.org/10.1117/12.2629863.